Systematic study of neutron density distributions of Sn isotopes by proton elastic scattering

Satoru Terashima

Doctoral Dissertation

Department of Physics

Kyoto University

April, 2008

Abstract

Cross sections and analyzing powers for proton elastic scattering from ^{116,118,120,122,124}Sn at 295 MeV have been measured for a momentum transfer up to about 3.5 fm^{-1} to deduce systematic changes of the neutron density distribution at Research Center for Nuclear Physics, Osaka University.

We have analyzed the experimental data based on the relativistic impulse approximation using the relativistic Love-Franey effective interaction. The interaction is tuned to explain the proton elastic scattering of a nucleus ^{58}Ni whose density distribution is well known by changing the coupling constants and masses of exchanged mesons. This interaction is applied for the proton elastic scattering of tin isotopes to deduce these neutron density distributions using the model-independent form densities. We have especially considered how the model uncertainty affect the neutron density distribution.

The neutron skin thickness is deduced by substituting the well known root mean square radius of proton density distribution from that of of neutron. The result of our analysis shows the clear systematic behavior of the gradual increase in the neutron skin thicknesses of tin isotopes with mass number, and these values are in good agreement with the mean field calculation using SkM* parameterization. We have attempted to deduce the symmetry energy coefficient $a_{\rm sym}$ and its density dependent coefficient L which are important components of the equation of state. These symmetry coefficients theoretically have the linear relation against the neutron skin thickness. The average values of the $a_{\rm sym}$ and the L are 30.0 $^{+0.5}_{-0.4}$ $\pm 2.0_{\rm sys}$ MeV and 47.9 $^{+7.2}_{-7.9}$ $\pm 15.0_{\rm sys}$MeV, respectively.

Contents

Chapter 1

Introduction

1.1 Study of nuclear charge distributions

Since the earliest days of nuclear physics, distributions of nuclear charge and density have received considerable interests. Information on charge distributions in nuclei is obtained from experiments with electron scattering. In 1950s, Hofstader *et al.* had performed 'High-Energy' electron scattering experiments at Stanford [1], and the study for charge distributions had started. At the beginning, experimental data were analyzed using the densities of simple function such as Fermi type or modified Gaussian type [2, 3]. By the end of 1970s, the measurement extended to the value of 0.1 pb/sr at momentum transfer of 3.5 fm^{-1} using high-intensity electron beam ($\sim$100 μA), and so-called model-independent method had appeared to analyze the high momentum-transfer data [4, 5]. These methods have been improved in many respects and applied extensively to extract nuclear charge distributions as shown in Fig. 1.1 [6]. Following numerous efforts to obtain accurate experimental data which includes measurements of absolute cross section data, the application of the methods and procedures has resulted in a rather clear details of ground-state charge distributions of stable nuclei. The elastic scattering is often combined with muonic-atom X-ray measurements which lead to precise information of nuclear mean radius [7].

1.2 Extraction of point proton density distributions

Point proton density distribution has been obtained from these 'precise' charge distribution of nucleus by unfolding charge distributions of proton and neutron themselves. The proton and the neutron are not point-like but finite-size particles, and these charge distributions can be described by form factors same as in the case of nuclei. For nucleons, two form factors; electric G_E and magnetic G_M form factors; both of which depend on momentum transfer Q^2 are necessary to characterise both the electric and magnetic distributions.

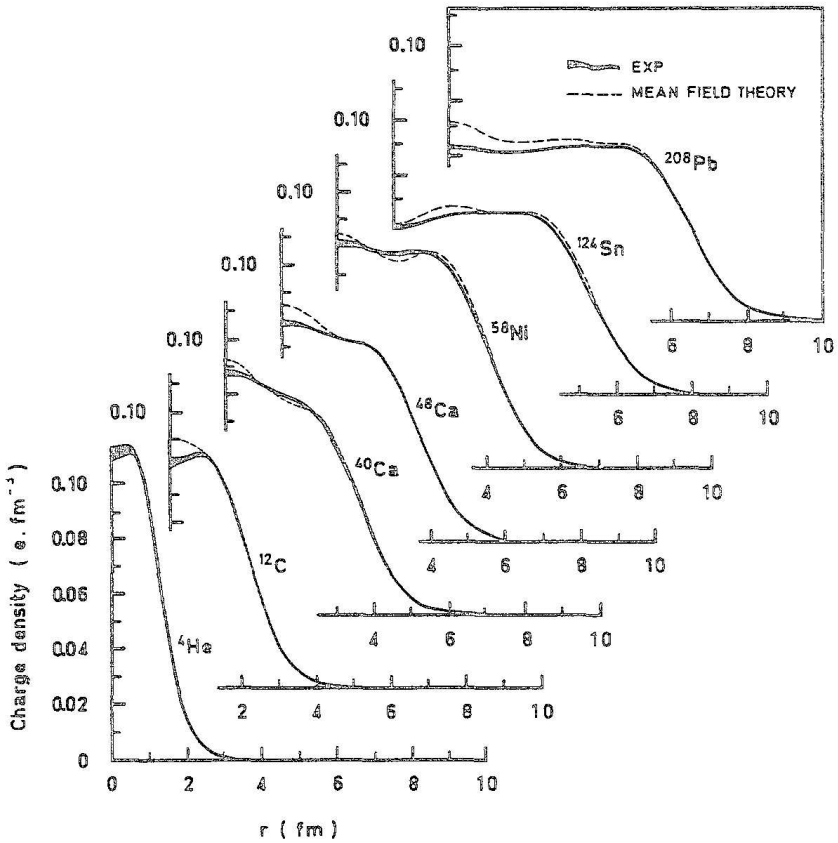

Figure 1.1: Nuclear ground state charge distributions, and comparison between the experimental charge distributions of magic nuclei and mean field predictions. The experiment have been performed at Amsterdam, Darmstadt, Mainz, NBS, Stanford, and Scalay over a period of 30 years [6].

The proton electric G_E^p and magnetic G_M^p form factors can be separately determined by performing cross-section measurements using the Rosenbluth separation technique [8]. The proton electric form factor and the magnetic form factors of both the proton and the neutron fall off similarly with Q^2, and their form factors can be described to a good approximation by a so-called dipole form factor [9]. The observed dipole form factor corresponds to a charge distribution which falls off exponentially. Recently, the advance of a technology for polarization has provided more precise proton electromagnetic form factors [10]. At present, we know precise proton electromagnetic form factors in a wide momentum transfer-range up to 5.6 GeV^2 [11, 12]. On the neutron side, the neutron electric G_E^n and the magnetic G_M^n form factors had been measured by quasi-elastic scattering off ^{2}H or ^{3}He. Due to the smallness of G_E^n, the measurement was very difficult [13]. However, an alternative elegant approach has been developed to determine the charge radius of the free neutron. The mean squared charge

radius of the neutron was obtained by measuring the transmission of low-energy neutrons through liquid ^{208}Pb and ^{209}Bi [14]. These results provided information concerning the neutron charge density. And then, the recent technology for polarization provides more precise neutron electromagnetic form factors. A series of double polarization measurements of neutron knockout from a polarized ^{2}H or ^{3}He target have provided accurate data on G_E^n in the past decade [15]. The neutron appears from the outsides to be electrically neutral and it therefore has a small electric form factor.

In recent years, highly accurate data have established the nucleon electric and magnetic form factors. Therefore, a large amount of nucleon electric form factor data up to 5.6 (GeV/c)^2 for proton [16] and 1.6 (GeV/c)^2 for neutron [17] makes it possible to obtain a precise charge distribution of both proton and neutron.

1.3 Investigation of the neutron density distribution

Charge distributions in the stable nuclei have been reliably measured by electron elastic scattering and muonic X-ray data [7]. These charge sensitive experiments provided precise information on charge distributions. On the other hand, neutron density distributions are much more difficult to observe, since the electromagnetic interaction provides little information about neutron density distributions.

Many experiments have been attempted to extract neutron and matter density distributions. X-ray measurements from exotic atoms, such as pionic, kaonic, and antiprotonic atom provide information on nuclear periphery. Recently the systematic study using X-ray measurements from antiprotonic atoms was performed at the Low Energy Antiprotonic Ring (LEAR) of CERN [18]. Trzcinska *et al.* measured the widths and shifts of X-ray transitions in twenty-six antiprotonic atoms, and they deduced a ratio of the annihilation probability on a proton to that on a neutron at the peripheral region. The ratio is related to an integrated ratio of neutron to proton density over the peripheral region using the antiproton effective scattering length [19]. However the measurements do not provide information about the precise shape of nuclear density due to a little information on the nuclear structure.

Hadronic probes such as pion, kaon, and alpha elastic scattering were also used to deduce a neutron or matter density distribution [20, 21, 22]. The pion-nucleon interaction is very strong in the Δ-resonance region. The existence of Δ-resonance easily masks information on the nuclear interior. In order to avoid the region, lower energy pion ($<$ 80 MeV) elastic scattering was attempted to apply for studying differences between neighboring nuclei under the limited degree of freedom using the phenomenological Kisslinger potential [20, 21]. The relation between the phenomenological potential and nucleon density distributions at low energy is less clear. It is difficult to study density distributions using the phenomenological potential. Latter, higher energy pion ($\sim$1 GeV/c) elastic scattering experiment had been performed at KEK above the

Δ-resonance region [23, 24]. Takahashi *et al.* analyzed the data using the first-order optical potential model factorized. They showed the necessity of the modification for the elementary amplitude to explain the experimental angular distributions and of the Fermi motion correction to explain total cross section [23]. Thus, the pion-nuclei scattering is microscopically not so understood as to study interior density. The kaon-nuclei elastic scattering have also received considerable attention as capable probe for the interior nuclei [25]. However the experimental difficulties of its short lifetime, or an impurity of kaon beam limit the high-quality experimental data and knowledge of the kaon-nucleon scattering amplitude. Rather poor of understanding of pion-, kaon-, or alpha-nucleus interaction limits their sensitivities for studying nuclear densities. Compared with the above mentioned hadronic probes, proton elastic scattering at intermediate energies is suitable for extracting information on nuclear surface and interior, because protons have a large mean free path in nuclear medium and therefore its reaction mechanism is simple.

In 1970s, pioneering experiments were performed to study nuclear densities by protons of intermediate energy at Brookhaven [26]. Experiments using around 1 GeV proton beam was performed at Gatchina and Saclay [27, 28]. Alkhaznov *et al.* analyzed the data using the Glauber model neglecting the spin-orbit effect which plays an important role in a large momentum transfer region [27]. In their analysis, the experimental data at larger scattering angles were not included in the fit, since the Glauber model is limited to low momentum transfer. Brussaud and Brussel attempted to study neutron density distributions using the same data, the Glauber model, and a "model-independent" prescription for the nuclear density [29]. They found that the limitations are not really due to intermediate energy protons as an experimental tool but mainly arisen from the Glauber diffraction approximation to small momentum transfer. The restrictions of the Glauber diffraction approach to a low momentum transfer and the neglect of spin-orbit effects triggered a series of analyses using the multiple scattering theory of optical model potential by Kerman, McManus and Thaler (KMT) [30]. A large amount of new precise data by 800 MeV polarized protons became available at LAMPF. The dashed lines in Fig. 1.2 are the first-order KMT optical potential calculation by Ray *et al.* using point proton and neutron densities predicted by the density matrix expansion (DME) Hartree Fock [31]. Two-nucleon scattering amplitudes were determined from nucleon-nucleon total cross section and polarization data [31, 32]. They partially adopted "model-independent" functional form for the neutron density distribution to reduce the constrain from model-dependent functional form such as simple Fermi function. However, the prediction using the scattering amplitude from nucleon-nucleon data could not explain analyzing powers for a proton-nucleus scattering. Therefore in their analyses two parameters among twelve were phenomenologically adjusted to explain the scattering for each nucleus as free parameters. The uncertainty for the spin-orbit term still remains.

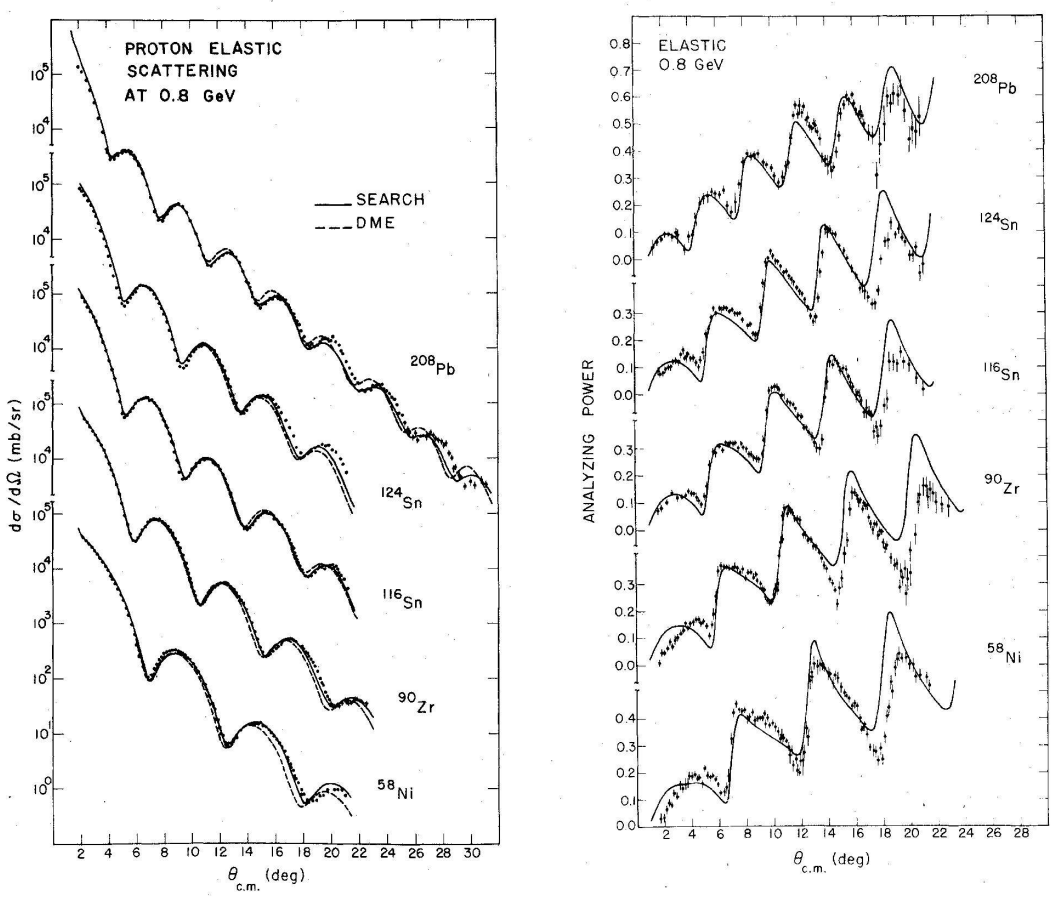

Figure 1.2: Proton elastic scattering at 0.8 GeV on targets ^{58}Ni, ^{90}Zr, ^{116,124}Sn, and ^{208}Pb. The solid lines are results with use of the KMT optical potential, freely searched neutron densities and spin-dependent parameters [30].

300 MeV proton was adopted as a probe to obtain information of nuclear interior considering the following reasons. To deduce nuclear densities using protons, the incident energy has to be sufficiently high to describe the scattering by a simple reaction mechanism. At energies above 100 MeV, we can describe proton elastic scattering based on the nucleon-nucleon interaction, because the imaginary part of the optical potential is mainly explained by a quasi-free process without the need for a renormalization factor. Until recently, energies above 500 MeV have been applied for proton elastic scattering to study neutron density distributions [31, 32, 33]. However, this energy is sufficiently high to produce mesons, and information on the nuclear interior is easily masked by the imaginary potential due to the meson-productions. Furthermore, the total cross section of nucleon-nucleon scattering shows a minimum at the incident energy of 300 MeV [**?**]. We thus adopt 300 MeV protons in this work as probes for information on the nuclear interior. A mean free path of 300 MeV proton is about 3 fm in a normal density ρ=$\sim$0.2(fm^{-3}).

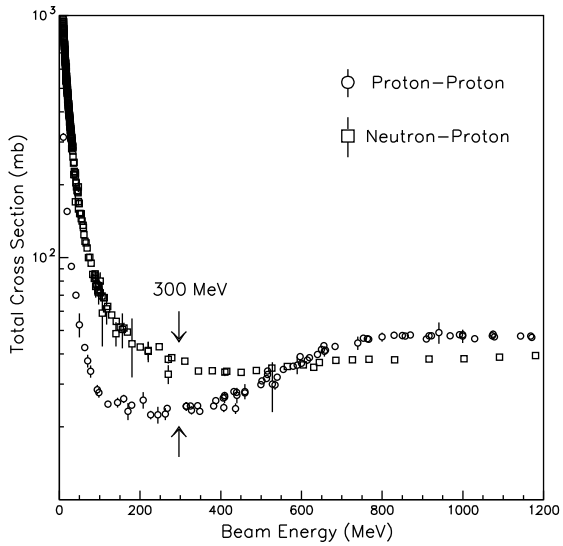

Figure 1.3: The experimental data of nucleon-nucleon total cross section from Ref. [34]. Open circles show the proton-proton total cross section, and open squares show neutron-proton total cross section. The adopted energy 300 MeV is indicated by arrows.

In 1980s, relativistic approaches based on Dirac equations applied to the elastic scattering of intermediate energy protons. Murdock and Horowitz calculated the elastic scattering at the several hundred MeV using the relativistic Love-Franey effective interaction based on relativistic impulse approximation [35]. They well explained experimental data especially polarization observables for ^{16}O, ^{40,48}Ca, ^{90}Zr, and, ^{208}Pb by treating the exchange term. Sakaguchi *et al.* calibrated the effective interaction including medium effects for the scattering from a nucleus ^{58}Ni, whose density distribution is well known [36, 37]. The elastic scattering from ^{58}Ni was used to tune the interaction, since ^{58}Ni is the heaviest stable nucleus with N $\approx$ Z and the density distribution of neutrons in ^{58}Ni is well assumed to be the same as the that for proton. In order to explain the experimental data they have found that they have to modify the scattering amplitudes of nucleon-nucleon interaction inside the nucleus. For our first systematic search for neutron density distributions, five tin isotopes ^{116,118,120,122,124}Sn are selected. Tin has many stable isotopes (^{112}Sn-^{124}Sn). Also, unstable tin isotopes have a long isotopic chain including two double-magic nuclei (^{100}Sn [N=50], ^{132}Sn [N=82]). Moreover, its proton number is a magic number (Z=50). Thus, tin isotopes are suitable for the study of systematic changes in neutron density distributions. The main purposes of this work are to attempt to deduce information on neutron density distributions, and to systematically study the neutron skin thickness of tin isotopes.

1.4 Symmetry energy and neutron skin thickness

The nuclear equation of state (EOS) is characterized by the following values, a binding energy per nucleon E/A, a normal saturation density ρ_∞, an incompressibility of nuclear matter K_∞, an effective nucleon mass m^*_∞, and a symmetry energy a_{sym}. Recently, K_∞ is experimentally determined by measuring two giant resonances of compressional modes; the isoscalar giant monopole resonance (ISGMR), the isoscalar giant dipole resonance (ISGDR). Its value of ^{208}Pb is K_∞=215±6 MeV [38]. Several components of the EOS, E/A∼ -16 MeV, ρ_∞ ∼0.16 fm^{-3}, and m^*_∞/m∼0.8, are well known as empirical saturation properties of symmetric nuclear matter. Thus, only the symmetry energy a_{sym} remains to be solved as an unknown parameter of EOS.

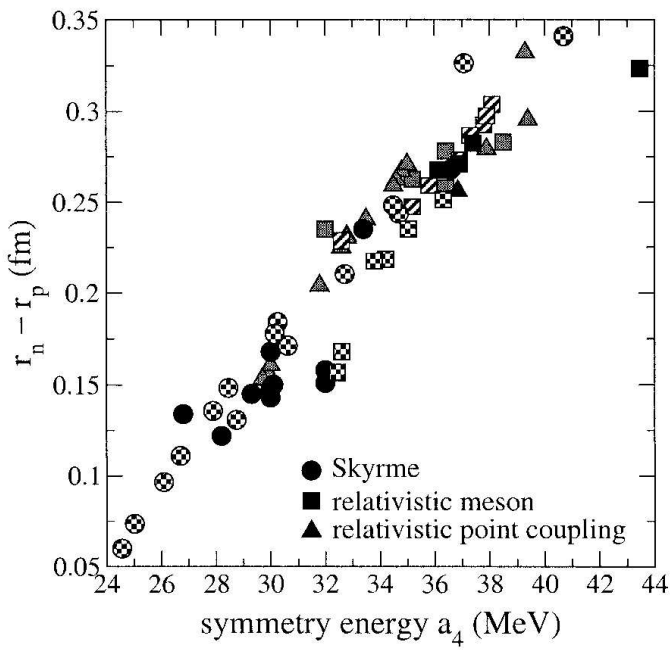

Figure 1.4: The neutron skin thickness of ^{208}Pb versus the symmetry energy obtained with several nonrelativistic and relativistic mean field parameter sets [43].

Recent studies in some unstable nuclei show that differences between proton and neutron shapes are larger than stable nuclei. Besides, it was indicated that the difference of between neutron radius and proton one, which is called neutron skin thickness related to the symmetry energy of the EOS [39, 40, 41, 42, 43]. Brown [39] showed that the unique correlation between neutron skin Thus we can study the EOS of the neutron matter from the analysis of neutron skins using this correlation. The neutron skin thicknesses are calculated using effective interactions. Furnstahl [43] showed a direct connection between the neutron skin in the spherical

nucleus ^{208}Pb and the symmetry term of the EOS in Fig. 1.4. Reinhard *et al.* also pointed out that there is a unique relation between the symmetry energy and the neutron skin thickness of tin isotopes, and the relation is almost independent on shell structure [44]. He showed the trends of neutron radii along the tin isotopic chain. A study of the neutron skin thickness of such stable tin isotopes should give understanding of the symmetry energy of the EOS.

In Chapter 2, the experimental setup is presented. The detail of the data reduction is described in Chapter 3, and the theoretical analysis for the scattering observables is shown in Chapter 4. The discussion on the result of the deduced densities and the relation to the EOS properties are shown in Chapter 5. Finally the conclusion is given in Chapter 6.

Chapter 2

Experiment

2.1 Beam line

The measurements have been performed at Research Center for Nuclear Physics (RCNP), Osaka University. Polarized protons from a high intensity polarized ion source [45] were injected into AVF cyclotron (K=120), transported to six sector ring cyclotron (K=400) and accelerated up to 295 MeV. The polarization axis was in the vertical direction. Spin direction and magnitude of the beam polarization were measured continuously by two sets of sampling-type beam line polarimeters (BLPs) [46] placed between the ring cyclotron and a scattering chamber. The beam was then transported to a target center in the scattering chamber. The typical beam spot size on the target during measurements was 1 mm in diameter. Finally, the beam was stopped by an internal Faraday cup inside the scattering chamber (ScFC) in the case of forward-angle measurements. In the measurements at backward scattering angles, the beam was transported to another Faraday cup located inside the shielding wall of the experimental room about 25 m downstream of the scattering chamber (WallFC). The integrated beam current was monitored using a current digitizer (Model 1000C) made by BIC (Brookhaven Instruments Corporation). Additionally, the beam current was monitored independently using p-p cross sections at the BLPs during the backward-angle measurements.

2.2 Beam line polarimeter

Figure 2.2 shows the setup of the BLPs. BLPs are consist of eight plastic scintillator counters. Four counters are placed on a horizontal plane of beam, the other counters are placed on a vertical plane. In this experiment, the first BLP (BLP1) placed just after the entrance to the west experimental room was used to measure the beam polarization with four counters on the horizontal plane. And the second BLP (BLP2) placed in the middle between BLP1 and target was used to monitor the beam intensity during this experiments with four counters on the vertical plane. The both BLPs are synchronized controlled and typical sampling ratio is 10% of

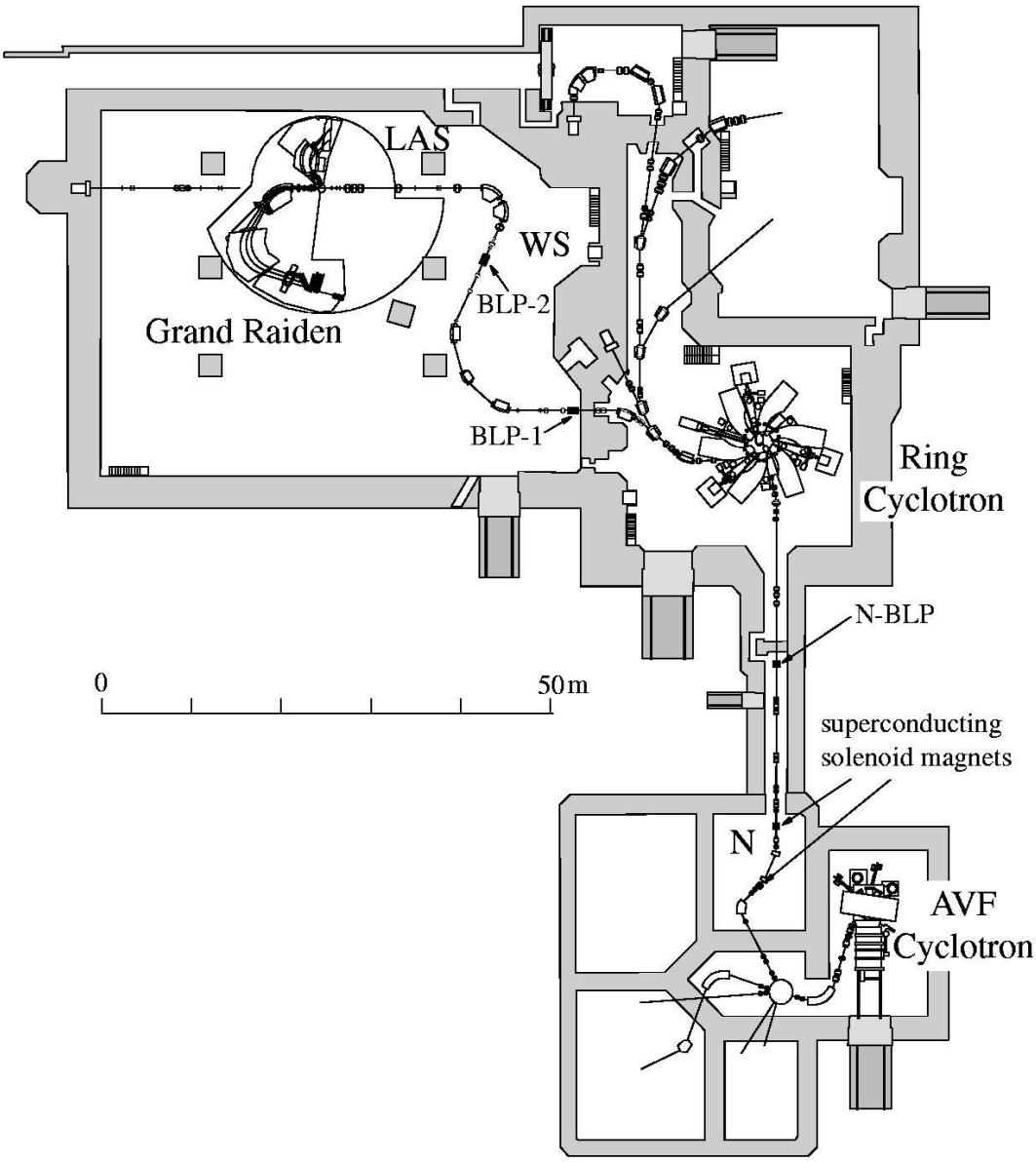

Figure 2.1: Overview of the RCNP facility.

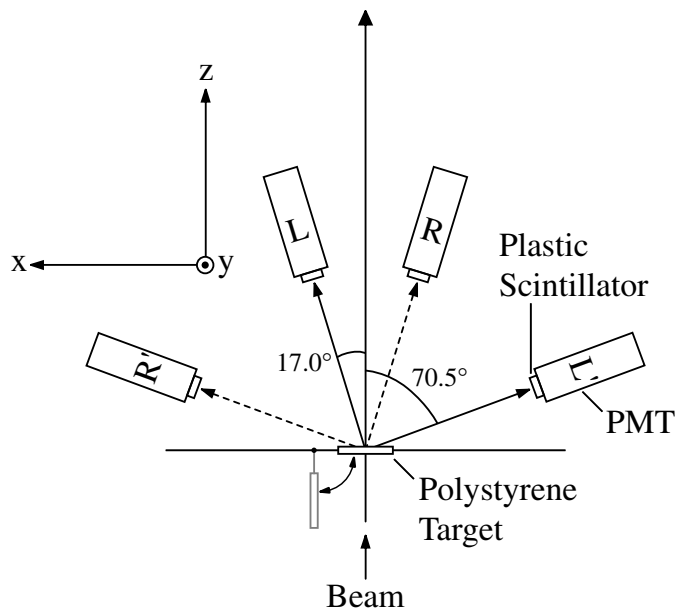

Figure 2.2: Setup of BLPs in the horizontal plane

total DAQ time. BLP1 utilized only left-right asymmetries in p-H scattering from $(CH_2)_n$ foil to determine the y-axis transverse components p_y of the beam polarization. A pair of protons scattered to the opposite direction in the center of mass system are detected in coincidence by a pair of the scintillation detectors. The scattering angle for the forward counters was set to 17.0° where p-p scattering has the maximum analyzing power A_y= 0.40. The angle of the backward counters was 70.5° which was determined by the p-p kinematics. Delayed coincidence events between different beam bunches were also measured to estimate the numbers of accidental coincidence protons. During the measurement, the analyzing target was periodically inserted on the beam position for polarization measurement. A typical beam polarization was 65%.

2.3 Targets

Five tin isotope targets (^{116,118,120,122,124}Sn) in the form of self-supporting metal foils were used for this experiment. Two different thicknesses were used for each target. Thin targets were used for the forward-angle measurements to reduce the dead time of the data acquisition system, and thick targets were for the backward-angle measurements to increase the yields. The enrichment and thicknesses of each target are shown in Table 2.1. The main contaminants of the targets originated from other tin isotopes. The present energy resolution could not separate the elastic scattering of other tin isotopes. Thus, the targets including the contamination were analyzed from other isotopes at all momentum transfer regions. The error of this analysis is estimated less than 1% for all cross sections and analyzing powers. An automatic target changer system

Table 2.1: The target enrichment and thicknesses of tin isotopes.

Nuclei	Enrichment	Thin	Thick
^{116}Sn	95.5%	10.0mg/cm^2	100.mg/cm^2
^{118}Sn	95.8%	10.0mg/cm^2	100.mg/cm^2
^{120}Sn	98.4%	5.12mg/cm^2	39.9mg/cm^2
^{122}Sn	93.6%	10.5mg/cm^2	85.4mg/cm^{2}5A
^{124}Sn	95.5%	5.00mg/cm^2	62.7mg/cm^2

was used in this experiment to reduce the systematic errors of relative cross sections between isotopes. A schematic view of the target changing system is shown in Fig. 2.3. The vertical position of the target was changed by using a pulse stepping motor, which was controlled remotely using CAMAC system. A Linux PC was used for this purpose independently from the main data acquisition (DAQ) system. A schematic view of the control system for this experiment is shown in Fig. 2.4. A stack of three targets is used in a single measurement, which was moved vertically every 2 min to avoid errors due to the drift of the beam direction and that of its position on the targets. In a normal experiment using polarized beam, a stand-alone VME module controlled the direction of beam spin with a time sequence summarized in Fig. 2.5. The target control was synchronized with the signal for spin-control from the VME module as shown in Fig. 2.4. The position information on targets was added to the event header in event-by-event, and the integrated beam current was measured for each target separately. The position of the target are always monitored by reading register attached to the moving system. The time necessary to change target were typically 0.5 sec, and the precision of the target position reproducibility is better than 0.1mm. The beam was stopped by sending a signal to the ion-source during the moving period of the target.

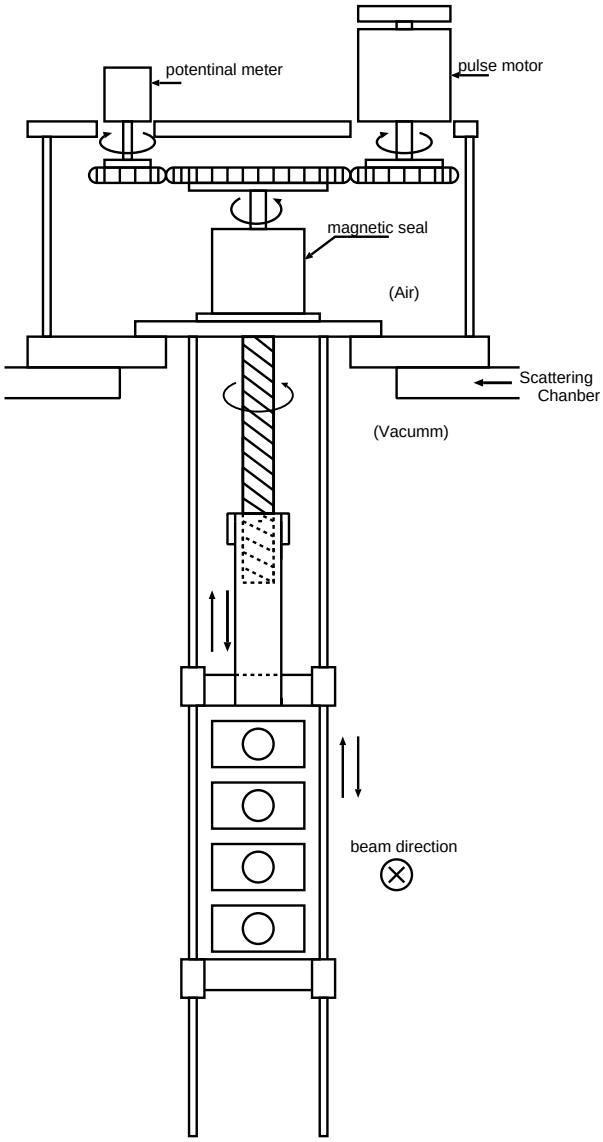

Figure 2.3: Schematic view of the target changer system installed on top of the scattering chamber.

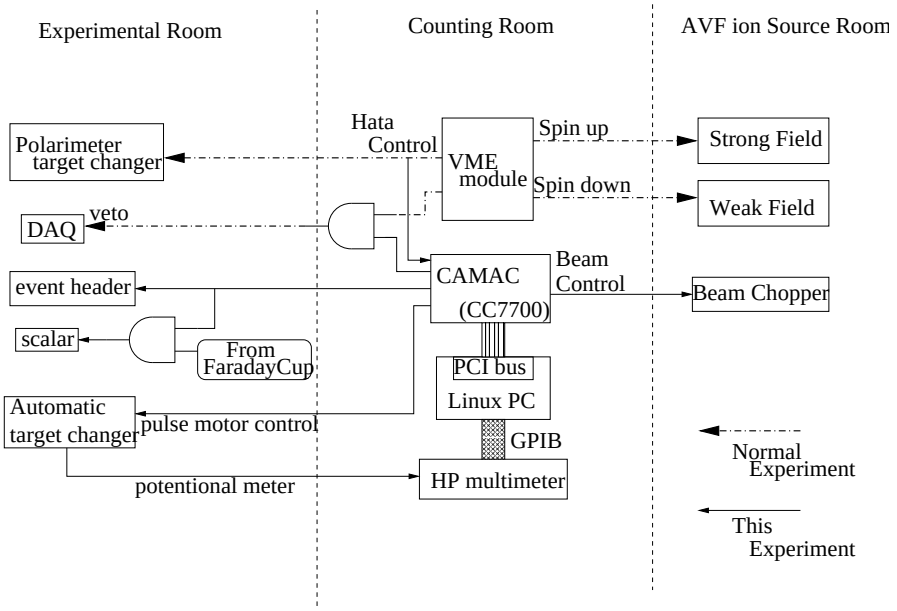

Figure 2.4: Schematic view of the control system for the target changer system. Solid arrow show the additional parts for this experiment.

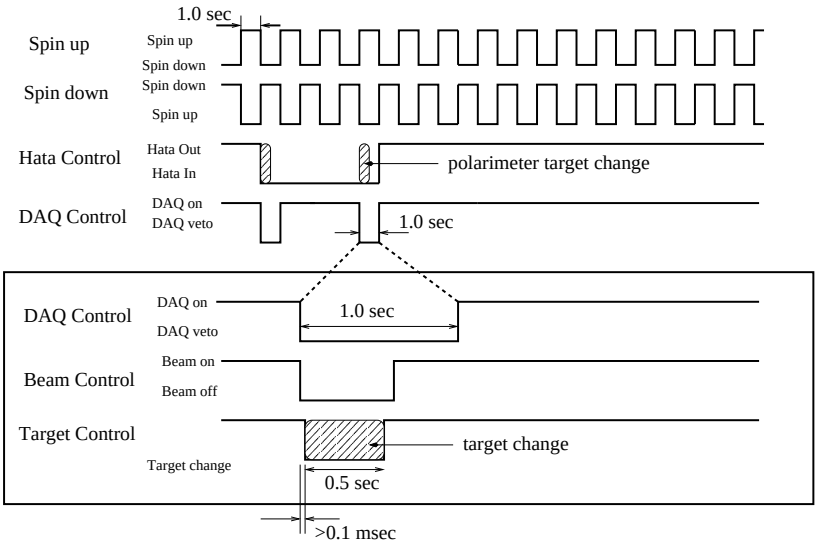

Figure 2.5: Timing chart between normal polarization measurement and the target changing system. Upper four (Spin up, Spin down, BLP Control which was called Hata Control, and DAQ Control) show the standard line for control polarimeter target.

2.4 Grand Raiden Spectrometer

Figure 2.6 shows a high resolution($p/\Delta p \sim 37{,}000$) magnetic spectrometer 'Grand Raiden' (GR). The GR consists of three dipole (D1,D2, and DSR) magnets, two quadrapole (Q1 and Q2) magnets, a sextupole (SX) magnet, and a multipole (MP) magnet. In Table 2.2, the designed values of specifications and ion-optical properties of the GR are summarized [47]. MP magnet is designed for the reduction of higher order aberrations, DSR magnet is designed for the measurement of the in-plane polarization transfer. These two magnets were not used in this experiment.

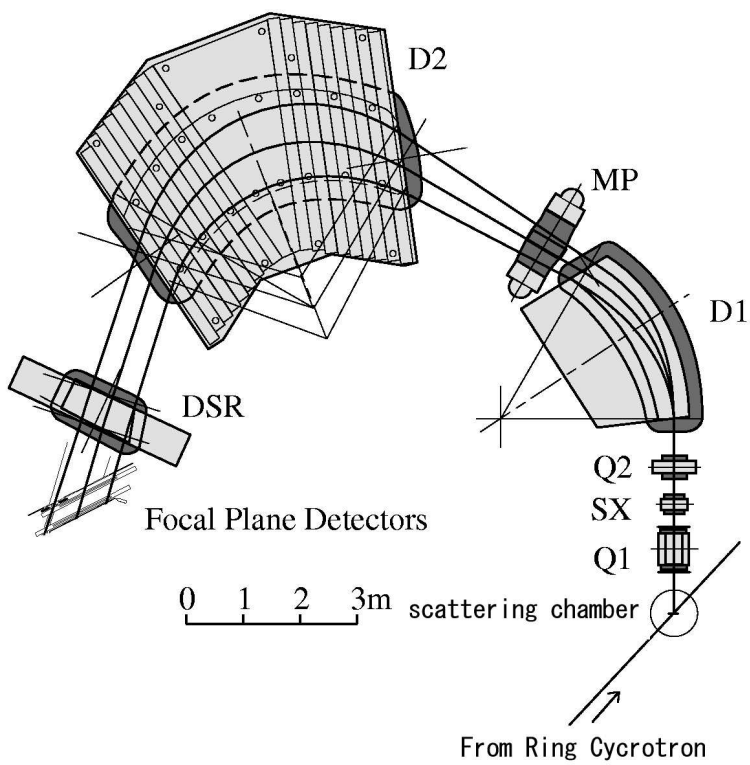

Figure 2.6: Layout of the 'Grand Raiden' spectrometer and the focal plane.

Table 2.2: Grand Raiden specifications

Configuration	QSQD(M)D(D)
Mean orbit radius	3 m
Total deflection angle	162°
Focal plane length	120 cm
Focal plane tilting angle	45.0°
Maximum particle rigidity	5.4 Tm
Momentum resolving power $p/\Delta p$	37,000
Momentum broadness	5 %
Acceptance angle-vertical	±70 mrad
Acceptance angle-horizontal	±20 mrad
Horizontal magnification $(x\|x)$	-0.417
Vertical magnification $(y\|y)$	5.98
Momentum dispersion $(x\|\delta)$	15451 mm

2.5 Angular distribution measurements

There are three different settings commonly used for the GR system depending upon experimental conditions, namely 'GR mode', 'p2p mode', and 'LAS mode'. Two modes among these settings were used in this experiment. A use of a high current beam is needed for low cross section measurement at a high momentum transfer region. For a high current beam more than 15 nA, we must use the WallFC due to a regulation of a radiation control. The 'p2p mode' is a setting for the use of both of two spectrometers; the Grand Raiden spectrometer (GR) and a Large Acceptance Spectrometer (LAS). Only in this mode an additional beam duct transporting beams from the scattering chamber to the WallFC can be attached as shown in Fig. 2.7. The 'GR mode' is a setting enable to perform the forward angle measurements including the 0° scattering. Hence we used the 'GR mode' for the forward angle measurement ($< 28°$) and the 'p2p mode' for the backward angle measurement ($> 25°$).

The GR was rotated for the angular distribution measurement. In the case of the experiment using high intensity beam like this experiment, the radiation level in the experimental room is ordinarily high, this situation makes it more difficult to enter the experimental room, when we rotate the GR. Thus the measurements of the angular distributions for cross sections and analyzing powers were performed to avoid any remnant radiation dosages to the experimentalist in the experimentally room.

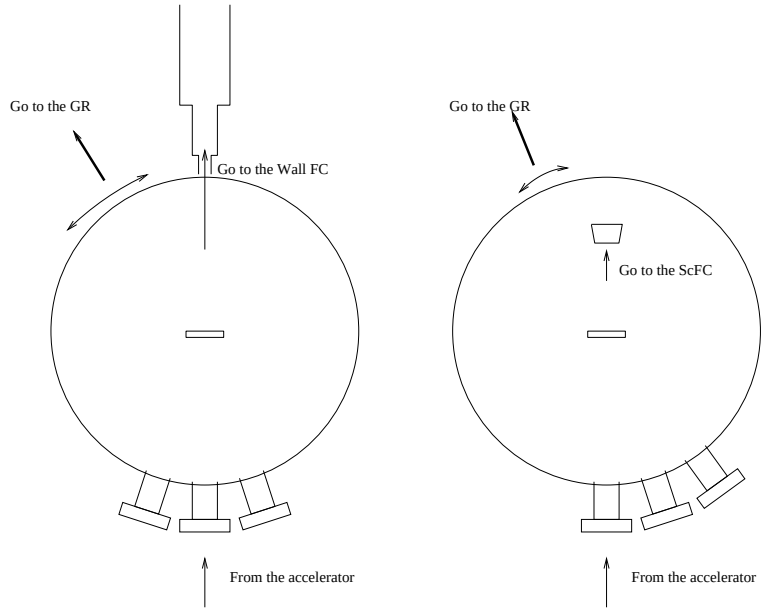

Figure 2.7: Two operation modes of the scattering chamber. The right figure is 'p2p' mode for the backward angle measurement, and the left figure is 'GR mode' for the forward angle measurements.

2.6 Focal plane detectors

At the focal plane of the GR, we placed the focal plane counters which consist of two multi wire drift chambers of vertical-drift type (VDCs) and two plastic scintillating counters (PS1,PS2). Proton scattered from target were momentum-analyzed by the GR.

Specifications of the VDCs are summarized in Table 2.3. Each VDC consists of two anode wire planes (X and U). The structure of an X-wire plane is schematically illustrated in Fig. 2.9. The spacing of sense wires is 6mm for X-planes and 4mm for U-planes shown in Fig. 2.8. The potential wires serve to make a uniform electric field between the cathode plane and the anode plane. High voltages of -300V were supplied to potential wires in both planes for field shaping, while the cathode voltage was -5.6kV and the sense wires were nearly ground voltage. The gas multiplications by avalanche processes only occur near the sense wires. A drift time information from several (three or four) wires are obtained and the trajectory of the scattered particles can be determined.

Gas mixture of argon (71.4%), iso-butane (28.6%), and iso-propyl-alcohol was used. The iso-propyl-alcohol was mixed in the argon gas with vapor pressure at 2°C in order to reduce the deterioration due to the aging effect like the polymerizations of gas on the wire surface. Signals from the sense wires were pre-amplified and discriminated by LeCroy 2735DC card, which were directly connected on the printed bases of the VDCs without cables. Output ECL signals of

2735DC cards were transfered to LeCroy 3377 multihit TDCs, in which information on the hit timing of each wire was digitized.

The drift chambers were backed by two plastic scintillation counters with thicknesses of 10 mm, which size were 1200 mm [Wide] $\times$ 120 mm [Height]. The scintillation light was detected by photo-multiplier tubes (PMT: HAMAMATSU H1161) on both sides of PS1 and PS2. Signals from these scintillators were used to generate a trigger. An aluminum plate with a thickness of 10 mm was placed between PS1 and PS2 to prevent the secondary electrons producted in one scintillator hit another scintillator.

Table 2.3: Design specification of the VDCs

Wire configuration	X(0°), U(-48.2°)
Active area	$1150^{W} \times 120^{H}$ mm
Number of sense wires	192 (X), 208 (U)
Anode-cathode gap	10 mm
Anode wire spacing	2 mm
Sense wire spacing	6 mm (X), 4 mm (U)
Anode sense wires	20 μmϕ gold-plated tungsten wire
Anode potential wires	50 μmϕ gold-plated beryllium copper wire
Cathode film	10 μm carbon-aramid film
Applied voltage	-5600 V (cathode), -300 V(potential), 0 V (sense)
Gas mixture	argon:iso-butane:iso-propyl-alcohol = 71.4:28.6:$*$[1]
Pre-amplifier	LeCroy 2735DC
Digitizer	LeCroy 3377 drift chamber TDC

[1] Mixed with the argon gas in 2°C vapor pressure.

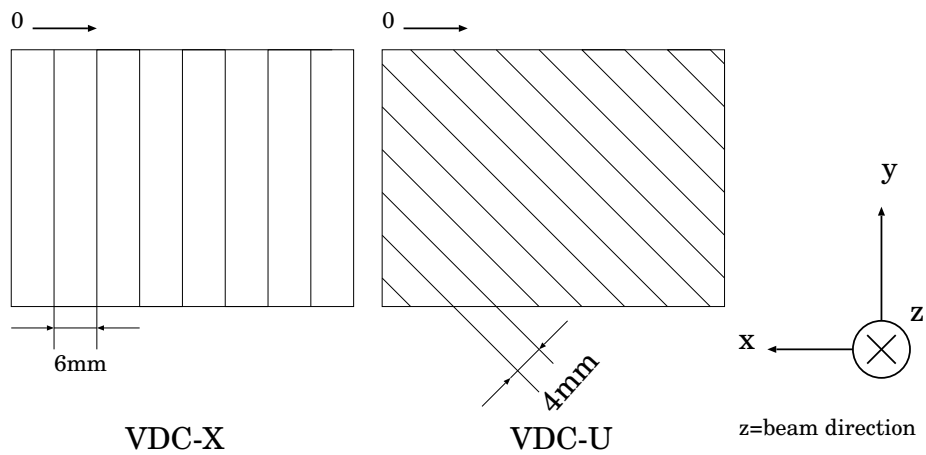

Figure 2.8: Wire configuration of the VDCs for the focal plane detector system of the Grand Raiden spectrometer.

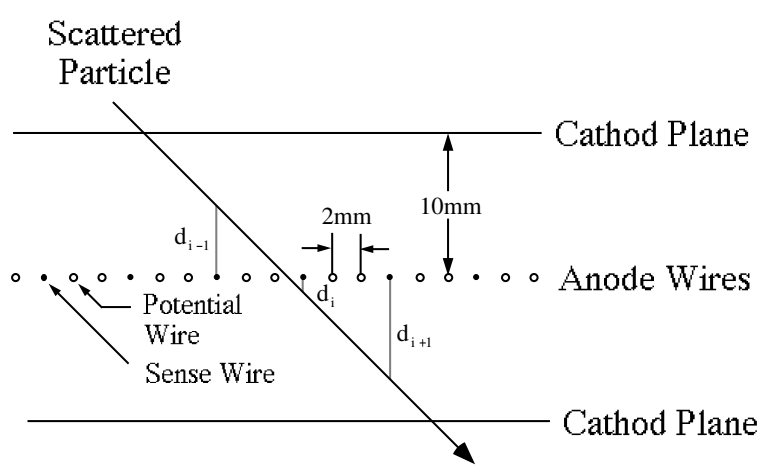

Figure 2.9: Schematic view of an X-plane structure of the VDC. Ionized electrons vertically drift from the cathode plane to the anode wires.

2.7 Trigger system

A schematic diagram of the trigger system of the focal plane scintillators is shown in Fig. 2.10. The system was placed near the focal planes. Outputs of the plastic scintillators were first divided into two signals, one of them was discriminated by a constant fraction discriminator (CFD) (Ortec 935) and the other was sent to a FERA (Fast Encoding and Readout ADC)(LeCroy 4300B) module. One of the CFD outputs was transmitted to the TDC system consisting of TFCs (Time to FERA Converter)(LeCroy 4303) and FERAs. A coincidence signal of the two PMT-outputs on both ends of the same scintillator was generated by a Mean Timer module (REPIC PRN-070), in which the times of two signals were averaged. Thus, the position dependence of output timing due to the difference of the propagation time in the long scintillator was minimized.

The overview of the DAQ system is illustrated in Fig. 2.11. In order to check the consistency of data flow, the event header, event number and input register words were attached to the digitized information from LeCroy 3377, LeCroy 4300B event-by-event in the Flow Controlling Event Tagger (FCET) [48].

The digitized data were transferred in parallel via ECL buses to high speed memory modules (HSM) in a VME crate. The stored data in the HSMs were moved to a VMIC 5576 reflective memory modules (RM5576) through the VME bus by an MC68040 based CPU board, and the data of RM5576 was automatically copied to another RM5576 attached to a SUN work station (SPARC Station 20) in the counting area. The SUN work station plays a important part in the data transfer. The SUN workstation receives data from the VME system by an optical fiber-ring, and transfer them to an IBM RS/6000 workstation operated by the AIX Version 4.3 via an FDDI network. The re-construction of event, the accumulation to disk storage, and distribution of the sampling data for on-line-analysis were managed in this main system.

The live time of the DAQ system was 95% in the case of about 1 kHz trigger events. Beam current was adjusted to maximum current on the condition of more than 90% live time. Experimental condition are summarized in Table 2.4.

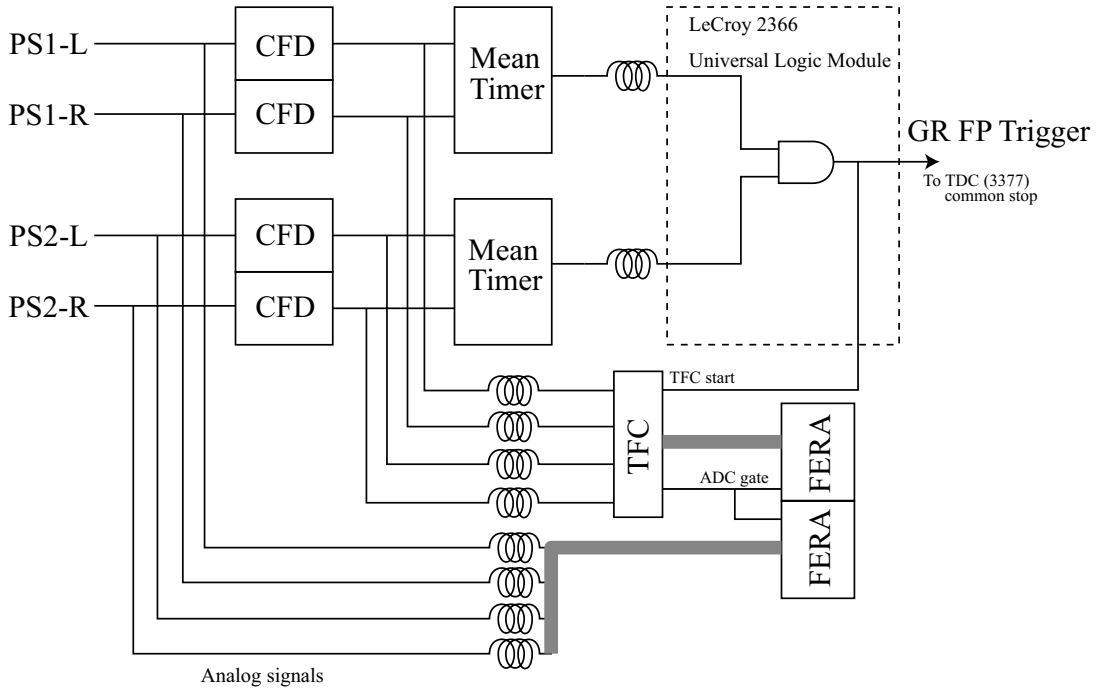

Figure 2.10: Schematic diagram of the trigger circuit.

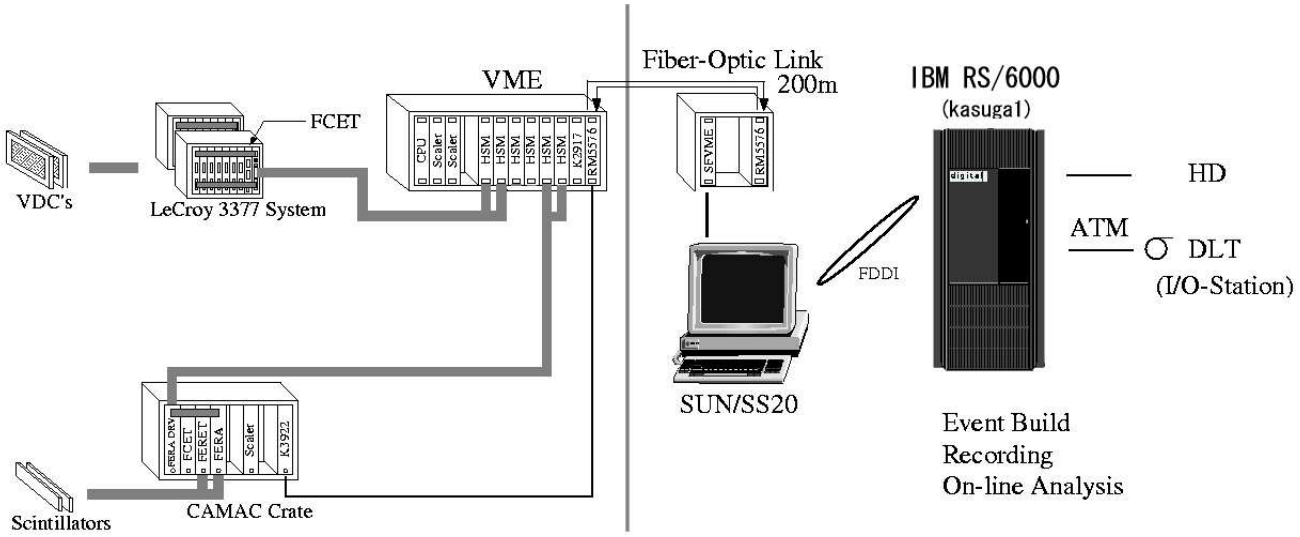

Figure 2.11: Overview of the DAQ system in the West-South (WS) course of RCNP.

Table 2.4: Summary of the experimental conditions.

beam	polarized proton	
beam energy	295	MeV
beam intensity	10-300	nA
beam polarization	0.55-0.7	
target	^{116,118,120,122,124}Sn	
scattering angle	7-50.5	deg.
horizontal acceptance (lab.)	± 20	mrad.
vertical acceptance (lab.)	± 30	mrad.
energy resolution	100-200	keV
FP trigger rate	0.5-3	kHz
DAQ live time(typical)	95	%
Total data size	80	GByte

Chapter 3

Data Reduction

3.1 Analyzer program

A program code for the data analysis has been developed, which is called 'Yosoi-ana' and widely used for analyzing experimental data obtained at WS beam line course of RCNP. The analyzed results were stored in an HBOOK [49] file and graphically displayed using a program PAW [50]. The data analysis was mainly carried out by using the central computer system at RCNP, namely, IBM RS/6000SP system.

3.2 Beam polarization

The beam polarization was measured by using beam line polarimeters (BLP1) placed at the entrance of the west experimental room. Yields on the two pairs of scintillators (N_R, N_L) for spin-up(↑) and spin-down (↓) modes are described as follows;

$$N_L^{\uparrow} = N_L^{\uparrow pro.} - N_L^{\uparrow acc.} = \sigma_0 N_t N_b^{\uparrow} \epsilon_L \Delta\Omega_L (1 + A_y^{\text{eff.}} P_y^{\uparrow}) \tag{3.1}$$

$$N_R^{\uparrow} = N_R^{\uparrow pro.} - N_R^{\uparrow acc.} = \sigma_0 N_t N_b^{\uparrow} \epsilon_R \Delta\Omega_R (1 - A_y^{\text{eff.}} P_y^{\uparrow}) \tag{3.2}$$

$$N_L^{\downarrow} = N_L^{\downarrow pro.} - N_L^{\downarrow acc.} = \sigma_0 N_t N_b^{\downarrow} \epsilon_L \Delta\Omega_L (1 + A_y^{\text{eff.}} P_y^{\downarrow}) \tag{3.3}$$

$$N_R^{\downarrow} = N_R^{\downarrow pro.} - N_R^{\downarrow acc.} = \sigma_0 N_t N_b^{\downarrow} \epsilon_R \Delta\Omega_R (1 - A_y^{\text{eff.}} P_y^{\downarrow}), \tag{3.4}$$

where $N^{pro.}$ and $N^{acc.}$ are the numbers of prompt and accidental coincidence events, σ_0 and A_y are unpolarized cross section and analyzing power for p + p scattering, and N_t and N_0 are numbers of the target and beam particles. P is the beam-polarization vector. ϵ and $\Delta\Omega$ are the efficiency and the solid angle of each scintillation detector, respectively. The accidental coincidence was estimated using the number of forward counter L(R) event coincident with the event of backward counter L'(R') in the next beam bunch.

The angular acceptances of the polarimeter were determined by collimating the backward protons. If there was no instrumental asymmetry, namely $\epsilon_L \Delta\Omega_L = \epsilon_R \Delta\Omega_R = \epsilon \Delta\Omega$, the beam

polarization can be expressed as follows;

$$Py^{\uparrow} = \frac{1}{\mathrm{A_y^{eff.}}} \frac{N_L^{\uparrow} - N_R^{\uparrow}}{N_L^{\uparrow} + N_R^{\uparrow}} \tag{3.5}$$

$$Py^{\downarrow} = \frac{1}{\mathrm{A_y^{eff.}}} \frac{N_L^{\downarrow} - N_R^{\downarrow}}{N_L^{\downarrow} + N_R^{\downarrow}}. \tag{3.6}$$

Here, the value of $\mathrm{A_y^{eff.}}$ is 0.40±0.01. The relative errors from the statistics are determined to be less than 1%. The instrumental asymmetry $\epsilon_L \Delta\Omega_L / \epsilon_R \Delta\Omega_R$ statistically fluctuates about 2-3% in every run. A uncertainty of polarization is typically 2%, whose value is mainly determined by the uncertainty of $\Delta\mathrm{A_y^{eff.}}$=0.01.

3.3 Beam current monitor

In the case of backward measurements, the thick target and the WallFC were used for the proton beam of high intensity (∼1-200nA). The beam passing through the tin targets are transported to Wall FC using five quadrapole magnets. But the transmission of the beam from the target to the WallFC was less than 100 % because of the multiple scattering in the target. The multiple scattering are written as shown in the equation

$$\theta = \frac{13.6 \text{ MeV}}{\beta c p} z \sqrt{x/X_0}[1 + 0.038(x/X_0)] \tag{3.7}$$

$$X_0 = \frac{716.4 \text{ g cm}^{-2} \ A}{Z(Z+1)\ln(287/\sqrt{Z})}, \tag{3.8}$$

where p, β c, z, Z, and A are the momentum (in MeV/c), velocity, charge number of the incident beam, charge, and mass number of the target. Thus a thick ($\geq$ 50 mg/cm^2) and heavy (Z=50) target affect a large multiple scattering to the incident proton. In the ^{116}Sn case whose thickness is 100 mg/cm^2, for example, the value of θ up to 2.0 mrad in plane. The protons passing through the targets partly hit the beam pipes. The vertical counters of the BLP2 were used to monitor the beam current by measuring the ratio of the measured charge by the FC to the yield of the p-p elastic scattering at the BLP2. The yield of the four scintillators of the BLP2 are described as follows;

$$N_U^{\uparrow} = N_U^{\uparrow pro.} - N_U^{\uparrow acc.} = \sigma_0 N_t N_b^{\uparrow} \epsilon \Delta\Omega (1 + A_x^{\mathrm{eff.}} P_x^{\uparrow}) \tag{3.9}$$

$$N_D^{\uparrow} = N_D^{\uparrow pro.} - N_D^{\uparrow acc.} = \sigma_0 N_t N_b^{\uparrow} \epsilon \Delta\Omega (1 - A_x^{\mathrm{eff.}} P_x^{\uparrow}) \tag{3.10}$$

$$N_U^{\downarrow} = N_U^{\downarrow pro.} - N_U^{\downarrow acc.} = \sigma_0 N_t N_b^{\downarrow} \epsilon \Delta\Omega (1 + A_x^{\mathrm{eff.}} P_x^{\downarrow}) \tag{3.11}$$

$$N_D^{\downarrow} = N_D^{\downarrow pro.} - N_D^{\downarrow acc.} = \sigma_0 N_t N_b^{\downarrow} \epsilon \Delta\Omega (1 - A_x^{\mathrm{eff.}} P_x^{\downarrow}), \tag{3.12}$$

where, the notations are similar to the Eq. (3.1-3.4), but U(D) means Up(Down) counters.

Thus we can calculate the number of incident beam N_b as follows;

$$N_U^{\uparrow} + N_D^{\uparrow} = 2\sigma_0 N_t N_b^{\uparrow} \epsilon \Delta\Omega \tag{3.13}$$

$$N_U^{\downarrow} + N_D^{\downarrow} = 2\sigma_0 N_t N_b^{\downarrow} \epsilon \Delta\Omega \tag{3.14}$$

$$N_b^{\uparrow(\downarrow)} = (N_U^{\uparrow(\downarrow)} + N_D^{\uparrow(\downarrow)})/(2\sigma_0 N_t \epsilon \Delta\Omega). \tag{3.15}$$

By assuming the beam transmission from the BLP2 to the ScFC is constant, the corrected charge I_{ScFC} by the ScFC is proportional to the yield in the BLP2. At first, the normalization constant $\mathrm{R}_{\mathrm{ScFC}}$ defined by Eq. (3.16) is checked and determined by forward angle measurements using the ScFC as shown the left side of Fig. 3.1 using the following equation as;

$$\mathrm{R}_{\mathrm{ScFC}}^{\uparrow(\downarrow)} = I_{\mathrm{ScFC}}^{\uparrow(\downarrow)}/N_b^{\uparrow(\downarrow)}. \tag{3.16}$$

The $\mathrm{R}_{\mathrm{ScFC}}$ should be constant if thickness of the target located on the BLP2 and a transmission from the BLP2 to the target are stable. The standard deviation of the $\mathrm{R}_{\mathrm{ScFC}}$ is about 0.6%, which is the same order of the BLP2 statistical uncertainty in the forward angle measurements. Thus, we can use the normalization constant for the monitor of the transmission from the BLP2 to the WallFC.

Next the ratio the collected charge by the ScFC to the WallFC at low beam current was checked as follows;

$$\mathrm{R}_{\mathrm{WallFC}}^{\uparrow(\downarrow)}/\mathrm{R}_{\mathrm{ScFC}}^{\uparrow(\downarrow)} = 0.95 \pm 0.02, \tag{3.17}$$

where,

$$\mathrm{R}_{\mathrm{WallFC}}^{\uparrow(\downarrow)} \equiv I_{\mathrm{WallFC}}^{\uparrow(\downarrow)}/N_b^{\uparrow(\downarrow)}. \tag{3.18}$$

Here, I_{WallFC} is collected charge by the WallFC. The ratio showed a transmissions of about 95% corresponding to a transmission from the target to the WallFC in Fig. 3.1. During this experiment we monitored the transmission using the BLP2 and the WallFC as shown in the right side of Fig. 3.1, and we multiplied the beam current using the WallFC for each targets by $\mathrm{R}_{\mathrm{ScFC}}/\mathrm{R}_{\mathrm{WallFC}}$, where $\mathrm{R}_{\mathrm{ScFC}}$ is the normalization constant, $\mathrm{R}_{\mathrm{WallFC}}$ are calculated by Eq. (3.18) in each run.

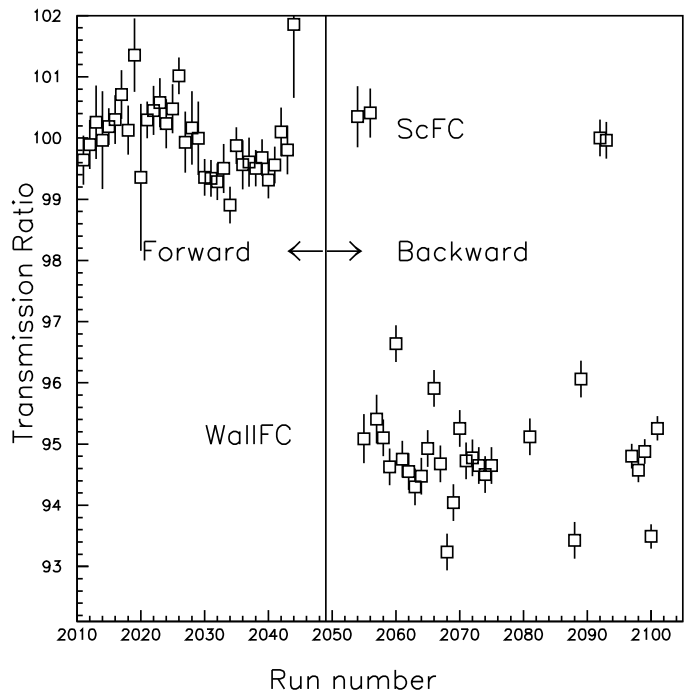

Figure 3.1: The ratios of forward and backward angle measurements in spin-up. Horizontal axis shows run-number corresponding to running time. Statistical fluctuations of each points are less than 0.5%.

3.4 Particle identification

Particle identification (PID) was made using the signals from the two trigger plastic scintillators PS1 and PS2. Scintillating photons of the scintillators were detected by the PMTs attached on the left and the right sides of scintillators. The number of photon is attenuated due to the absorption inside the scintillator during transmission. The photon number *I(x)* can be described as a function of the path length x;

$$I(x) = I_0 \exp(-x/l), \tag{3.19}$$

where I_0 is the initial number of photon and l is the attenuation length of the scintillator. Suppose the distance between the left(right) PMT and the emitting point of the photons are $\mathrm{x}_L(\mathrm{x}_R)$, a geometrical mean I_{mean} of the photon numbers at both sides is shown a mean energy deposition without position dependence;

$$I_{\mathrm{mean}} = \sqrt{I_0 \exp(-\frac{x_L}{l}) \times I_0 \exp(-\frac{x_R}{l})} = I_0 \exp(-\frac{x_L + x_R}{2l}) = I_0 \exp(-\frac{L}{2l}), \tag{3.20}$$

where $L = x_L + x_R$ is the length of the scintillator. The energy deposition of the charged particle in the scintillator is described by the well-known Bethe-Bloch formula [51] as;

$$-\frac{dE}{dx} = 2\pi N_A r_e^2 m_e \rho \frac{Z}{A}\frac{z^2}{\beta^2}\left\{\ln\left(\frac{2m_e\beta^2\gamma^2 W_{max}}{I^2}\right) - 2\beta^2 - \delta - 2\frac{C}{Z}\right\}. \tag{3.21}$$

Here W_{max} is the maximum kinetic energy which can be transfered to a free electron in a single collision, and the notations of other variables are defined as follows:

r_e**:** Classical electron radius (2.817×10^{-13}cm)

m_e**:** Electron mass

N_A**:** Avogadro constant (6.022×10^{23}mol^{-1})

I**:** Mean excitation energy

Z**:** Atomic number of medium

A**:** Atomic mass of medium

ρ**:** Density of medium

z**:** Charge of incident particle

β**:** velocity of incident particle

δ**:** Density effect correction to ionization energy loss

C**:** Shell correction effect.

In this experiment the momenta of scattered particles were limited by the GR momentum acceptance. Thus the velocities of each scattered particle was almost determined [β ~0.65 (proton), 0.39 (deuteron), and 0.27 (triton)], and the energy deposits of deuterons are from two to three times larger than those of protons.

Typical spectrum of particle identification using the PS1 is shown in Fig. 3.2. The gated region of the PID spectrum is indicated by arrows to discriminate deuteron events. In this procedure, the proton events above the right arrow in Fig. 3.2 are also cut off as shown the right-upper panel of Fig. 3.2. Dashed line shows a estimated tail of the proton events. The ratio of such events was estimated to be less than 1%. Figure 3.3 shows the time difference between the main trigger and the AVF cyclotron radio frequency (RF). We can see two peaks in the figure since we have downscaled the RF to a half by a rate divider circuit. The hatched areas in Fig. 3.3 show the spectrum after applying the proton cut on the analog signal. The timing signal was additionally used for PID by cut to the 3-σ region which are indicated by arrows in Fig. 3.3. Figure 3.4 shows the mean analog signal of the PS1 versus the focal plane position. Focal plane measurement will be mentioned in the next section. The mean analog signal of the PS1 is almost independent on the position of the focal plane as shown in Fig. 3.4. The magnetic field was adjusted to locate elastically scattered proton onto the central ray of the magnetic spectrometer. Then the deuterons entered the focal plane as continuum events at this magnetic field.

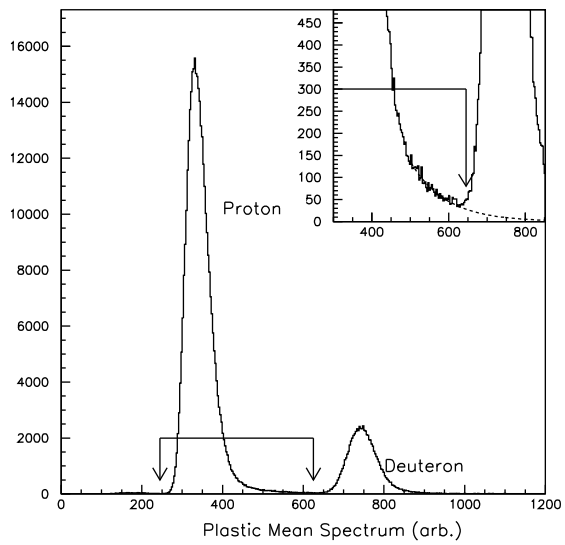

Figure 3.2: PID for proton analog signal from the PS1. Hatched area shows the gated region indicated by arrows. Dashed line in the upper-right panel shows a estimated tail of the proton events.

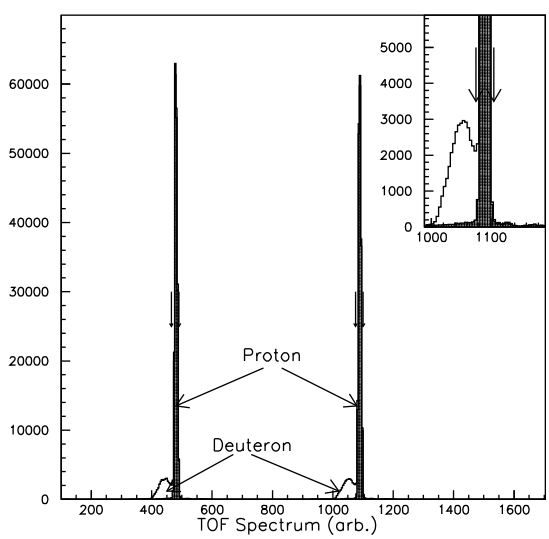

Figure 3.3: PID for proton timing signal from the PS1. Hatched areas show the spectrum after gated by the analog signal of the PS1 in Fig. 3.2.

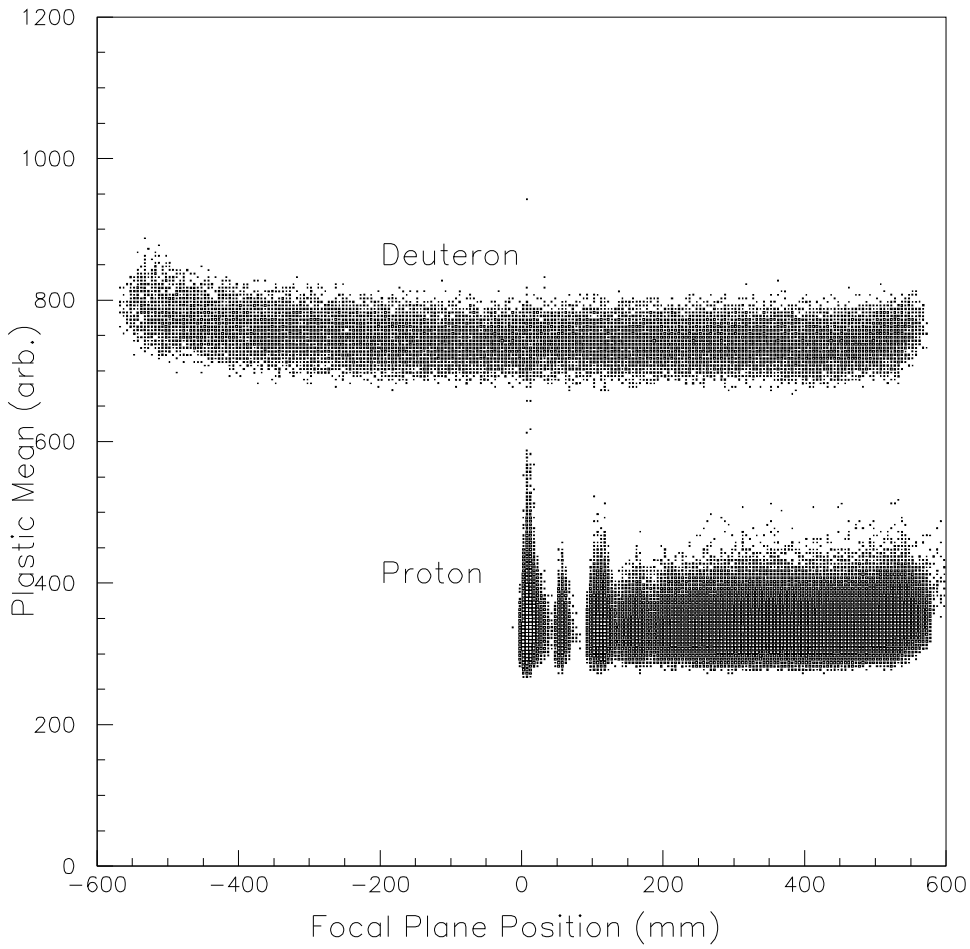

Figure 3.4: Scatter plot of analog signal of the PS1 versus the focal plane position taken at $\theta_{lab.} = 35.5°$. A vertical axis is correspond to Fig. 3.2.

3.5 Track reconstruction

By using the information of two sets of X- and U-positions of anode planes, we can completely determine the three dimensional trajectory of the charged particles. The z-axis is defined as the central ray of the spectrometer. We have constructed the position for the single cluster drift events which have more than two hit wires in a cluster. Figure 3.5 shows a schematic view for a typical one cluster event which consists of three hit wires. This figure is the same as Fig. 2.9. When three or four wires were hit, the position p on the anode plane was calculated using the following equation as;

$$p = p_i + l\frac{d_{i-1} + d_{i+1}}{d_{i-1} - d_{i+1}}, \quad (d_{i-1} > 0 > d_{i+1}) \tag{3.22}$$

where d_{i-1} and d_{i+1} are drift lengths of the i-1 and i+1-th wires located at both sides of i-th wire which had the minimum drift length d_i in a cluster as shown in Fig. 3.5. p_i is the position on the anode plane of i-th wire, l is the sense wire spacing.

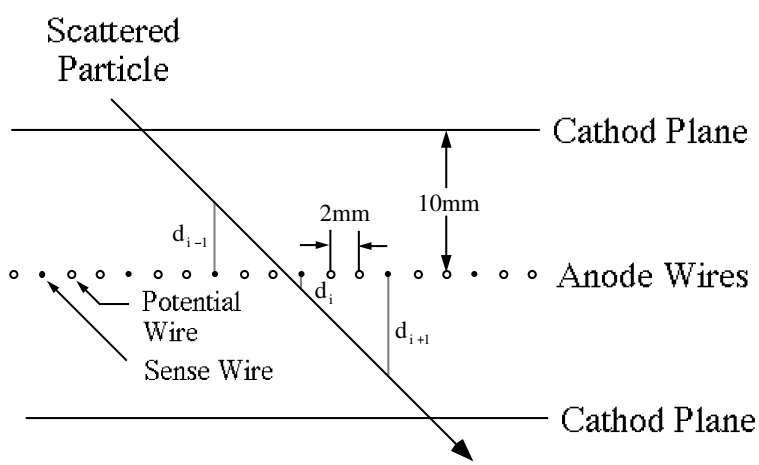

Figure 3.5: Schematic view of an X-plane structure of the VDC. Ionized electrons vertically drift from the cathode plane to the anode wires.

At the case of two wire hit, the events were in a minority. Each wire was assumed to be located opposite side against the anode plane. In the case, the position p was calculated as;

$$p = p_i + l\frac{d_i}{d_{i-1} - d_i}, \quad (d_{i-1} > 0 > d_i) \tag{3.23}$$

where, the notations are the same as Eq. (3.22).

No cluster events and multi-cluster events were dealt as inefficient events. If an anode planes has more than two clusters, the position p is calculated for each cluster. In the analysis, we required that all the anode planes had one cluster or that only one plane had two clusters and

the other three planes had one cluster. Since vertical length of the VDC are not large, the X-position and U-position of single event in the same VDC are strongly correlated. Thus, we chose strongly correlated cluster, and dealt the specific two cluster events as the efficient events.

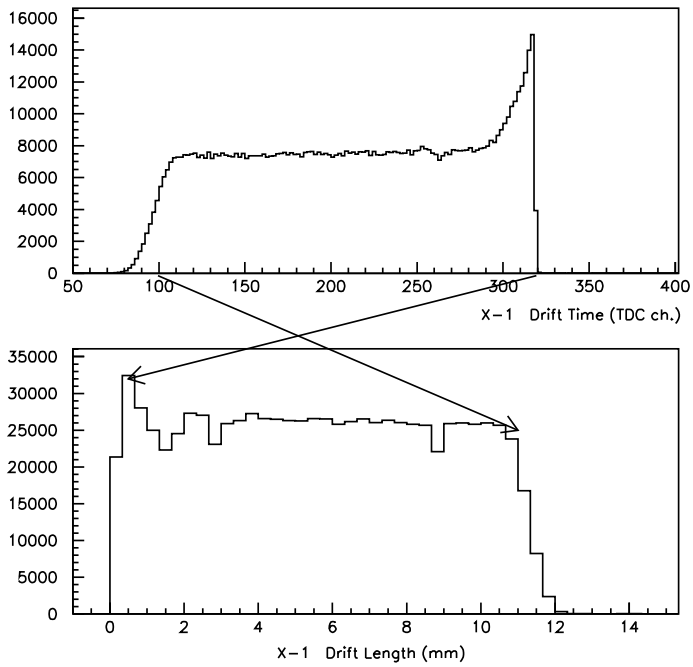

Figure 3.6: Sample spectrum obtained from LeCroy 3377 on X-plane. The TDC signal shown in the upper panel is converted to the drift length shown as the lower panel using time-to-drift relations.

A typical TDC spectrum for X-plane is shown in the upper panel of Fig. 3.6. The TDC signal shown in the upper panel of Fig. 3.6 is converted to the drift length as shown in the lower panel of Fig. 3.6 using the time-to-drift relation. The drift velocity is almost constant except near the sense wires, where drift velocity becomes higher due to the steep gradient of the electric field. Thus the so called time-to-drift relation for each plane is calibrated by using polynomial expression to achieve the uniform residual distributions without position dependences. Typical drift velocity of the uniform region is about 48 μm/ch($\sim$ μm/nsec). The residual distribution is defined as;

$$\text{Residual} : (d_{i-1} + d_{i+1})/2 - d_i. \tag{3.24}$$

A two-dimensional scatter plot for the residual distribution of near the sense wire is shown in Fig. 3.7, where the vertical axis denotes the distance from the sense wire. Typical residual resolution was 350 μm in full width at half maximum (FWHM) as in Fig. 3.8. The intrinsic

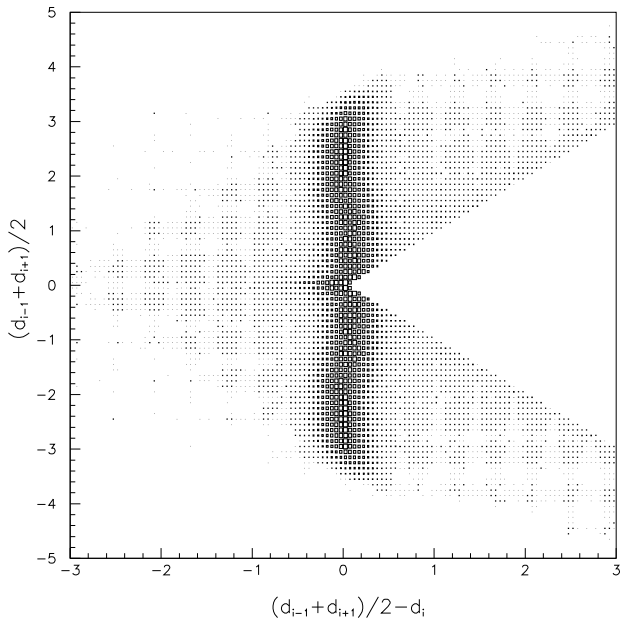

Figure 3.7: Scatter plot of residual resolution versus drift starting position. The residual distributions are almost constant except extremely near the anode wire (± 0.2 mm).

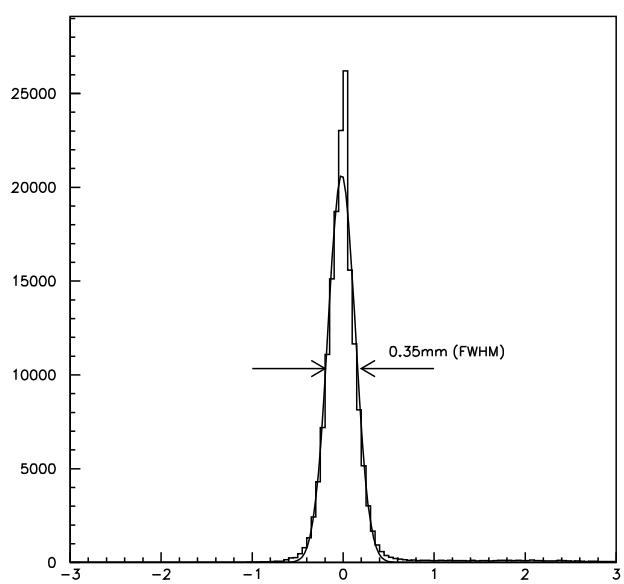

Figure 3.8: Residual resolution correspond to the horizontal projection of Fig. 3.7.

position resolution of each wire is $\sqrt{6}/3$ of the residual resolution, which is analytically deduced if position resolutions of all the wires were same. This position resolution corresponds to less than 10 keV of energy resolution in FWHM.

The trajectories of scattering particle were independently determined Z-X planes and Z-U planes in the central-ray coordinate using X1, X2 planes or U1, U2 planes. The focal plane of the GR is calculated using X1, X2 planes. The trajectory of Z-Y planes were calculated using the information of X- and U-position. Thus a vertical position resolution is about two times worse than a horizontal one. However vertical information hardly affect the energy resolution.

Energy resolution was typically 200 keV in FWHM, and was larger than the expected one deduced from the detector resolution and the resolving power of the GR. It was due to the energy resolution of the beam itself. But for our experiment, it was enough to separate elastic peaks from the inelastic ones.

3.6 Tracking efficiency

For successful reconstruction of the track at each anode plane, it is required that a charged particle hits at least more than two sense wires and makes one cluster. The efficiency of the VDC was calculated as follows;

$$\epsilon_{X1} = \frac{N(X1 \cap U1 \cap X2 \cap U2)}{N(U1 \cap X2 \cap U2)} \tag{3.25}$$

$$\epsilon_{U1} = \frac{N(X1 \cap U1 \cap X2 \cap U2)}{N(X1 \cap X2 \cap U2)} \tag{3.26}$$

$$\epsilon_{X2} = \frac{N(X1 \cap U1 \cap X2 \cap U2)}{N(X1 \cap U1 \cap U2)} \tag{3.27}$$

$$\epsilon_{U2} = \frac{N(X1 \cap U1 \cap X2 \cap U2)}{N(X1 \cap X2 \cap U1)} \tag{3.28}$$

$$\epsilon_{total} = \epsilon_{X1}\ \epsilon_{U1}\ \epsilon_{X2}\ \epsilon_{U2}, \tag{3.29}$$

where $N(X1 \cap U1 \cap X2 \cap U2)$ denotes the number of events in which the positions are successfully determined in all four planes, and $N(U1 \cap X2 \cap U2)$ is the number of events in which the position are determined in three planes except X1-plane, and so on. These efficiencies are calculated for the elastic proton events because the tracking efficiency is depend on the event rate, particle species, and particle energies. Thus, the region where elastic scattering is dominant are roughly selected using the time-difference spectra of the trigger scintillator PS1 whose position resolution was about 2-3 cm at FWHM. Figure 3.9 shows the comparison of the time-difference spectrum with the position spectra at the PS1 position calculated by VDCs. The typical overall tracking efficiency ϵ_{total} of the elastic dominant region was 97%. According to these method, the accidental hit which had one cluster at the each plane was not dealt as inefficiency, and the efficiency had prospect of overestimated. Figure 3.10 shows scatter plot of X-positions using between X1- and X2-position. non-correlated events which are located at the indicated region

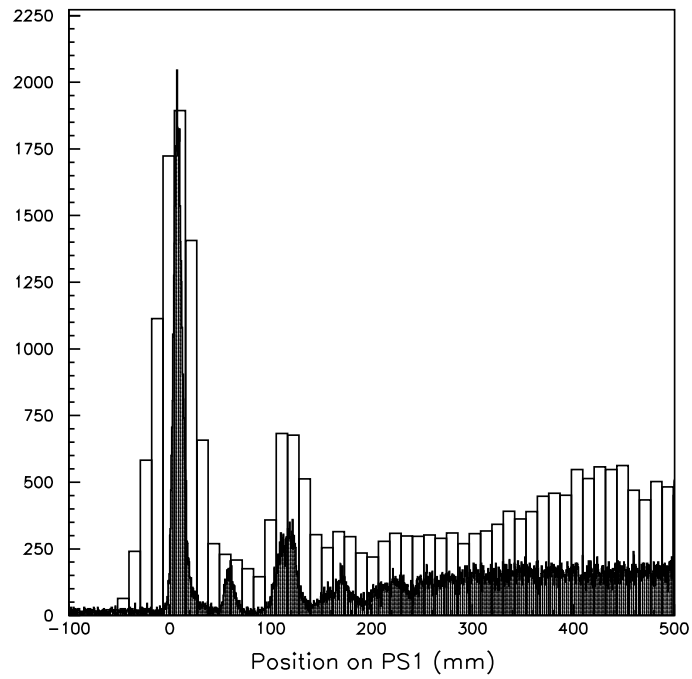

Figure 3.9: Comparison using VDC with the time difference spectrum on the PS1. The hatched histogram show using VDC tracking, and bars show using the time difference of the PS1, and a width of bar shows one channel of the TFC-FERA system.

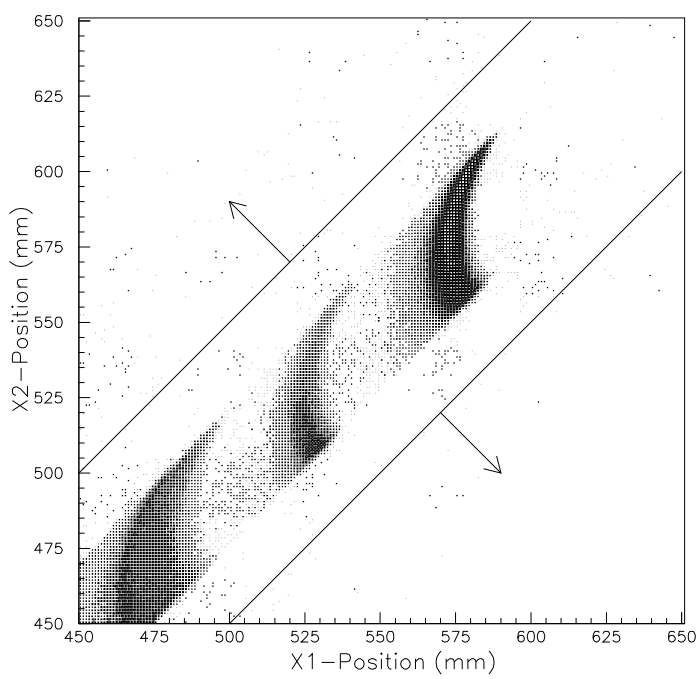

Figure 3.10: Scatter plot of X1- and X2-position using VDCs.

by arrows in Fig. 3.10 slightly existed as accidental events, however, the accidental events were estimated to be less than 0.2 %, and were negligible.

Figure 3.12 shows typical spectra of the ^{116,118,120}Sn run, and the ^{120,122,124}Sn run at 35.5°. Each run was measured in a single data run using the target changing system. The energy resolution of the ^{116,118,120}Sn run in the left panel of Fig. 3.12 is 140 keV in FWHM, and one of the ^{120,122,124}Sn run in the left panel is 250 keV in FWHM. These values were strongly dependent on the beam condition. Each target is selected using the event header signal from the target changing system. The characteristic first excited states in tin isotopes are shown in the ^{116,118,120}Sn run. The characteristic negative parity states in tin isotopes are also shown in the ^{120,122,124}Sn run. The magnetic field of the GR is adjusted for ^{118}Sn in the case of ^{116,118,120}Sn measurement, and for ^{122}Sn in the case of ^{120,122,124}Sn measurement.

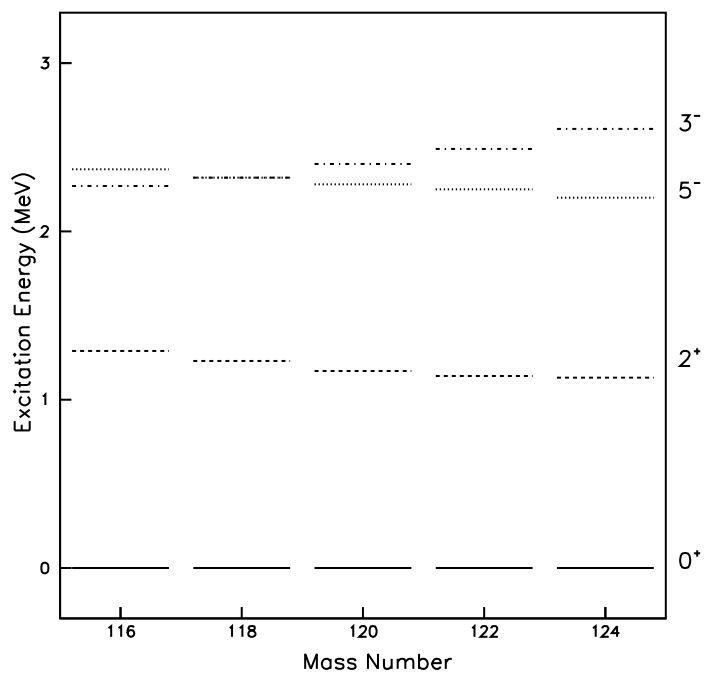

Figure 3.11: Energies of typical excited states for tin isotopes around $\theta_{lab.}$= 35.5°. The solid, dashed, dotted, and dot-dashed lines show ground states 0^+, first excited states 2^+, 5^-, and 3^-, respectively [52].

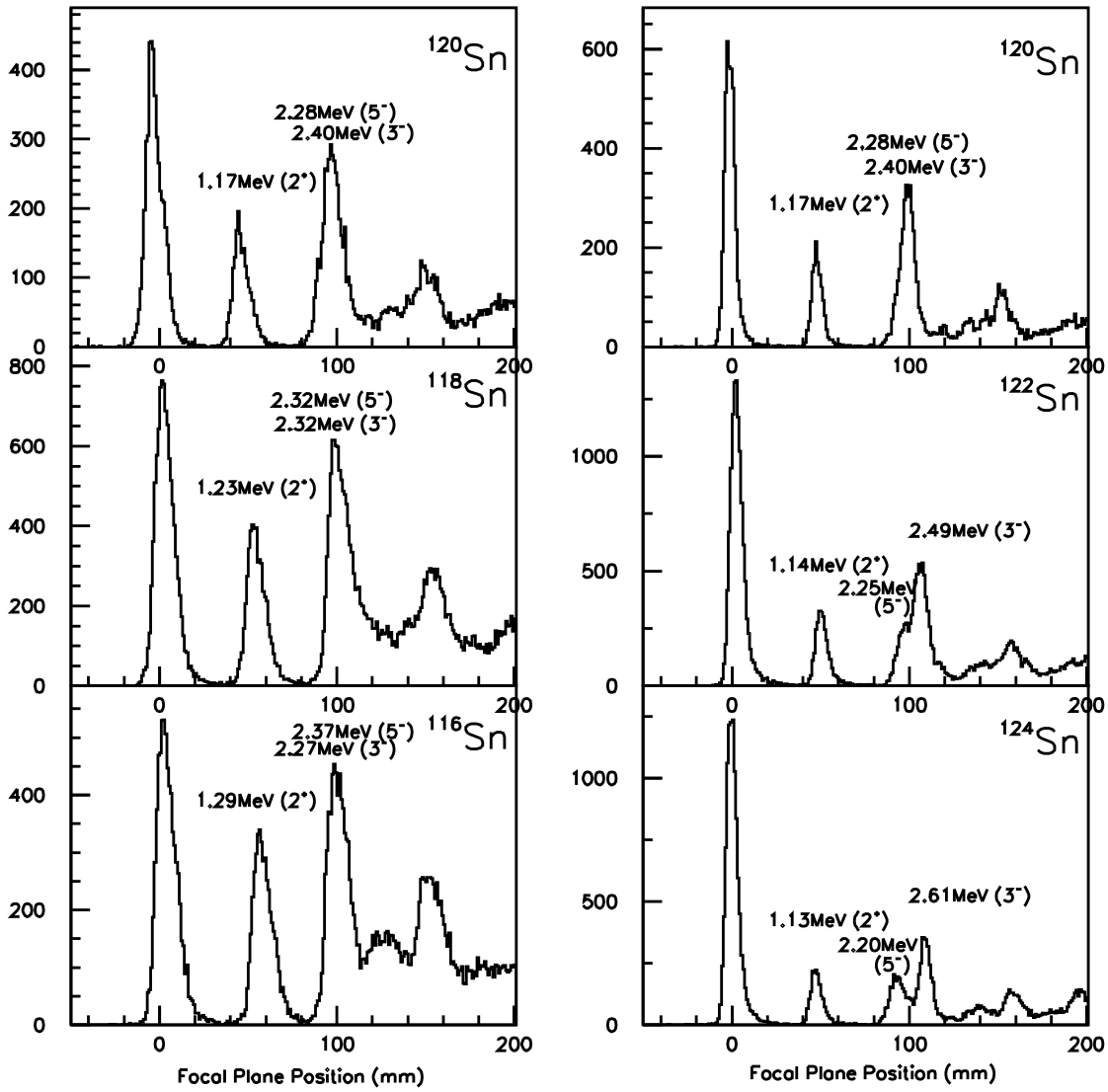

Figure 3.12: Sample focal plane spectra corresponding to the excitation energy of ^{116,118,120}Sn, ^{120,122,124}Sn, taken at a scattering angle $\theta_{lab.}= 35.5°$.

3.7 Acceptance of the spectrometer

The entrance slits are located at the entrance of the GR, whose width is ±20 mrad horizontally and ±30 mrad vertically. The incident angle of scattered particles to the focal detectors were limited from the entranced slit. Using the ion-optical matrix, the angles at the detectors can be traced back up the scattering angles on the target. The angular resolution of this method was horizontally about 0.05° (σ) on target. This value was estimated by folding the square shape by a Monte Carlo simulation. A typical spectrum of scattering angle on the target is shown in Fig. 3.13. Markers show the results of the simulation with 0.05° resolution of angle. This value was overall angular resolution including the tracking resolution of detector itself, the multiple scattering effect at the GR exit window, the higher order aberration of the GR, and the edge scattering effect from the entrance slit of the GR. The horizontal acceptance used ±0.75°, which was calculated from the angle at the focal plane. On the other hand the vertical acceptance was determined by the entrance slit because the vertical angle resolution of the GR was worse due a specific feature of vertical magnification. Thus it was determined by the size of slit ±30 mrad.

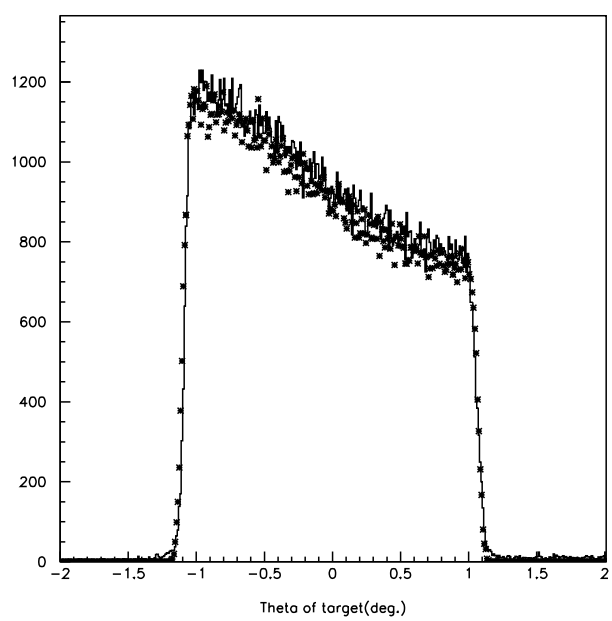

Figure 3.13: Sample spectrum for scattering angle on the target. The symbols show the Monte-Carlo simulation considered to angular resolution in this analysis (∼0.05°).

3.8 Differential cross sections and analyzing powers

Number of elastically scattered protons detected by the VDC can be expressed as;

$$N_{\uparrow} = \frac{d\sigma}{d\Omega}(1 + p_y^{\uparrow} A_y)\Delta\Omega N_t \epsilon^{\uparrow} \lambda^{\uparrow} N_b^{\uparrow}. \tag{3.30}$$

$$N_{\downarrow} = \frac{d\sigma}{d\Omega}(1 + p_y^{\downarrow} A_y)\Delta\Omega N_t \epsilon^{\downarrow} \lambda^{\downarrow} N_b^{\downarrow}. \tag{3.31}$$

where, the notations were almost the same as Eq. (3.1-3.4), however $\Delta\Omega$, ϵ, and λ are the solid angle , the overall detection efficiency, and the live time ratio of the DAQ system, respectively. And the signs of the polarizations were opposite as;

$$p_y^{\uparrow} \geq 0 \geq p_y^{\downarrow}. \tag{3.32}$$

Cross sections and analyzing powers can be deduced by simultaneous Eq. (3.30);

$$\frac{d\sigma}{d\Omega} = \frac{1}{p_y^{\uparrow} - p_y^{\downarrow}}\left(\frac{N^{\downarrow} p_y^{\downarrow}}{\epsilon^{\downarrow}\lambda^{\downarrow} N_b^{\downarrow}} - \frac{N^{\uparrow} p_y^{\uparrow}}{\epsilon^{\uparrow}\lambda^{\uparrow} N_b^{\uparrow}}\right)\frac{1}{\Delta\Omega N_t}, \tag{3.33}$$

$$A_y = \frac{1-\alpha}{\alpha p_y^{\uparrow} - p_y^{\downarrow}} \tag{3.34}$$

where

$$\alpha \equiv \frac{N^{\downarrow}}{Q^{\downarrow}\epsilon^{\downarrow}\lambda^{\downarrow} N_b^{\downarrow}} \Big/ \frac{N^{\uparrow}}{Q^{\uparrow}\epsilon^{\uparrow}\lambda^{\downarrow} N_b^{\uparrow}}. \tag{3.35}$$

Statistical errors can be estimated as

$$\begin{aligned} \Delta\frac{d\sigma}{d\Omega} &= \frac{d\sigma}{d\Omega} \times \frac{1}{p_y^{\uparrow} - p_y^{\downarrow}} \times \frac{1}{\alpha p_y^{\uparrow} - p_y^{\downarrow}} \\ &\quad \times (1-\alpha)^2((p_y^{\downarrow}\Delta p_y^{\uparrow})^2 + (p_y^{\uparrow}\Delta p_y^{\downarrow})^2) \\ &\quad + (p_y^{\uparrow} - p_y^{\downarrow})^2\left(\frac{p_y^{\downarrow 2}}{N^{\uparrow}} + \frac{\alpha^2 p_y^{\downarrow 2}}{N^{\downarrow}}\right)^{1/2} \end{aligned} \tag{3.36}$$

$$\begin{aligned} \Delta A_y &= \frac{1}{(\alpha p_y^{\uparrow} - p_y^{\downarrow})^2}((1-\alpha)^2(\alpha^2 \Delta p_y^{\uparrow 2} + \Delta p_y^{\downarrow 2}) \\ &\quad + \alpha^2 (p_y^{\uparrow} - p_y^{\downarrow})^2\left(\frac{1}{N^{\uparrow}} + \frac{1}{N^{\downarrow}}\right))^{1/2}. \end{aligned} \tag{3.37}$$

Here, the statistical fluctuation for number of beam $N_b^{\uparrow(\downarrow)}$ is smaller than number of elastically scattered proton $N^{\uparrow(\downarrow)}$, and is negligible for the statistical error $\Delta\frac{d\sigma}{d\Omega}$. Uncertainties of analyzing power ΔA_y are mainly determined by the uncertainty of polarization, typically 2% for $\Delta \mathrm{p}_y$. and the statistical fluctuation term of $1/\sqrt{N}$ for ΔA_y is relatively small in this measurement.

3.9 Experimental results

Differential cross sections and the analyzing power were measured up to 50 degrees corresponding to momentum transfer of 3.5 fm^{-1} in the center-of-mass system. Uncertainties in the experimental data are mainly due to inhomogeneities of the target foil thickness and are not due to counting statistics. Therefore, the experimental uncertainties are added $\pm 3\%$ to both cross sections and analyzing powers as systematic uncertainties. The experimental results of the cross sections and the analyzing powers are shown in Fig. 3.14 together with the model calculations. The details of the calculation are shown in the next chapter, and the digital data are summarized in Appendix A.

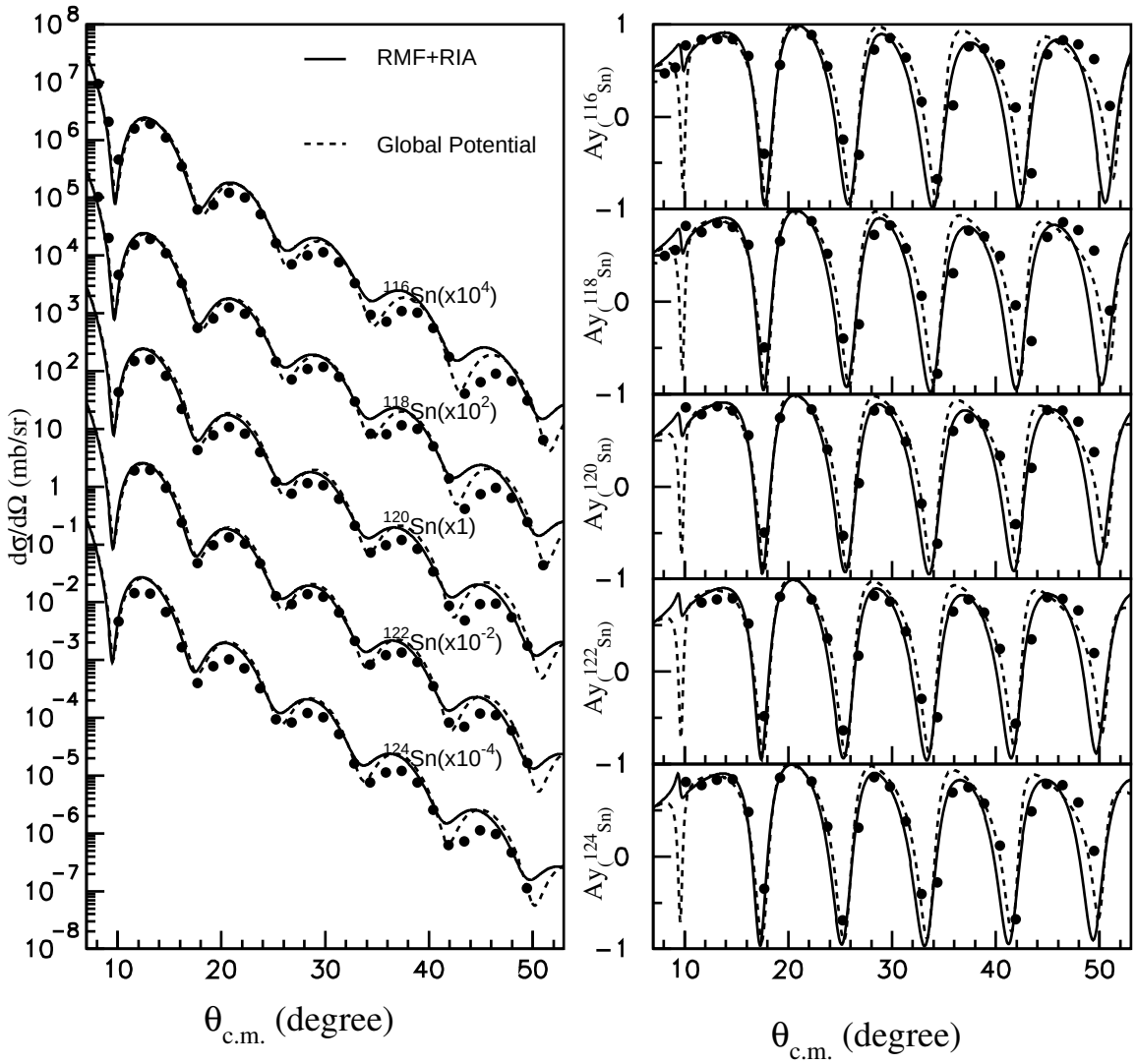

Figure 3.14: Differential cross sections and analyzing powers for proton elastic scattering from tin target. The solid curves are the original RIA calculations of Murdock and Horowitz [35], while dashed lines are calculations from the Dirac global potential [53, 54].

Chapter 4

Analysis

4.1 Historical background of the relativistic approach

Since 1980s, relativistic approaches based on Dirac equations have been applied to the elastic scattering of intermediate energy protons, and have been successfully explaining the scattering, especially polarization observables. Clark *et al.* have extended the Dirac phenomenology as the global potential, which has been able to explain elastic proton scattering of spin zero nuclei for the mass number of $12 \leq \mathrm{A} \leq 208$ from 20 MeV to 1040 MeV [53, 54]. It was a great success to explain proton elastic scattering in a wide mass- and energy-range, however, the physical meaning of the parameters was not clear. More fundamental approach has been presented by McNeil, Shepard, and Wallece who have also found a dramatic improvements for spin dependent observables for ^{16}O and ^{40}Ca at 500 MeV using the Dirac equation [55]. They have applied impulse approximation to the Dirac approach, where the Lorentz invariant amplitude has been expressed as;

$$\begin{aligned} F(q) &= F^S + F^V \gamma^\mu_{(0)} \gamma^\mu_{(1)} + F^{PS} \gamma^5_{(0)} \gamma^5_{(1)} \\ &\quad + F^T \sigma^{\mu\nu}_{(0)} \sigma_{(1)\mu\nu} + F^A \gamma^5_{(0)} \gamma^\mu_{(0)} \gamma^5_{(1)} \gamma_{(1)\mu}, \end{aligned} \tag{4.1}$$

and the amplitude has been directly determined from nucleon-nucleon phase shift analyses. They have showed the superiority of the relativistic impulse approximation than the non-relativistic t-matrix one.

4.2 Relativistic impulse approximation

Our experimental data have been analyzed on the formalism of the relativistic impulse approximation (RIA) using the relativistic Love-Franey (RLF) interaction [35]. Murdock and Horowitz have calculated the elastic scattering of ^{16}O, ^{40,48}Ca, ^{90}Zr, and ^{208}Pb at the energies from 200 MeV to 400 MeV using the RLF interaction treating explicitly the exchange term. They have introduced ten mesons, for example π, η, σ, ω, and ρ, as exchanged mesons.

Each Lorentz invariant amplitude F^L in the Eq. (4.1) is described as;

$$F^L = \mathrm{i}\frac{M^2}{2E_c k_c}[F_D^L(q) + F_X^L(Q)] \tag{4.2}$$

$$F_D^L(q) \equiv \sum_j \delta_{L,L(j)}(\boldsymbol{\tau_0}\cdot\boldsymbol{\tau_1})^{I_j} f^j(q), \tag{4.3}$$

$$F_X^L(Q) \equiv (-1)^T \sum_j B_{L(j),L}(\boldsymbol{\tau_0}\cdot\boldsymbol{\tau_1})^{I_j} f^j(Q), \tag{4.4}$$

$$\tag{4.5}$$

Here, T is the total isospin of the two-nucleon state, *L(j)* denotes the spin and parity of the *i*-th meson, I_j is the isospin of the *j*-th meson. q and Q are direct and exchange momentum transfers, E_c is the total energy, and k_c is the relative momentum in the nucleon-nucleon center of mass system. B is the Fierz transformation matrix. Each amplitude $f^i(q)$ is shown as the sum of real and imaginary amplitudes using masses m_i, coupling constants g_i, and cutoff parameters λ_i of the exchanged *i*-th meson in following equation;

$$f^i(q) \equiv \frac{g_i^2}{\boldsymbol{q}^2 + m_i^2}\left(\frac{\lambda_i^2}{\lambda_i^2 + \boldsymbol{q}^2}\right) - \mathrm{i}\frac{\bar{g}_i^2}{\boldsymbol{q}^2 + \bar{m}_i^2}\left(\frac{\bar{\lambda}_i^2}{\bar{\lambda}_i^2 + \boldsymbol{q}^2}\right). \tag{4.6}$$

The first-order Dirac optical potentials for the spherical nuclei are produced by folding this *NN* amplitude with the target densities;

$$U^L(r,E) = U_D^L(r,E) + U_X^L(r,E) \tag{4.7}$$

$$U_D^L(r,E) \equiv -\frac{4\pi \mathrm{i} p}{M}\int d\boldsymbol{r}'\rho(\boldsymbol{r}')t_D^L(|\boldsymbol{r}'-\boldsymbol{r}|,E) \tag{4.8}$$

$$U_X^L(r,E) \equiv -\frac{4\pi \mathrm{i} p}{M}\int d\boldsymbol{r}'\rho(\boldsymbol{r}')t_X^L(|\boldsymbol{r}'-\boldsymbol{r}|,E)\ j_0(p|\boldsymbol{r}'-\boldsymbol{r}|), \tag{4.9}$$

where $t_D^L(|\boldsymbol{r}|,E)$ are Fourier transforms of $t_D^L(q,E) \equiv (iM^2/2E_c k_c)F_D^L(q)$ and similarly for the exchange pieces $t_X^L(Q,E)$, and $\rho(\boldsymbol{r})$ are target density. For a spin zero nucleus, the only nonzero densities are scalar, vector, and tensor densities. The tensor contribution is found to be small and is neglected. Thus only scalar and vector densities are taken into account for the RIA calculation in this work.

Figure 3.14 shows the results from two theoretical calculations and our experimental data. Solid lines are the RIA calculations using the RLF interaction, where densities are taken from the relativistic Hartree calculations [56]. Dashed lines are calculations using the global potential based on Dirac phenomenology [53, 54]. The results of the RIA calculations are in agreement with our data of cross sections at forward angles, but it is overestimated at backward angles. On the other hand, the analyzing powers are well reproduced. The calculations by the global potential reproduce cross sections, but there are large deviations in analyzing powers at forward angle ($\sim$10°).

4.3 Medium effects

Murdock and Horowitz approximatively introduced a phenomenological energy-dependent "Pauli blocking" factors, whose functional form is considered based on the Bruckner theory [35]. Recently Sakaguchi *et al.* modified the RIA calculation more microscopically, namely the nucleon-nucleon interaction level. It is because that the properties of hadron such as the masses and the coupling constants can change in the nuclear medium due to the interaction with the hadrons [57]. These changes in the masses and coupling constants are called "medium effects", and may be an effect of the presentations of the partial restoration of chiral symmetry [58], Pauli blocking [35], vacuum polarization [59], multistep process [60], and few-nucleon force. They attempted to explain the experimental data by phenomenologically changing the masses and coupling constants of exchanged mesons (σ and ω) in the real and the imaginary amplitudes of Eq. (4.6) depending the nuclear densities. They expanded the meson propagator in the amplitudes of Eq. (4.6) up to second order in $\boldsymbol{q}^2$ and ρ as;

$$\begin{aligned}
\frac{g_i^2}{\boldsymbol{q}^2+m_i^2} &=> \frac{g_i^2}{\boldsymbol{q}^2+m_i^2+b(\rho/\rho_0)+a(\rho/\rho_0)\boldsymbol{q}^2} \\
&= \frac{g_i^2}{\boldsymbol{q}^2(1+a(\rho/\rho_0))+m_i^2+b(\rho/\rho_0)} \\
&= \frac{g_i^2/(1+a(\rho/\rho_0))}{\boldsymbol{q}^2+m_i^2(1+b'(\rho/\rho_0))/(1+a(\rho/\rho_0))} \\
&= \frac{g_i^{*2}}{\boldsymbol{q}^2+m^{*2}}, \qquad (4.10)
\end{aligned}$$

where

$$\begin{aligned}
g^{*2} &\equiv \frac{g^2}{1+a\rho/\rho_0} \\
m^* &\equiv m\sqrt{\frac{1+b'\rho/\rho_0}{1+a\rho/\rho_0}} \\
&\cong m(1+b''\rho/\rho_0) \\
b' &\equiv \frac{b}{m_i^2} \\
b'' &\sim \frac{b'-a}{2}.
\end{aligned}$$

Here, ρ and ρ_0 show a matter density distribution and its normal density.

The functional form of density dependence is described as follows;

$$\begin{aligned}
g_j^2,\ \bar{g}_j^2 &\longrightarrow \frac{g_j^2}{1+a_j\ \rho(r)/\rho_0},\ \frac{\bar{g}_j^2}{1+\bar{a}_j\ \rho(r)/\rho_0} \\
m_j,\ \bar{m}_j &\longrightarrow m_j[1+b_j\ \rho(r)/\rho_0],\ \bar{m}_j[1+\bar{b}_j\ \rho(r)/\rho_0], \qquad (4.11)
\end{aligned}$$

where j refers to the σ and ω mesons. m_j, $\bar{m}_j$, g_j, and $\bar{g}_j$ indicate the masses, and coupling constants of mesons for real and imaginary amplitudes, respectively. The normal density ρ_0 was taken to be 0.1934 fm^{-3} [36, 59].

In this work, we have refined treatments for point proton density to deduce systematic errors of the neutron density distributions, and the detail is discussed in the following Sec. 4.4. And we have carefully analyzed effects of several assumptions and errors to calculate the neutron density distributions; the effect of scalar density is discussed in Sec. 4.5. the effect of our introduced modification parameter errors is discussed in Sec. 4.6 and Sec. 4.7.

4.4 Proton density distributions of tin isotopes

In this section, we discuss treatments of the point density distributions of tin isotopes in the RIA calculation. In the RIA calculations, point proton density distributions derived from charge distributions are used. To reduce a systematic error of proton density distribution, we need a better charge distribution. Until now, charge distribution for stable nuclei have been studied using several model-dependent and -independent densities. Existing charge distribution data for tin isotopes are summarized in Table 4.1. As for the charge distribution for tin isotopes, two model-dependent densities and one model-independent density are reported [3, 7].

The model-dependent two-parameter Fermion (2pF) function is written as;

$$\rho_{ch}(r) = \rho_0 \frac{1}{1+e^{(r-c)/z}}, \tag{4.12}$$

where c and z correspond to a radial and a surface parameter, respectively. And another model-dependent three-parameter Gaussian (3pG) function is described as;

$$\rho_{ch}(r) = \rho_0 \frac{1+wr^2/c^2}{1+e^{(r^2-c^2)/z^2}}, \tag{4.13}$$

where w corresponds to an inner depth parameter, and a normalization condition is shown as;

$$\int \rho_{ch}(r) d\boldsymbol{r} = Z. \tag{4.14}$$

a normal density ρ_0 is determined to satisfy Eq. (4.14). The model-independent Sum-of-Gaussian (SOG) charge distribution is described as;

$$\begin{aligned} \rho_{ch}(r) &= \frac{Z}{2\pi^{3/2}\gamma^3} \sum_{i=1}^{12} \frac{Q_i}{1+2R_i^2/\gamma^2} \\ &\quad \times \left[e^{-(r-R_i)^2/\gamma^2} + e^{-(r+R_i)^2/\gamma^2} \right], \end{aligned} \tag{4.15}$$

where, a normalization condition Eq. (4.14) is rewritten as;

$$\int \rho_{ch}(r) d\boldsymbol{r} = Z, \quad \Rightarrow \quad \int Q_i = 1. \tag{4.16}$$

In the case of ^{116,124}Sn model-independent densities are reported. In this case, the SOG charge distributions of ^{116,124}Sn are used, which were obtained from the electron scattering up to the high momentum transfer of 3.6 fm^{-1} [5].

Figure 4.1 shows a comparison of charge distribution of ^{124}Sn between model-independent density (SOG) with other model-dependent densities (2pF, 3pG) [3, 7].

The model-dependent charge distribution using 3pG is in good agreement with the model-independent charge distribution at a surface and tail region. However a density using 3pG does not describe the form factor of model-independent functional shape at the high momentum transfer region (>2.5 fm^{-1}) as shown in Fig. 4.2, since the SOG charge distribution for ^{124}Sn reproduces the experimental data up to the high momentum transfer [62]. The deviation is corresponding to inner region less than 4 fm in Fig. 4.1. And the deviation of 2pF in Fig. 4.1 is corresponding to less than 5 fm. It means that it is difficult to extrapolate toward a high momentum transfer region using the model-dependent density, and it is not neglected to remain the constraint of the model-dependent density.

Table 4.1: The summary of exiting charge distributions data using model-dependent and -independent functional shapes of even-even tin isotopes.

Nuclei	Model	RMS radius (fm)	q-range (fm^{-1})	Year
^{112}Sn	2pF	4.655(23)	0.49-1.40	1970 [3, 7]
	3pG	4.586(5)	0.64-2.37	1972 [3, 7]^{*1}
^{114}Sn	3pG	4.602(5)	0.64-2.37	1972 [3, 7]^{*1}
^{116}Sn	2pF	4.551	0.46-1.08	1967 [3]
	2pF	4.62	0.35-0.59	1969 [3]
	2pF	4.673(16)	0.84-1.98	1972 [3]
	2pF	4.626(15)	0.36-1.00	1976 [3, 7]
	3pG	4.619(5)	0.64-2.65	1972 [3, 7]^{*1}
	SOG	4.627(3)	0.36-3.60	1982 [7]^{*2}
^{118}Sn	2pF	4.64	0.35-0.59	1969 [3]
	2pF	4.679(16)	0.49-1.40	1970 [3, 7]
	2pF	4.676(17)	0.84-1.75	1972 [3, 7]
	3pG	4.634(5)	0.64-2.37	1972 [3, 7]^{*1}
^{120}Sn	2pF	4.640	0.46-1.08	1967 [3, 7]
	2pF	4.64	0.35-0.59	1969 [3]
	3pG	4.646(5)	0.64-2.37	1972 [3, 7]^{*1}
^{122}Sn	3pG	4.658(5)	0.64-2.37	1972 [3, 7]^{*1}
^{124}Sn	2pF	4.666	0.64-2.37	1967 [7]
	2pF	4.64	0.35-1.59	1969 [7]
	2pF	4.695(17)	0.84-1.75	1972 [3, 7]^{*1}
	3pG	4.670(5)	0.64-2.65	1972 [3, 7]^{*1}
	SOG	4.677(3)	0.36-3.60	1982 [7]^{*2}

^{*1}Including the result from optical isotope shifts data [61].
^{*2}Including the result from muonic atom data [62].

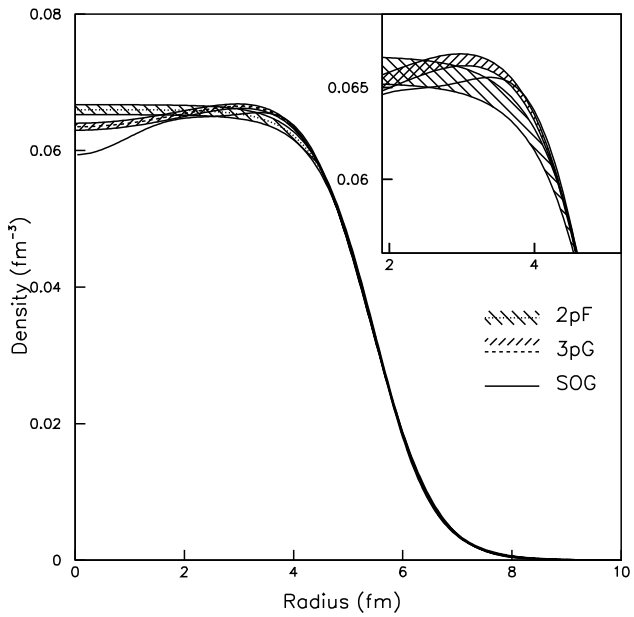

Figure 4.1: The comparison existing charge distributions of ^{124}Sn using different functional shapes, 2pF, 3pG, and SOG. The right-upper panel is enlarged view at a shoulder region (2-5 fm) in this figure.

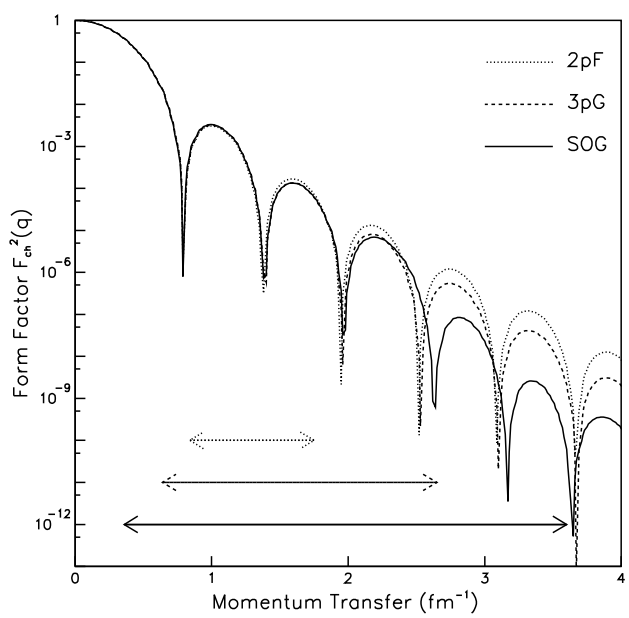

Figure 4.2: The sample calculation of a electric form factor of ^{124}Sn which is transformed from existing charge distributions of Fig. 4.1. Arrows show momentum transfer regions of use data sets which are shown in Table 4.1.

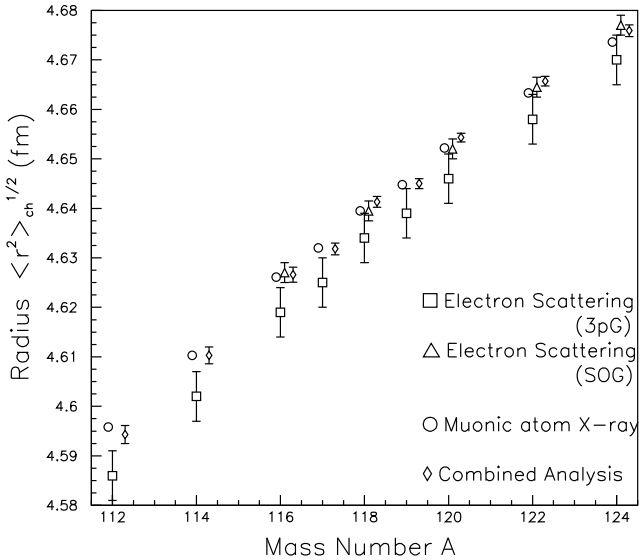

Figure 4.3: The charge radius of tin isotopes. Squares and triangles are results from electron elastic scattering using different model distributions [3, 7]. Here, the SOG data of ^{116,124}Sn are existing ones from Ref. [7], and the other SOG data for ^{118,120,122}Sn are interpolated using Eq. (4.17-4.19). Circles are results from muonic X-ray data [63]. Diamonds are combined results from both electron scattering and muonic X-ray data [64].

Figure 4.3 shows the existing experimental root mean squared (RMS) radii of the charge distributions for tin isotopes. The charge radius of the tin isotope increases smoothly with mass number, while the number of protons is constant and magic number. Thus a smooth change in the charge distributions with the neutron number can be expected. We interpolated the charge distributions of ^{118,120,122}Sn using the arithmetic mean of the SOG type charge distributions of ^{116,124}Sn;

$$\rho_{ch}^{118\mathrm{Sn}}(r) = \frac{3\rho_{ch}^{116\mathrm{Sn}}(r) + \rho_{ch}^{124\mathrm{Sn}}(r)}{4} \tag{4.17}$$

$$\rho_{ch}^{120\mathrm{Sn}}(r) = \frac{\rho_{ch}^{116\mathrm{Sn}}(r) + \rho_{ch}^{124\mathrm{Sn}}(r)}{2} \tag{4.18}$$

$$\rho_{ch}^{122\mathrm{Sn}}(r) = \frac{\rho_{ch}^{116\mathrm{Sn}}(r) + 3\rho_{ch}^{124\mathrm{Sn}}(r)}{4}. \tag{4.19}$$

As shown in Fig. 4.5, the interpolated charge distributions change smoothly similar to the experimentally extracted 3pG model densities in Fig. 4.4. The interpolated radii of model-independent-type charge distributions for ^{118,120,122}Sn are consistent with other experimental data obtained from the electron scattering and muonic X-rays as shown in Fig. 4.3. Figure 4.6 shows the differences between interpolated radii and other results from the 3pG electron scattering data, the muonic X-ray data, and the combined analyses of elastic electron scattering [64].

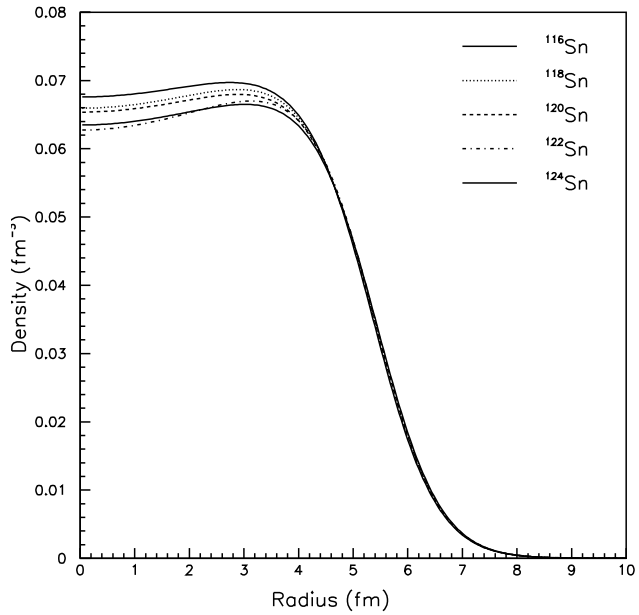

Figure 4.4: The existing charge distribution of tin isotopes using 3pG functional shape.

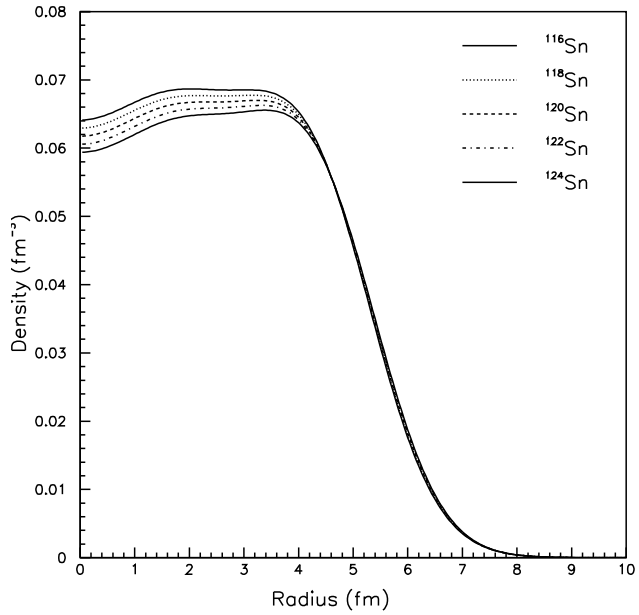

Figure 4.5: The existing charge distribution of ^{116,124}Sn using SOG functional shape, and the deduced charge distribution of ^{118,120,122}Sn from Eq. (4.17).

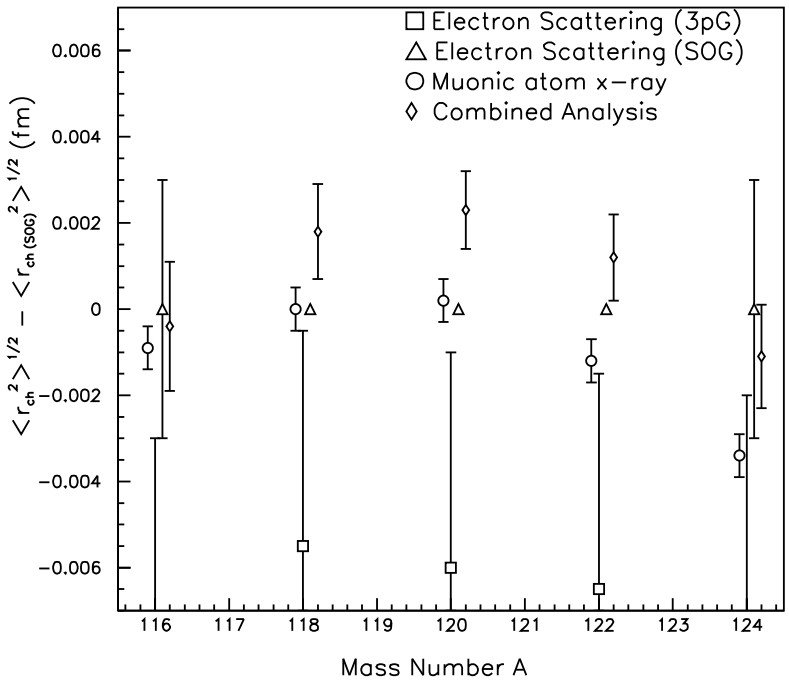

Figure 4.6: The difference of charge RMS radii from SOG charge RMS radius for tin isotopes. The notations are in same as in Fig. 4.3.

The dependence for the differences with mass number slightly shows, however the differences are very small as shown in Fig. 4.6. The errors of our interpolated charge radii are estimated to be 0.003 fm. Their values are in the same value as for ^{116,124}Sn.

In the report by Sakaguchi *et al.* [36], the point proton distribution was extracted by unfolding the charge distribution by the charge distribution of proton itself, neglecting the charge distribution of neutron itself. In this paper, we have also considered the charge distribution of neutron itself. Thus, a charge distribution is expressed as follows;

$$\rho_{ch}(\boldsymbol{r}) = \int \rho_p(\boldsymbol{r}')\rho_{ch}^{\text{proton}}(\boldsymbol{r}-\boldsymbol{r}')d\boldsymbol{r}' + \int \rho_n(\boldsymbol{r}'')\rho_{ch}^{\text{neutron}}(\boldsymbol{r}-\boldsymbol{r}'')d\boldsymbol{r}'', \tag{4.20}$$

where, ρ_{ch}, ρ_p, ρ_n, $\rho_{ch}^{\text{proton}}$, and $\rho_{ch}^{\text{neutron}}$ indicate charge distribution, point proton density distribution, point neutron density and charge distribution of proton, and neutron themselves. And a mean squared (MS) radius of charge distribution can be written using a point proton MS radius and a MS radius of proton and neutron charge distribution as follows;

$$\left\langle r_{ch}^2 \right\rangle = \left\langle r_p^2 \right\rangle + \left\langle (r_{ch}^{\text{proton}})^2 \right\rangle + \frac{N}{Z}\left\langle (r_{ch}^{\text{neutron}})^2 \right\rangle, \tag{4.21}$$

where

$$\begin{aligned}
\left\langle r_{ch}^2 \right\rangle &= \int r^2 \rho_{ch}(\boldsymbol{r}) d\boldsymbol{r} / \int \rho_{ch}(\boldsymbol{r}) d\boldsymbol{r} \\
\left\langle r_{p}^2 \right\rangle &= \int r^2 \rho_{p}(\boldsymbol{r}) d\boldsymbol{r} / \int \rho_{p}(\boldsymbol{r}) d\boldsymbol{r} \\
\left\langle (r_{ch}^{\text{proton}})^2 \right\rangle &= \int r^2 \rho_{ch}^{\text{proton}}(\boldsymbol{r}) d\boldsymbol{r} / \int \rho_{ch}^{\text{proton}}(\boldsymbol{r}) d\boldsymbol{r} \\
\left\langle (r_{ch}^{\text{neutron}})^2 \right\rangle &= \int r^2 \rho_{ch}^{\text{neutron}}(\boldsymbol{r}) d\boldsymbol{r} / \int \rho_{ch}^{\text{neutron}}(\boldsymbol{r}) d\boldsymbol{r}
\end{aligned}$$

$\langle r_{ch}^2 \rangle, \left\langle r_{p}^2 \right\rangle, \left\langle (r_{ch}^{\text{proton}})^2 \right\rangle$, and $\langle (r_{ch}^{\text{neutron}})^2 \rangle$ are defined as the MS radii of ρ_{ch}, ρ_p, $\rho_{ch}^{\text{proton}}$, and $\rho_{ch}^{\text{neutron}}$, respectively.

The Eq. (4.20) is calculated using a Fourier transform as;

$$F_{ch}(q) = G_{ch}^{p}(q) \cdot F_p(q) + G_{ch}^{n}(q) \cdot F_n(q), \tag{4.22}$$

where, $F_{ch}(q)$, $F_p(q)$, $F_n(q)$, and $G_{ch}^{p}(q)$, $G_{ch}^{n}(q)$ indicate Fourier transforms of charge, point proton, point neutron, and the charge distribution of proton, neutron themselves, respectively. $G_{ch}^{p}(q)$, $G_{ch}^{n}(q)$ are also called Sachs electric form factor of proton and neutron [65]. Since digital data of form factors are not existed, we estimate pseudo data and their errors to solve the Eq. (4.22). The center value of the pseudo data are estimated to Fourier-transform existing charge distribution. The errors are estimated from the existing form factor of ^{124}Sn via an eye guide in Fig. 4.11 [66]. The SOG density for a point proton ρ_p is adopted, and the point proton density is also analytically Fourier-transformed to the proton form factor $F_p(q)$. And the simple parameterization of nucleon form factors $G_{ch}^{p}(q)$, $G_{ch}^{n}(q)$ are used in this analysis as follows [67];

$$G_{ch}^{p}(q) = \frac{1 - 0.24\tau}{1 + 10.98\tau + 12.82\tau^2 + 21.97\tau^3} \tag{4.23}$$

$$G_{ch}^{n}(q) = \frac{1.70\tau}{1 + 3.30\tau} \frac{1}{(1 + 4.97\tau)^2} \tag{4.24}$$

where

$$\tau = q^2 / 4M_{\text{nucleon}}^2.$$

The RMS radius of proton itself is 0.863 ± 0.004 fm [67], and the MS radius of neutron itself is -0.112 ± 0.003 fm^2 [67]. This proton radius is consistent with the measurement of the hydrogen 1S Lamb shift [68]. Equation (4.20) shows that an explicit treatment for charge distribution of neutron itself is necessity to deduce point proton density distribution precisely. In case of tin isotope, the contribution from the $G_{ch}^{n}(q)$ to the RMS radius of the point proton density distribution is in the order of 0.02 fm. Thus, the contribution from the neutron form factor is small but not negligible if we want to discuss the difference of 0.02 fm in RMS radii. These nucleon form factors $G_{ch}^{p}(q)$, $G_{ch}^{n}(q)$ are in good agreement with existing data of proton and neutron form factors in Fig. 4.7, 4.8. And these parameterizations can also explain the recent polarization transfer measurement at MIT-Bates [69].

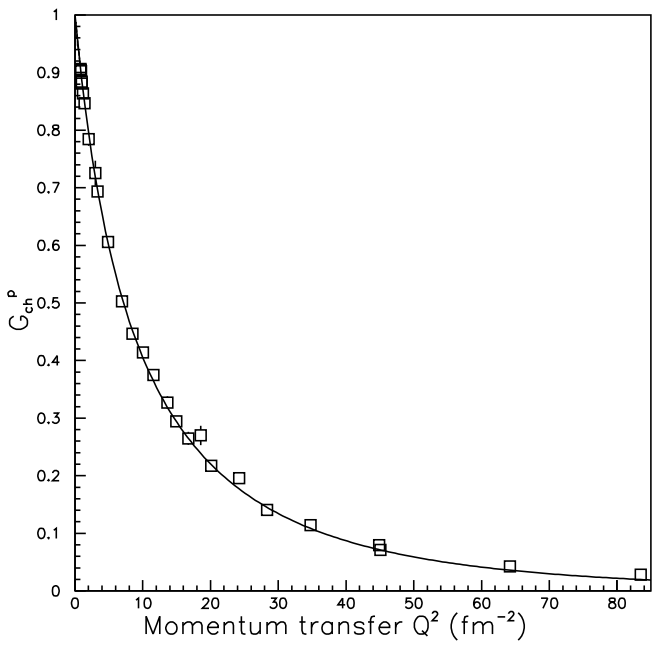

Figure 4.7: The proton electric form factor shown as Eq. (4.23) and existing experimental data are taken from electron-proton scattering [16].

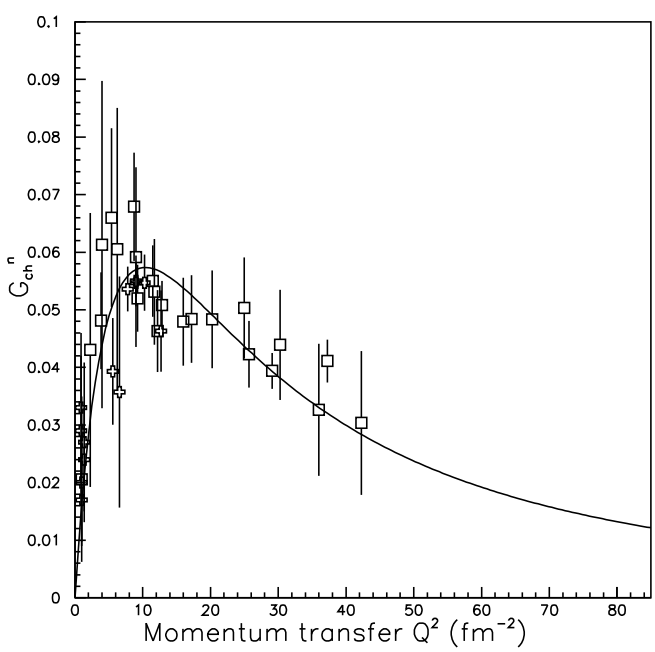

Figure 4.8: The neutron electric form factor shown as Eq. (4.24) and existing experimental data from electron-deuteron or helium-3,4 scattering and sophisticated analysis [17]. On the other hand, the MS charge radius of the neutron had been determined from other literature experiments [14].

The point proton distributions are unfolded using Eq. (4.22) by the following procedure;

1, We have constructed pseudo data and errors of charge form factor $F_{ch}(q)$ on momentum space using charge distribution ρ_{ch}.

2, We have assumed a initial proton, neutron density distribution, for example $\rho_p^{\rm init}(r) = \rho_{ch}(r)$, $\rho_n^{\rm init}(r) = (N/Z)\rho_p(r)$.

3, We have calculated the right-hand side of the Eq. (4.22) using initial nucleon densities $\rho_p^{\rm init}$, $\rho_n^{\rm init}$ and the nucleon electric form factors $G_{ch}^p(q)$, $G_{ch}^n(q)$ from the Eq. (4.23) and Eq. (4.24).

4, We have searched point proton density distribution comparing the right-hand side of the Eq. (4.22) with the pseudo data.

Figure 4.10 shows the result of the fitting in the case of ^{124}Sn. The solid line shows calculation from the Eq. (4.20). Open circles and bars are pseudo data and errors constructed for the least-square fitting. The SOG parameters of the point proton density distribution are freely searched using the MINUIT code [70].

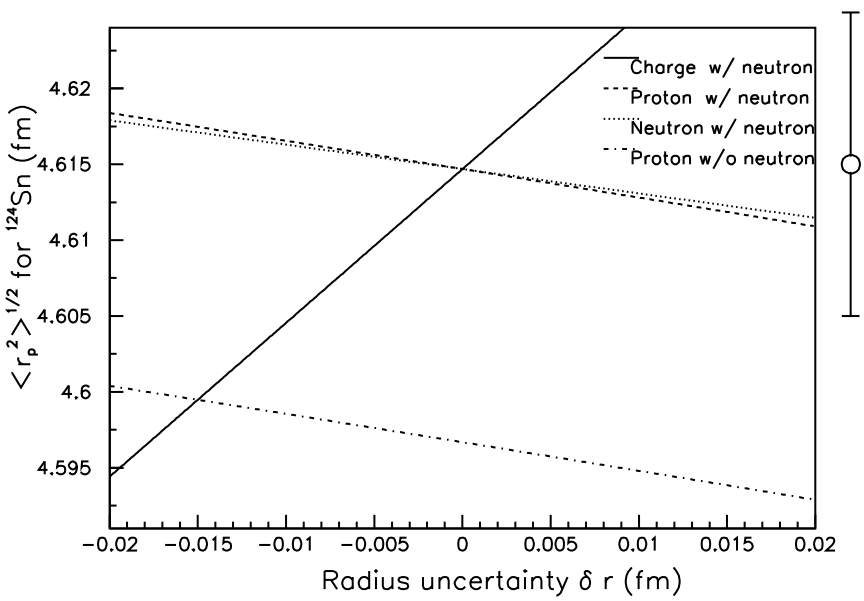

Figure 4.9: Contribution to the RMS radius of point proton density distributions for ^{124}Sn. Solid, dashed, and dotted lines show results of charge, proton, and neutron RMS radius using the propagation of errors for the point proton RMS radius with neutron electric form factor. Dash-dotted line shows the case of proton RMS radius the without neutron electric form factor. Open circle and bars show targeted value for uncertainty of point proton RMS radius, ±0.01 fm.

Figure 4.9 shows the contribution from uncertainties of charge, proton itself, and neutron itself RMS radii to point proton RMS radius. The effect including the neutron electric form factor is obvious when the accuracy to be 0.01 fm is needed. Since the errors of point proton RMS radii are mainly determined by errors of charge RMS radii in Eq. (4.21), the errors of point proton RMS radii of tin isotopes are estimated to be 0.003 fm whose value is the same order to charge RMS radius.

Figure 4.12 shows a comparison of our deduced proton density for ^{124}Sn using the scaled neutron density as an initial one with several theoretical calculations using L-HS, SkM*, and SIII, respectively. Our deduced density has less oscillatory behavior than three theoretical calculations. Among the calculations, SHF model using SkM* is in good agreement with our deduced densities for five tin isotopes. Figure 4.13 shows our deduced proton density distributions. The systematic behavior as shown in Fig. 4.5 has been conserved in the process of unfolding charge distribution.

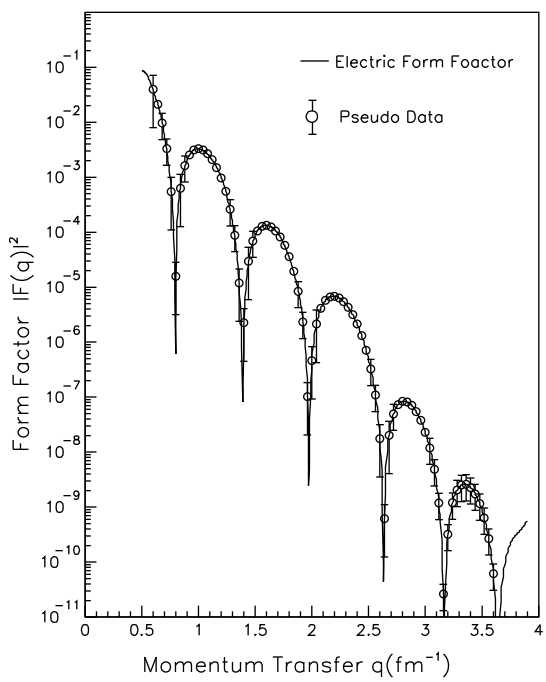

Figure 4.10: Calculated by the right-hand side of Eq. (4.20) and pseudo data using SOG charge distributions of ^{124}Sn.

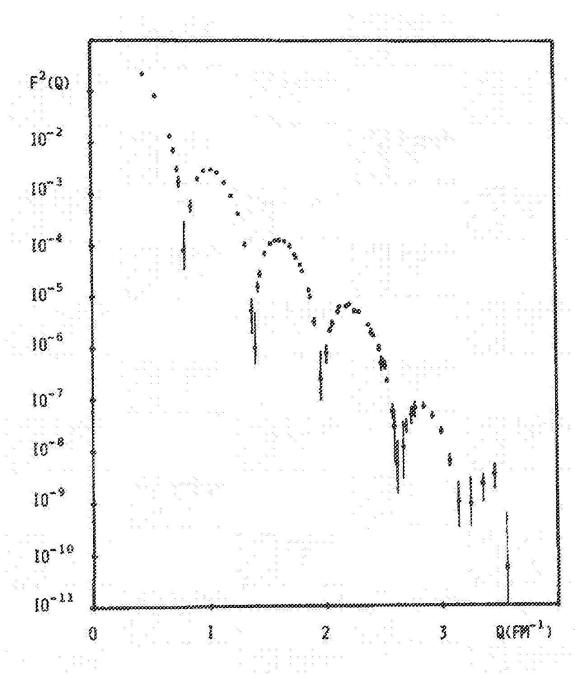

Figure 4.11: Experimental form factors and errors of ^{124}Sn from electron scattering experiments [66].

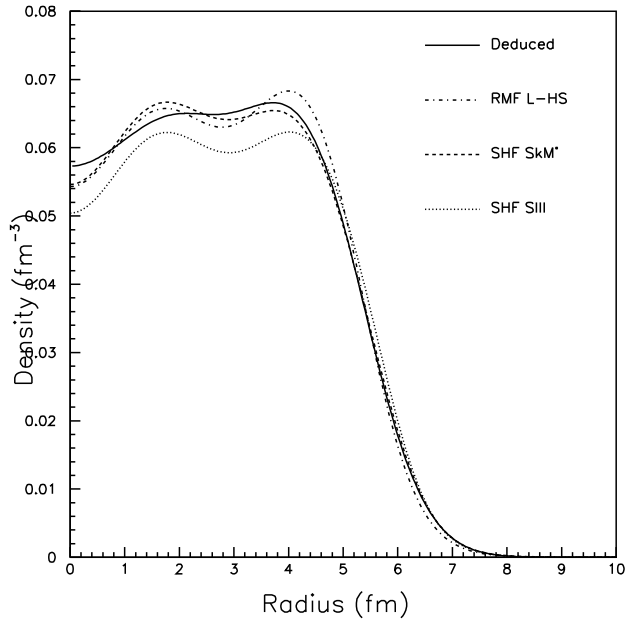

Figure 4.12: Point proton density distribution of ^{124}Sn. Solid, dashed, dotted, and dashed-dotted lines show the point proton density distributions deduced from Eq. (4.30) and based on RMF with L-HS parameterization, SHF with SkM* [71], and SIII [72] parameterization, respectively. Here, we used the scaled neutron density $\rho_n(r) = (N/Z)\rho_p(r)$ for the initial density of Eq. (4.20).

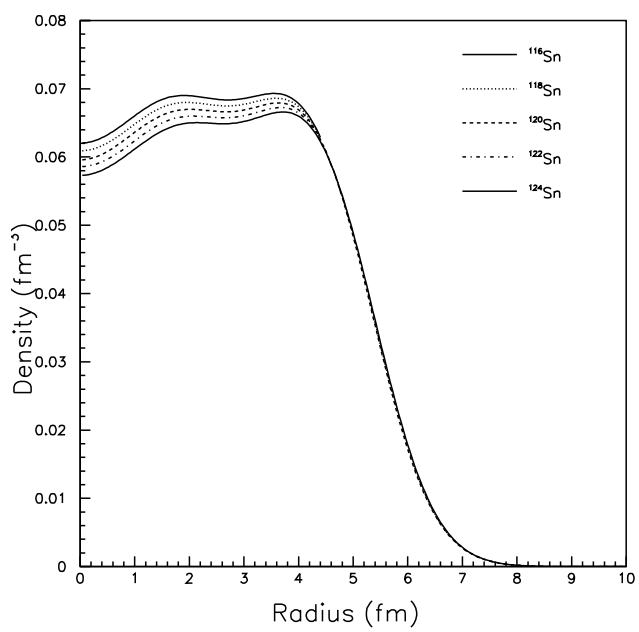

Figure 4.13: The deduced initial point proton density distributions of ^{116,118,120,122,124}Sn using SOG charge distribution. Here, we used the scaled neutron density $\rho_n(r) = (N/Z)\rho_p(r)$ as the initial density of Eq. (4.20).

4.5 Relation between scalar and vector density

In the RIA calculation, two types nucleon density distributions, namely the scalar density ρ^S and the vector density ρ^V are needed. In our calculation the tensor density ρ^T is neglected because of its smallness. Here $\rho^V(r)$ indicates the vector density corresponding to the normal type proton or neutron density. Each density satisfies the normalization condition;

$$\int \rho_p^V(r)dr = Z, \qquad \int \rho_n^V(r)dr = N. \tag{4.25}$$

It is difficult to determine experimentally the fine structure of scalar densities. However, the following clear relation between scalar and vector densities have been discovered empirically [36].

$$\rho^S(r)/\rho^V(r) \simeq \text{const.} \tag{4.26}$$

Thus scalar densities can be calculated using the relation between vector and scalar densities estimated by the relativistic Hartree calculation code TIMORA which are introduced by Horowitz and Serot [56]. Their parameterization (L-HS) does not include a non-linear term of σ and ω fields in their Lagrangian. The non-linear terms are described as;

$$\frac{1}{2}m_\sigma^2\sigma^2 + \frac{1}{3}g_2\sigma^3 + \frac{1}{4}g_3\sigma^4 - \frac{1}{4}g_4(\omega_\mu\omega^\mu)^2. \tag{4.27}$$

The necessity of those terms to improve the fit for binding energy is already known, but their contributions to the scalar density is not clear. Thus L-HS calculation is compared with TMA calculation in ^{208}Pb, which include the non-linear term introduced by Toki and Sugahara [73, 74].

Figure 4.14 and 4.15 show ratios of scalar to vector densities in radial distributions of ^{208}Pb for TMA and L-HS, respectively. Both calculations show almost the same ratio in their radial distributions. We deserve no difference for the ratio scalar to vector densities between L-HS and TMA, and we expect similar relation holds for other RMF calculation.

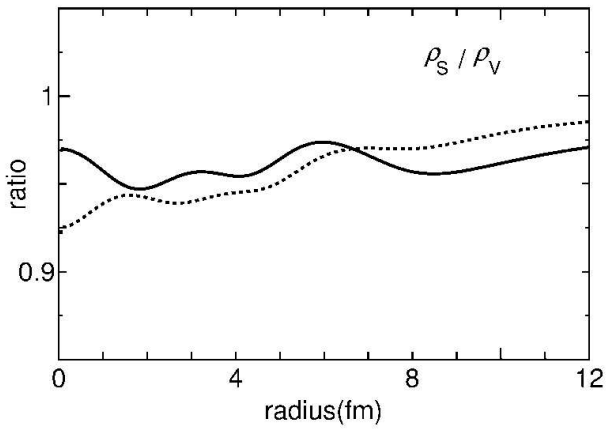

Figure 4.14: The radial distribution of the ratio of scalar to vector densities of ^{208}Pb using the TMA parameterization calculated by Kaki [74]. Solid and Dashed lines show proton and neutron, respectively.

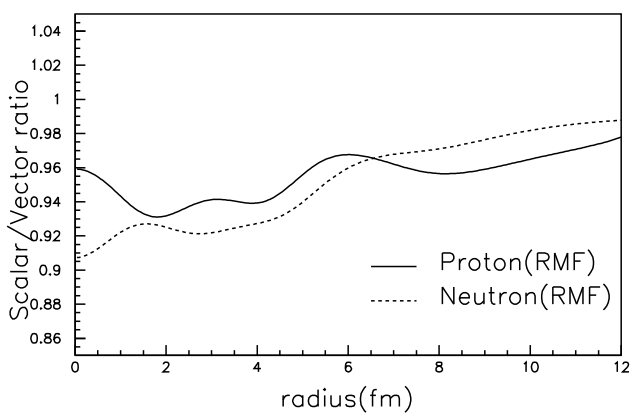

Figure 4.15: The radial distribution of the ratio of scalar to vector densities of ^{208}Pb using the L-HS parameterization which is not included the non-linear term as shown in Eq. (4.27).

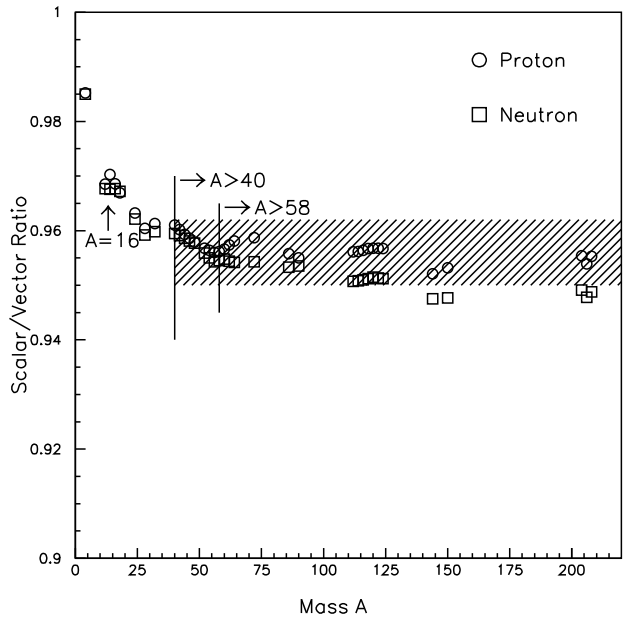

Figure 4.16: Integrated ratio from scalar and vector densities of proton and neutron of typical stable nuclei calculated of L-HS. Hatched area shows 0.955±0.005.

Figure 4.16 shows a mass dependence of the ratios of integrated scalar and vector densities using L-HS one. In this region, we can see a small dependence on mass number, but it is less than 1%. A slight difference is noticed in the ratios of scalar to vector densities of proton and neutron in the heavy-nuclei case. It is because that the scalar density is related to the average density. In the medium and heavy nuclei, number of neutron is different from protons due to the Coulomb repulsion. And a difference of a uniform density in a nuclear medium between proton and neutron becomes larger with mass number. However its difference is relatively small (less than 1%), and hardly affects experimental observables.

Table 4.2: The exiting theoretical and experimental proton, neutron RMS radius, and its differences of ^{58}Ni.

Method	$\left\langle r_p^2 \right\rangle^{1/2}$ (fm)	$\left\langle r_n^2 \right\rangle^{1/2}$ (fm)	Δr_{np} (fm)
DME+D1[75]	3.68	3.67	-0.01
HF-BCS+SIII[76]	3.738	3.732	-0.006
HF-BCS+SkM*[77]	3.722	3.720	-0.002
HF-BCS+SGII[78]	3.719	3.697	-0.012
RMF+NL3[79]	3.652	3.692	0.040
RMF+L-HS[56]	3.652	3.691	0.039
Glauber, 3pF[27]^{*1}	3.763(50)	3.72(5)	-0.043(70)
Glauber, 3pF[28]^{*2}	3.67(5)	3.60(5)	-0.07(7)
Glauber, 3pF[80]^{*1}	3.763(50)	3.75(10)	-0.01(7)
1st-order KMT, 3pF+SOG[31] ^{*3}	3.688	3.652(74)	-0.035(74)
2nd-order KMT, 3pF+SOG[32]^{*3}	3.686	3.700(50)	-0.035(50)
$\bar{p}$-Nucleus potential, 2pF[18]^{*4}	–	–	$-0.09^{+0.09}_{-0.16}$
This work, SOG	3.672(3)	3.672^{*5}	0.000^{*5}

^{*1} 1.044 GeV(p,p) at Gatchina
^{*2} 1.047 GeV(p,p) at Scalay
^{*3} 800 MeV(p,p) at LAMPF
^{*4} Anti-protonic atom X-ray at LEAR
^{*5} assumption in this work.

4.6 ^{58}Ni structure

The information on both proton and neutron density distributions is needed to calibrate the effective interaction based on RIA calculations. Several theoretical calculations have been performed to obtain the proton and neutron density distributions of ^{58}Ni using relativistic or nonrelativistic mean-field calculations. The results are dependent on parameterizations used in the calculations but the differences between the RMS radii of point protons and neutrons, the neutron skin, are generally small [75, 76, 78, 79, 81, 82], and are given as

$$\Delta r_{np} \equiv \left\langle r_n^2 \right\rangle^{1/2} - \left\langle r_p^2 \right\rangle^{1/2}. \tag{4.28}$$

In addition, since the number of neutron for ^{58}Ni is almost the same as number of proton, the shape of neutron density distribution is expected to be similar to the shape of proton. Thus the neutron density distribution is assumed to be the same shape as the proton density distribution. And the neutron density distribution can be described as;

$$\rho_n(r) \equiv (N/Z)\rho_p(r). \tag{4.29}$$

Thus, the substitution of Eq. (4.29) into Eq. (4.20) gives as;

$$\rho_{ch}(\boldsymbol{r}) = \int \rho_p(\boldsymbol{r'})[\rho_{ch}^{\text{proton}}(\boldsymbol{r}-\boldsymbol{r'}) + (N/Z)\rho_{ch}^{\text{neutron}}(\boldsymbol{r}-\boldsymbol{r'})]d\boldsymbol{r'}. \tag{4.30}$$

Table 4.3: The summary of exiting charge distributions data using model and model-independent functional shapes of ^{58}Ni.

Nuclei	Model	RMS radius (fm)	q-range (fm^{-1})	Year
^{58}Ni	2pF	3.823(15)	0.68-1.61	1970 [3]
	2pF	3.783(30)	1.02-1.98	1972 [3]
	3pG	3.760(10)	0.51-2.22	1973 [3]
	3pF	3.764(10)	0.58-2.64	1974 [3, 7]^{*1}
	FB	3.742(24)	0.51-2.22	1976 [7]
	SOG	3.772(4)	0.58-3.80	1980 [7]^{*1}
	FB	3.769(13)	0.25-2.65	1983 [7]

^{*1}Including the result from muonic atom data [83].

The point proton density distribution $\rho_p(r)$ of ^{58}Ni is calculated by unfolding the above equation. The SOG parameterization is used for the charge distribution of ^{58}Ni, which covers a higher momentum transfer region up to 3.80 fm^{-1} which is considered for the muonic atom result [83]. A lower region (<0.6 fm^{-1}) where a Fourier-Bessel (FB) parameterization covers is not included, however its low-momentum transfer region does not affect charge distribution in Fig. 4.2.

Figure 4.17 shows the comparison between the deduced point proton density distribution and the calculation based on the Skyrme Hartree Fock (SHF) using SIII and SkM* parameterizations and the RMF using L-HS parameterization. The RMF density shows an oscillatory behavior and a stiff surface, however the RMS radius of proton density is only slightly smaller than our deduced result. The oscillatory behaviors using SHF models are also shown. Their oscillating amplitudes of SHF models are smaller than the calculations by the RMF, and in good agreement with our deduced densities. And the RMS radii of point proton density in SHF models are larger than the deduced density by the order of 0.05 fm, but surface behaviors of SHF models reproduce our deduced density.

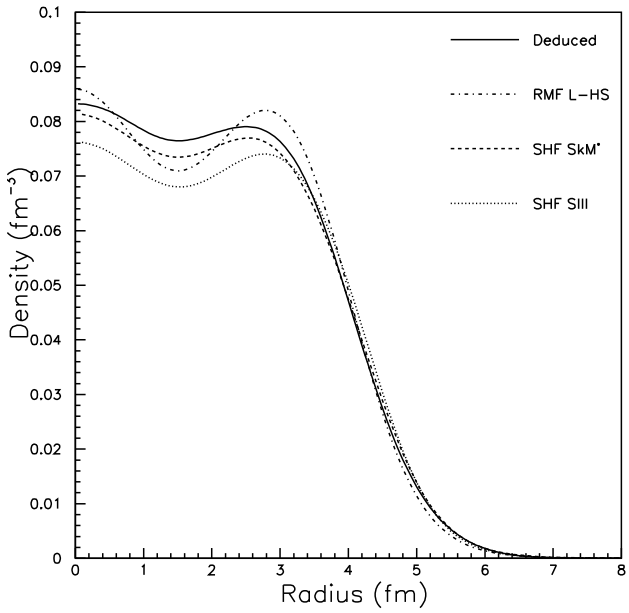

Figure 4.17: Point proton density distribution of ^{58}Ni. Solid, dashed, dotted, and dashed-dotted lines show point proton density distribution deduced from Eq. (4.30)and based on RMF with L-HS parameterization, SHF with SkM* [71] and SIII [72] parameterization, respectively.

We adopt the the constant value R_{SV}=0.96 which is the same as in the tin isotope cases. Using this constant value, a scaled scalar density is simply expressed as;

$$\rho^S(r) = R_{SV} \cdot \rho^V(r). \tag{4.31}$$

In Fig. 4.19, we compare calculated results for ^{58}Ni using a microscopic scalar density and the scaled densities with constant values. For the vector density, we used the RMF densities using the L-HS. We calculate several type scalar density with fixing the vector densities. Solid and dashed lines show the results using the scaled scalar densities and the RMF scalar ones. The calculation using a constant value of 0.96 is in good agreement with the one using microscopic densities. And even if a different constant value from 0.95 to 0.97 was taken, the differences in the cross sections and the analyzing powers would be small ($<$ 2-3%) without momentum transfer dependence. Therefore, the scaled scalar density is used in the following calculation in this work.

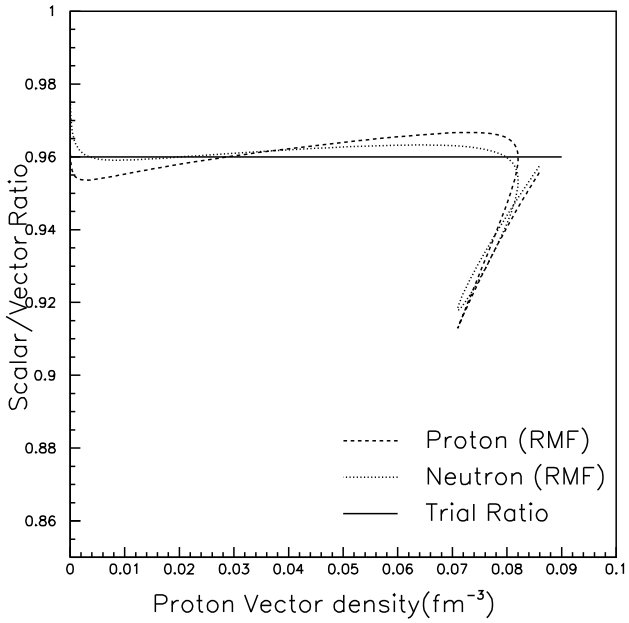

Figure 4.18: Ratio from vector density and scalar density of proton and neutron of ^{58}Ni calculated by the RMF calculation code using L-HS.

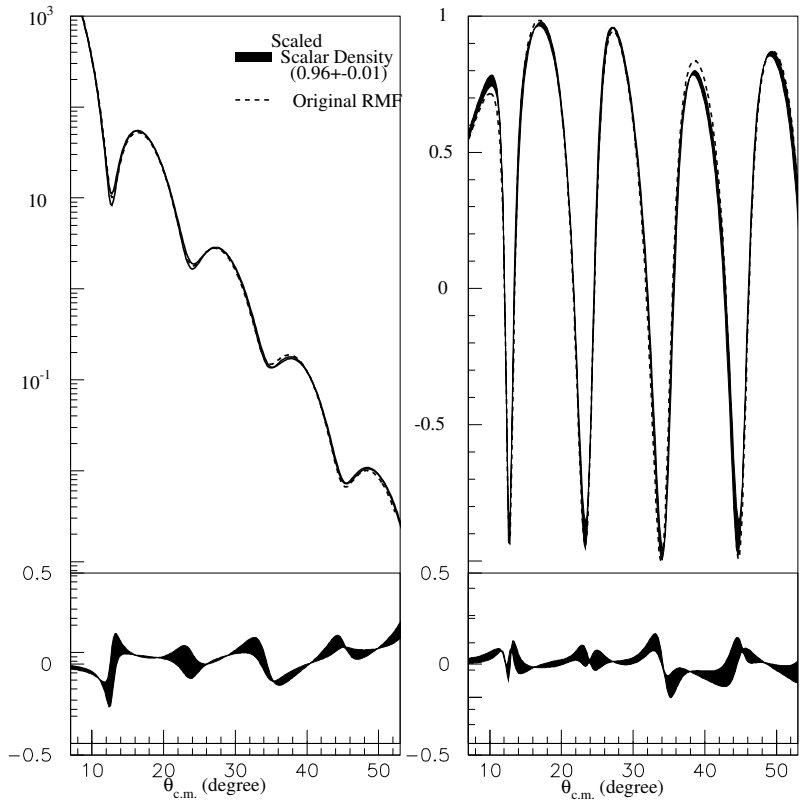

Figure 4.19: RIA calculations with different scalar density distributions of ^{58}Ni. Hatched area are deduced scalar density distributions. Dashed lines are original RIA calculations.

4.7 Effective interaction

In this section, we discuss the effective interaction to explain proton scattering data by the RIA calculation. The RLF effective interaction is tuned using medium modification parameters via proton-^{58}Ni elastic scattering at 295 MeV, since the RMS radius of neutron density distribution for ^{58}Ni is reasonably assumed to be the same as that of proton. Sakaguchi *et al.* introduced eight parameters, which consist of coefficients for coupling constants and masses of σ and ω in Eq. (4.11) to explain the scattering. Since in the case of the eight parameters have too many degrees of freedom for the fit, we have attempted to obtain a good fit by using four parameters. By reduction the number of free parameters, we can reduce the ambiguities of neutron density distributions of the tin isotopes caused by the ambiguities of the effective interaction. In this work the same modification parameters are used for both real and imaginary parts of the scattering amplitude ($\bar{a}_j = a_j$, $\bar{\mathrm{b}}_j$=b_j) to reduce the number of free parameters. Thus four free parameters are searched.

These parameters were determined by fitting the experimental data so as to minimize the chi-square (χ^2) value. χ^2 is defined as

$$\chi^2 \equiv \sum [(x_{\mathrm{exp.}} - x_{\mathrm{theo.}})/\Delta x_{\mathrm{exp.}}]^2 \tag{4.32}$$

where $x_{\mathrm{exp.}}$, $\Delta x_{\mathrm{exp.}}$ and $x_{\mathrm{theo.}}$ are the experimental data, the error of the data, and the calculated result, respectively. Figure 4.20 shows the experimental data at 295 MeV and the fitting result with the RIA calculation using the modified effective interaction with the unfolded proton and neutron densities of ^{58}Ni obtained using Eq. (4.29). Our calculations are in good agreement with all the data of the cross sections, the analyzing powers, and the spin rotation parameters for up to 3.5 fm^{-1}. The minimum chi-square χ^2_{min} for ^{58}Ni data using four free parameters ($\chi^2_{min} = 801$) has almost the same order ($\sim$10% increase) as that in the previous work using eight free parameters ($\chi^2_{min} = 692$).

A two-dimension mesh-search is performed to estimate uncertainties of these parameters. Figure 4.21 shows a correlation between a_σ and a_ω. In the case of a_σ, a_ω correlation, the minimum of χ^2 is searched b_σ, b_ω with rest two parameters a_σ, a_ω fixed at the mesh point value. The circle point shows the best-fit parameter, and horizontal and vertical bars show the error bars of a_σ and a_ω, respectively. The correlation is valley like and very strong, and the correlations of the other five combinations of these parameters also show similar behaviors as shown in Fig. 4.22. The minimum points indicated by arrows in Fig. 4.22 is located at the center of each correlation valley. Thus the modification parameters are uniquely determined.

The uncertainties of the modification parameters from the statistics and the experimental conditions are estimated as follows;

$$\chi^2 \leq \chi^2_{min} + P. \tag{4.33}$$

Here, P (in this work P=4) denotes a number of fitting parameters [84]. Table 4.4 shows a summary of the fitting results. The hatched area in Fig. 4.21 shows the region that satis-

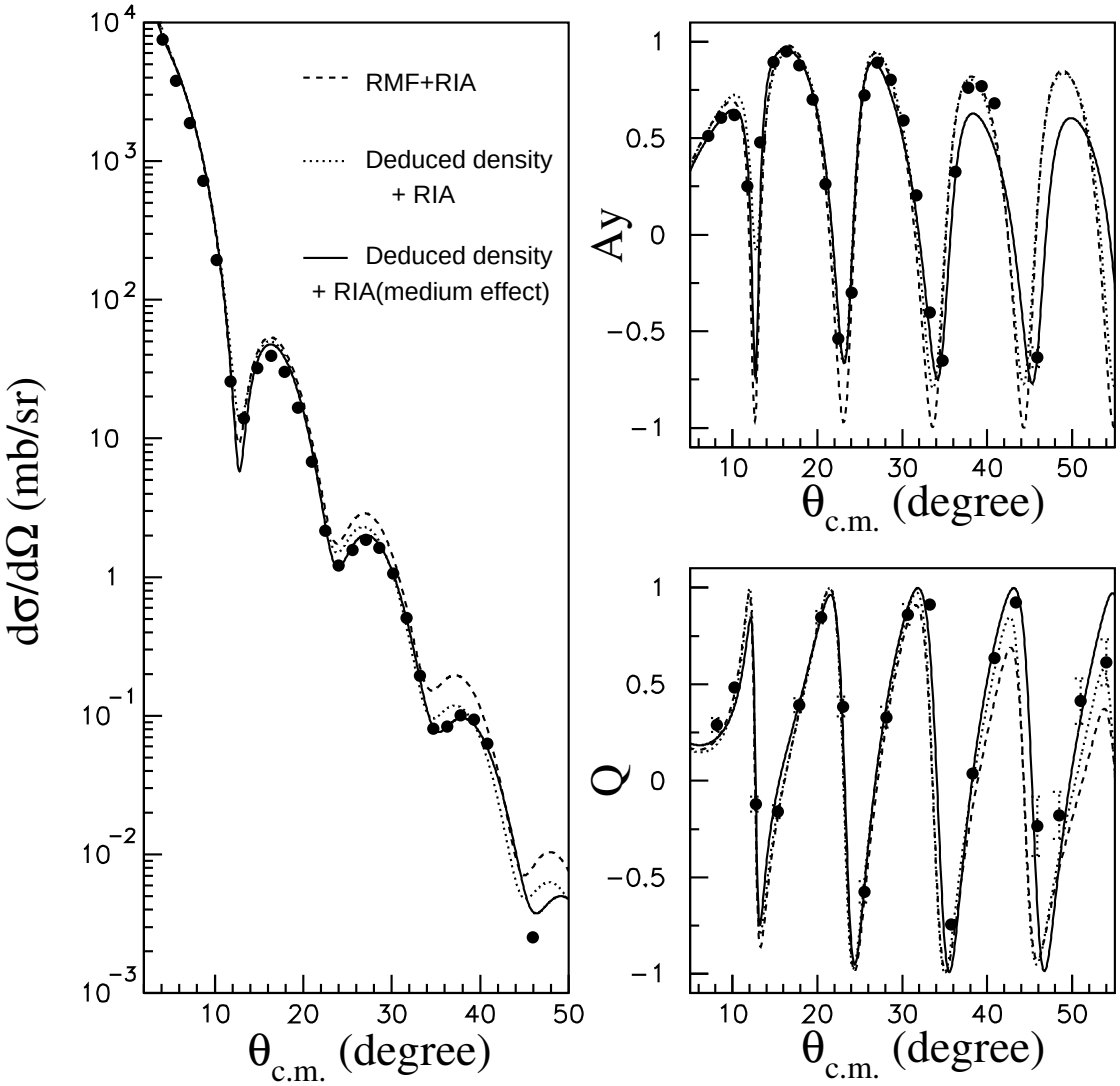

Figure 4.20: Experimental data of ^{58}Ni at 295 MeV. Dashed lines are the result of the original RIA calculations using Relativistic mean field densities. Dotted lines are represent a similar calculation as above but using a density distribution deduced from the electron scattering data. Solid lines are a calculation with the modified effective interaction using deduced densities.

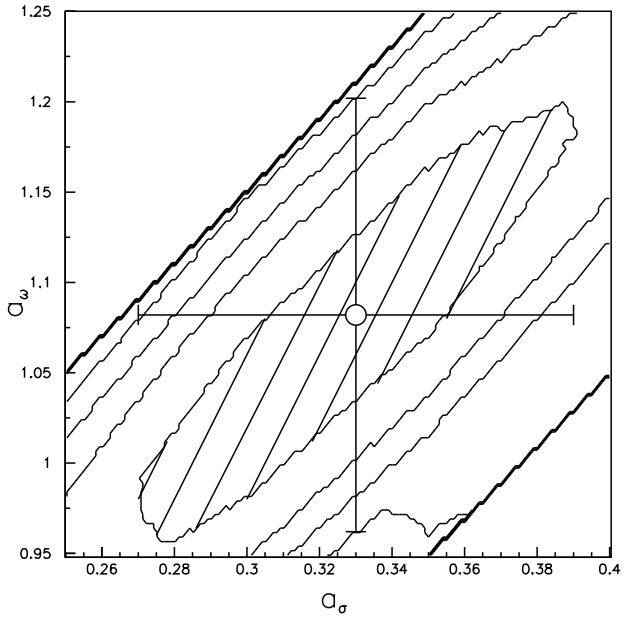

Figure 4.21: Contour plot of χ^2 correlation of a_σ with a_ω for ^{58}Ni. The hatched area represents the region obtained from Eq. (4.33). The open circle and bars represent the best-fit parameter and the errors shown in Table 4.4, respectively. The magnitude of χ^2 is arbitrary.

fies Eq. (4.33). Since each pair of parameters has a strong correlation, we cannot independently use the entire region defined by the errors in Table 4.4, which means that the usable area defined by each pair of the parameter set is very narrow. The correlations between a_j and b_j of each meson at the middle panels in Fig. 4.22 are stronger than other correlations. And the reduction ratio of the coupling constant a_j^* at normal density ρ_0 has almost same one of the mass b_j. They mean that $g_\sigma^*/g_\sigma = 0.87 \pm 0.02$, $m_\sigma^*/m_\sigma, = 0.88 \pm 0.05$, $g_\omega^*/g_\omega = 0.69 \pm 0.02$, $m_\omega^*/m_\omega = 0.70 \pm 0.03$ at normal density. The result implies that density dependences of real and imaginary parts may have a common origin.

Table 4.4: Medium-effect parameters at 295 MeV. The error estimation is discussed in this section

j	σ	ω
a_j	0.33 ± 0.06	1.08 ± 0.12
b_j	-0.12 ± 0.05	-0.30 ± 0.03
a_j^*	-0.13 ± 0.02	-0.31 ± 0.02

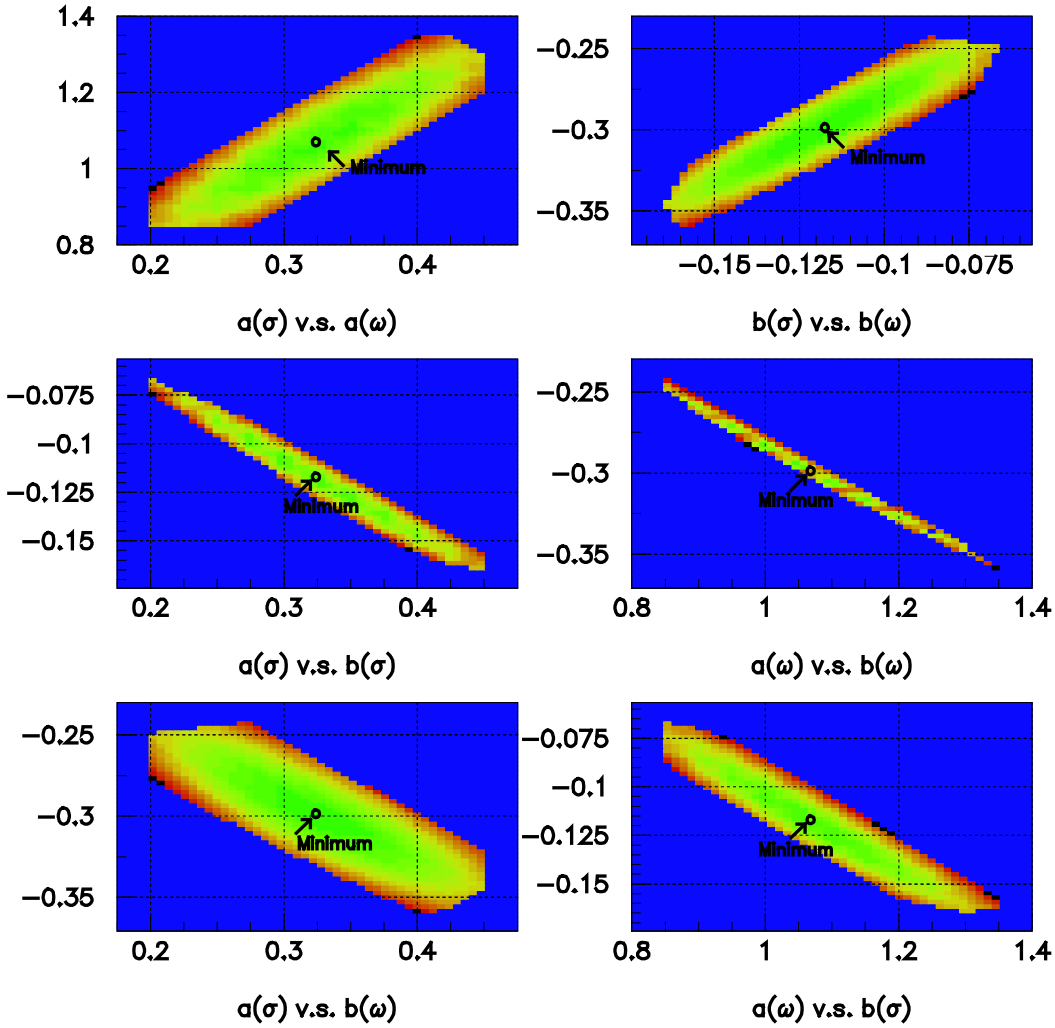

Figure 4.22: Contour plot of χ^2 correlation for all combination of ^{58}Ni. The upper-left figure is the same as Fig. 4.21.

4.8 Coupled channel effect at the intermediate energy

In this section, we discuss whether in the high-momentum-transfer region, the multistep process may affect the angular distribution of elastic scattering or not [60]. If the contributions were dominant to experimental observables, its contributions should be explicitly treated for each nucleus. To estimate the effect of multistep processes, a coupled-channel calculation is performed by using the coupled-channel code ECIS95 written by Raynal [85]. As the coupled state, the first excitation 2^+ is considered. Table 4.5 shows a summary of the transition probabilities B(E2) and deformation parameters β_2 for the first 2^+ discrete level of ^{58}Ni and tin isotopes $^{116-124}$Sn, where β_2 are calculated using existing B(E2) values as follows [86] ;

$$\beta_2 = \frac{4\pi}{3ZR_0^2}\sqrt{\mathrm{B(E2)}/e^2}, \qquad R_0 = 1.20\ A^{1/3}\ \mathrm{fm}. \tag{4.34}$$

Table 4.5: Summary of the transition probabilities B(E2) and deformation parameters β_2 of the first 2^+ discrete level.

Nuclei	E(2^+) (MeV)	B(E2) (e^2b^2) [86]	β_2
^{58}Ni	1.454	0.0695(20)	0.180
^{116}Sn	1.293	0.209(12)	0.1118
^{118}Sn	1.229	0.209(12)	0.1106
^{120}Sn	1.171	0.2020(40)	0.1075
^{122}Sn	1.140	0.1920(40)	0.1036
^{124}Sn	1.131	0.1660(40)	0.0953

Figure 4.23 shows the calculated cross sections and analyzing powers for ^{58}Ni with and without the coupled-channel. As for the optical potential for the calculation, the Dirac based global potential [53, 54] is used. The contribution from the coupled-channel for ^{58}Ni in the momentum transfer range from 0.7 fm^{-1} to 3.5 fm^{-1} is relatively small (1-2%) as shown in Fig. 4.23, whose values are less than the experimental errors.

In the case of the tin isotopes, the situation is similar to the case of ^{58}Ni. Figure 4.24 shows the same calculation as Fig. 4.23, but for the ^{116,118,120,122,124}Sn. The coupled-channel hardly affects the cross sections and the analyzing powers. A slight difference appears at the high momentum transfer region ($>$ 3 fm^{-1}). The differences are very small as in the case of ^{58}Ni. In addition the coupled-channel effect might be partly included in our medium modification parameterization because the effect includes on momentum dependence, and its dependence is involved by the phenomenological search to explain the experimental data. Therefore the effect of the coupled-channel at this energy is negligible at these momentum transfer regions, and was not included explicitly in our analysis.

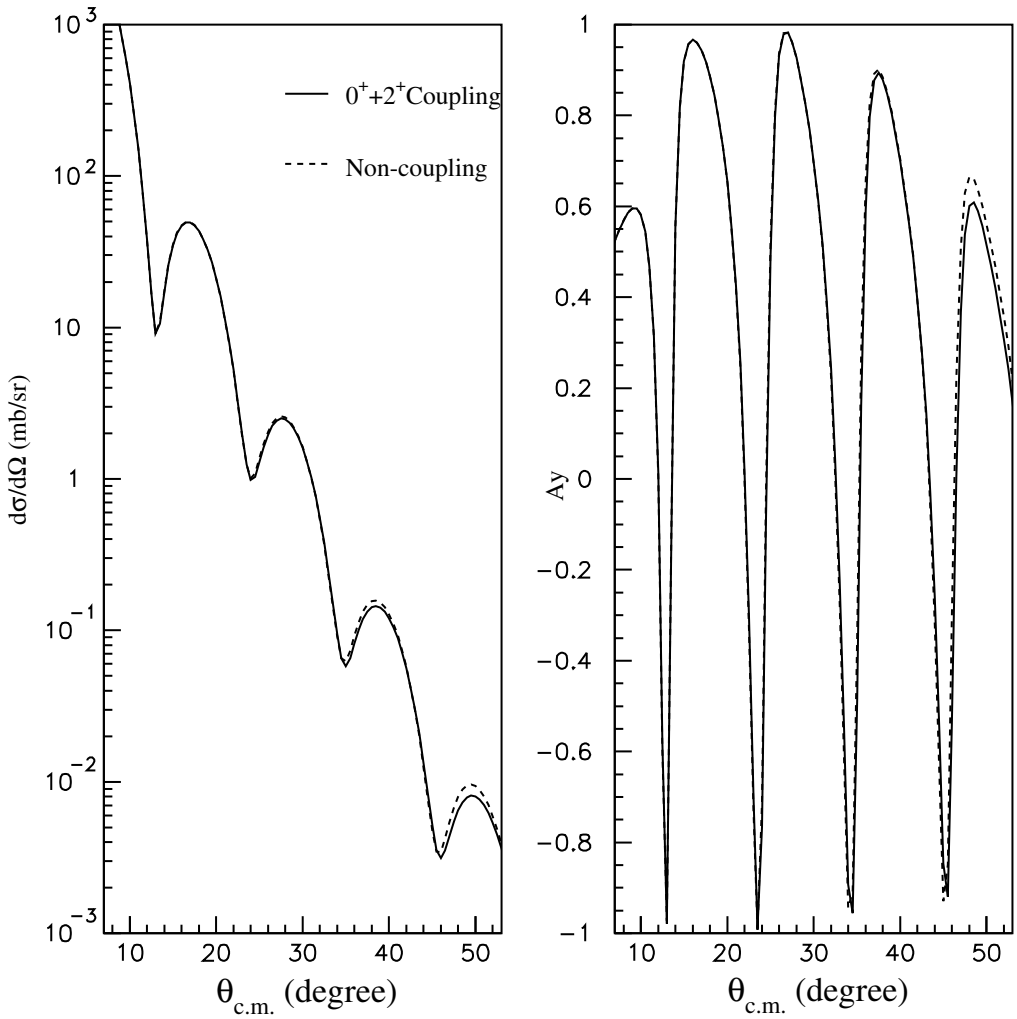

Figure 4.23: Coupling effect of ^{58}Ni at 295MeV. Solid line show coupled channel calculation between ground state and first 2^+ state. Dashed Line is not included of coupled channel. Lower panels show that ratios of cross sections and analyzing powers with to without performing the coupled-channel calculation.

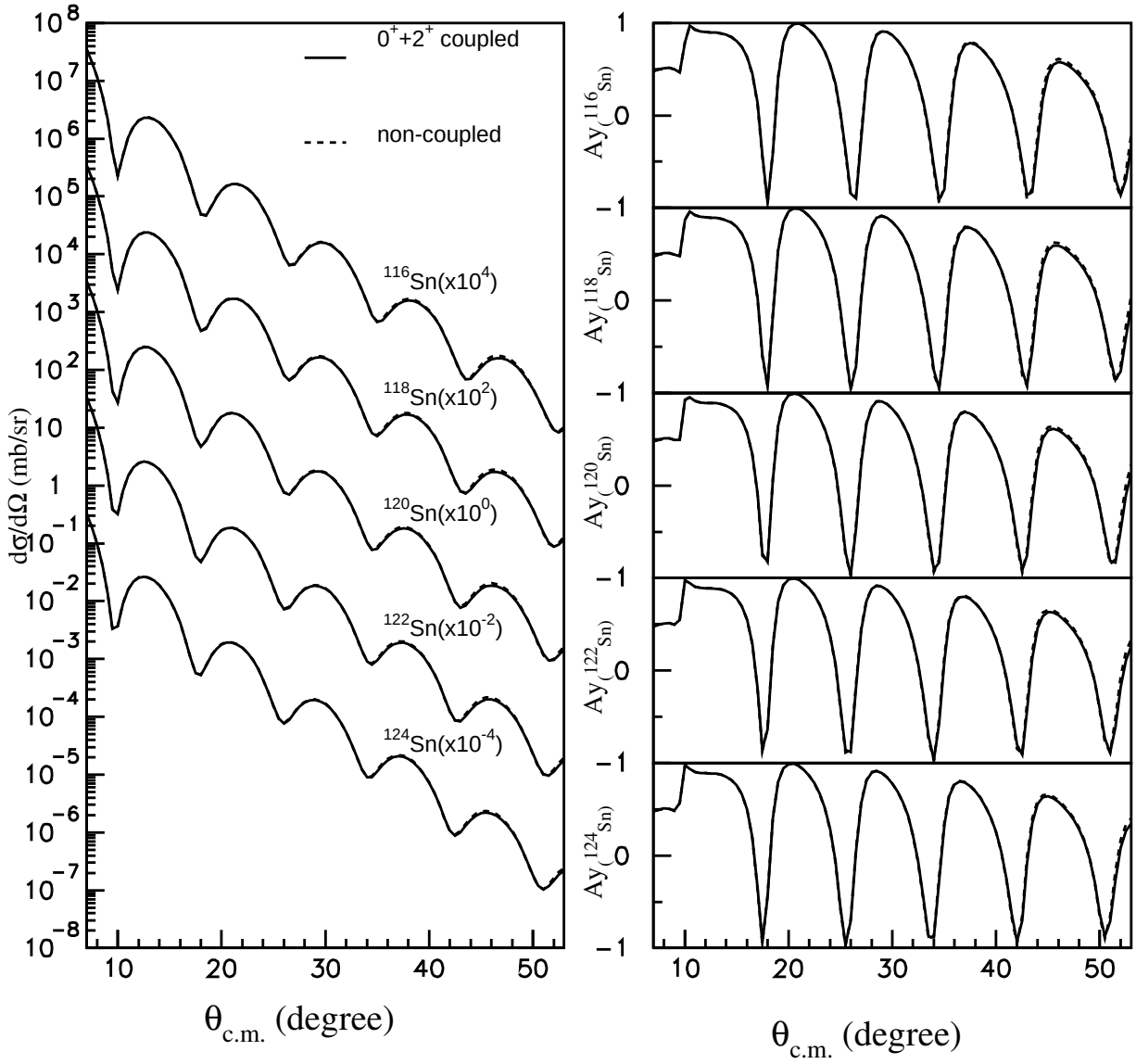

Figure 4.24: Same as Fig4.23, but for the of ^{116,118,120,122,124}Sn at 295MeV.

4.9 Neutron density distributions of tin isotopes

In this section, we attempt to deduce neutron density distributions of tin isotopes by using the modified effective interaction. Scalar nucleon density distributions ρ^S of tin isotopes are estimated to be the vector nucleon density distributions ρ^V multiplied by 0.96 as in the case of ^{58}Ni, because the ratio of scalar to vector densities of heavier nuclei has a similar behavior in medium and heavy nuclei as shown in Fig. 4.16. Figure 4.25, 4.26 show radial dependences of the scalar to vector density ratios for ^{116,124}Sn calculated by the relativistic Hartree code TIMORA. These RMF results are approximated by the constant value of 0.96. The point proton density distributions of tin isotopes are estimated from Eq. (4.20) with an initial neutron density distributions $\rho_n = (N/Z)\rho_p$ of Eq. (4.17) in the same way as ^{58}Ni.

The initial neutron density distribution was then calculated from the equation

$$\rho_n(r) \equiv \rho_p(r) + (\rho_n^{RMF}(r) - \rho_p^{RMF}(r)) \tag{4.35}$$

where $\rho_{n\ [p]}^{RMF}(r)$ denotes the RMF neutron [proton] density distributions using L-HS parameterization [56]. The SOG type density distribution is used as the fitting function of the point neutron density using Eq. (4.15);

$$\begin{aligned} \rho_n(r) &= \frac{N}{2\pi^{3/2}\gamma^3}\sum_{i=1}^{12}\frac{N_i}{1+2R_i^2/\gamma^2} \\ &\quad \times\left[e^{-(r-R_i)^2/\gamma^2}+e^{-(r+R_i)^2/\gamma^2}\right]. \end{aligned} \tag{4.36}$$

However the normalization condition of Eq. (4.16) is rewritten as;

$$\int \rho_n(r)d\boldsymbol{r} = N, \quad \Rightarrow \quad \int N_i = 1. \tag{4.37}$$

Here, the parameters such as γ and R_i are fixed with the results of the charge distribution [7]. Figure 4.27 shows experimental data together with the results of the search and calculations using initial neutron density distributions.

The corresponding parameters N_i of the neutron density distributions are freely adjusted to reproduce our experimental data with a range of momentum transfer from 0.7 fm^{-1} to 3.5 fm^{-1} using the Monte-Carlo technique. Proton and neutron density distributions are iterated until self-consistency is achieved with Eq. (4.20). In the iteration, we have achieved less than 0.1% accuracy for the envelops of neutron density distribution. This process has been repeated two or three times. The process for the iteration hardly affects point proton densities, because charge distributions are mainly sensitive to point proton density distributions. Finally, the point proton and neutron density distributions which satisfy both the proton scattering and the electron scattering which corresponds to Eq. (4.20) are deduced.

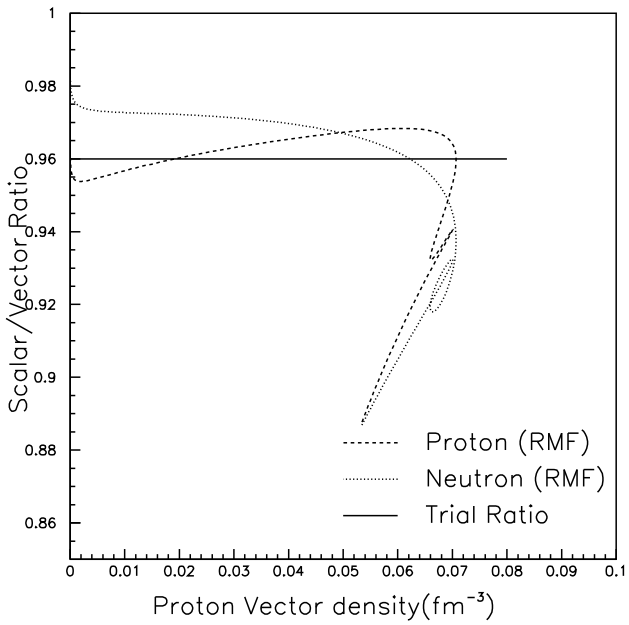

Figure 4.25: The ratio scalar to vector densities of ^{116}Sn. The dashed and dotted lines show proton and neutron, respectively. Solid line shows our assumed value 0.96 as the trial ratio.

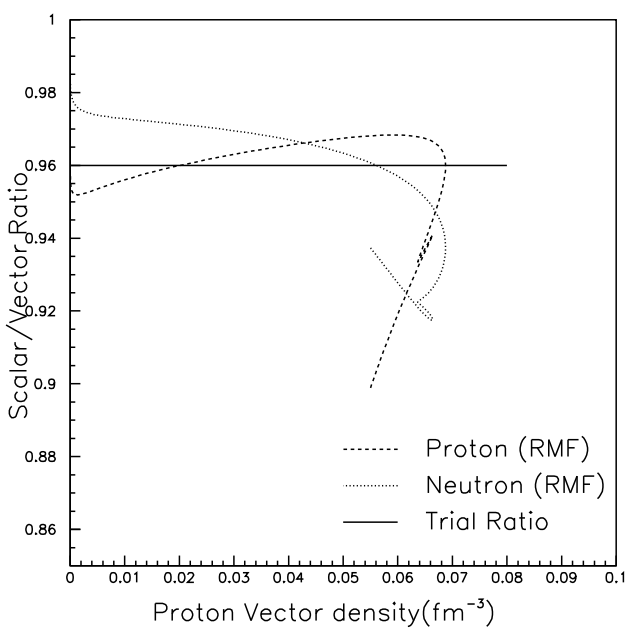

Figure 4.26: The same as in Fig. 4.25, but for ^{124}Sn.

As for the medium modification parameters, the same parameters which were defined in the previous section by the proton-^{58}Ni data were used . The very forward angle data ($\theta_{\mathrm{c.m.}} < 8°$) are not included in the fitting minimization procedure due to experimental difficulties for determining absolute cross section values. Figure shows our experimental data and for tin isotopes and two calculations using the same effective interaction and two different neutron density distributions. The dashed lines are calculations with the modified effective interaction using trial density distributions. The solid lines are best-fit calculations with the modified effective interaction.

The calculations using the initial neutron density and the medium modified effective interaction almost reproduce absolute values of cross sections and amplitude of polarization observables. But both cross sections and analyzing powers are shifted inward in angle because the RMF neutron density distribution has a tendency to have a larger neutron radius. While, we have able to deduce neutron density distributions for all the five tin isotopes up to high momentum transfer 3.5 fm^{-1} corresponding to $\theta_{c.m.} \sim 50°$. These results indicate that our deduced RMS radii of neutron density distribution are smaller than the RMS radii of trial density distributions.

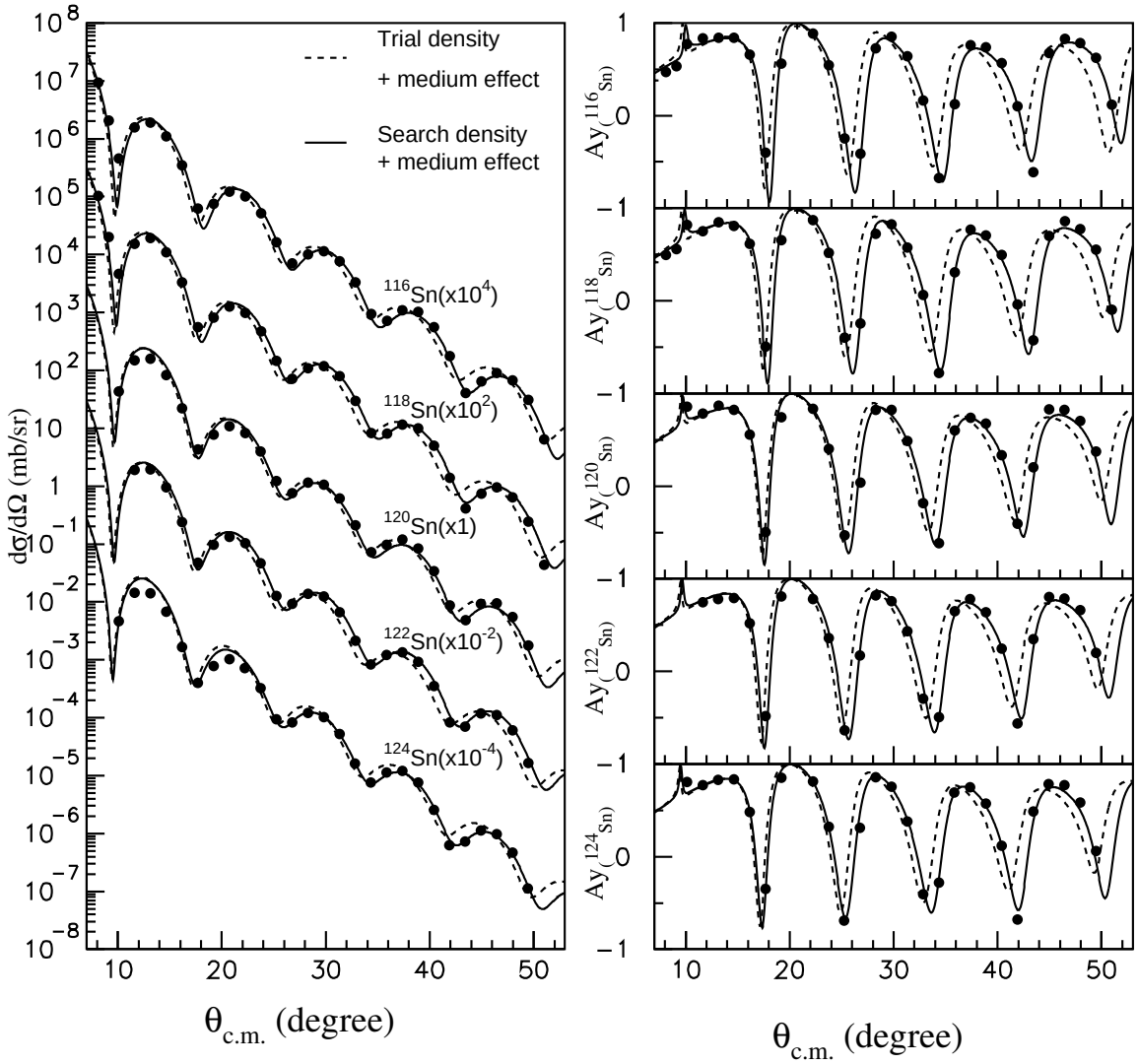

Figure 4.27: Differential cross sections and analyzing powers for proton elastic scattering from tin isotopes. The experimental data are some in Fig. 3.14. The dashed lines are calculations with the modified effective interaction using trial density distributions. While the solid lines are best-fit calculations with the modified effective interaction.

4.10 Uncertainties of neutron density distributions

In this section, uncertainties of the neutron density distributions of the tin isotopes are estimated. There are generally two types of uncertainties. One originates from the experiment, and the other originates from the model of calculation. In our case, the reduced chi-square χ^2/ν is larger than 1, and is typically 7 for ^{116,118,122,124}Sn. In the case of ^{120}Sn, not only the cross sections and analyzing powers but also the spin rotation parameters [37] are used as experimental data in the analysis. Thus, the errors for ^{120}Sn resulting from the experimental conditions, degrees of freedom ν and χ^2/ν are different from those for other isotopes. χ^2/ν is about 10 for ^{120}Sn. If the model was perfect, it would realize χ^2/ν=1. Thus, the reason that χ^2/ν >1 is attributed to the inadequacy of our model. To compensate for this inadequacy of the model, we increased the errors artificially by multiplying all the experimental errors by a constant factor to realize χ^2/ν=1. This means that we must redefine Eq. (4.33) as follows;

$$\chi^2 \leq \chi^2_{\rm min} + P \times \chi^2_{\rm min}/\nu. \tag{4.38}$$

The uncertainties of the neutron density distributions are estimated by the following procedure. In the estimations, we additionally took account the ambiguity of the medium effect parameter errors of the effective interaction. First, a new medium-effect parameter set using ^{58}Ni data is obtained by the Monte Carlo method. The parameter sets that satisfy Eq. (4.33) are adopted as "good" medium-effect parameter sets.

Second, the uncertainties of neutron density distributions are estimated using each set of "good" medium-effect parameters. The neutron density distributions are calculated by the Monte Carlo method under the normalization condition of Eq. (4.37). The experimental data are compared with the result of the calculation using each "good" set of medium-effect parameters and the trial neutron density distributions. All trial neutron density distributions that satisfy Eq. (4.38) are adopted as "good" neutron density distributions.

This procedure is repeated until the uncertainty of each "good" neutron density distribution converged. The uncertainties of the neutron density distributions in this analysis are defined as the outskirts of the density distributions at each radial point. The uncertainties of the RMS radii of the neutron density distributions were also calculated using all the neutron density distributions which satisfy Eq. (4.37). The results of deduced point proton and neutron density distributions of tin isotope are shown in Fig. 4.28. The details of the figure are discussed in the next chapter.

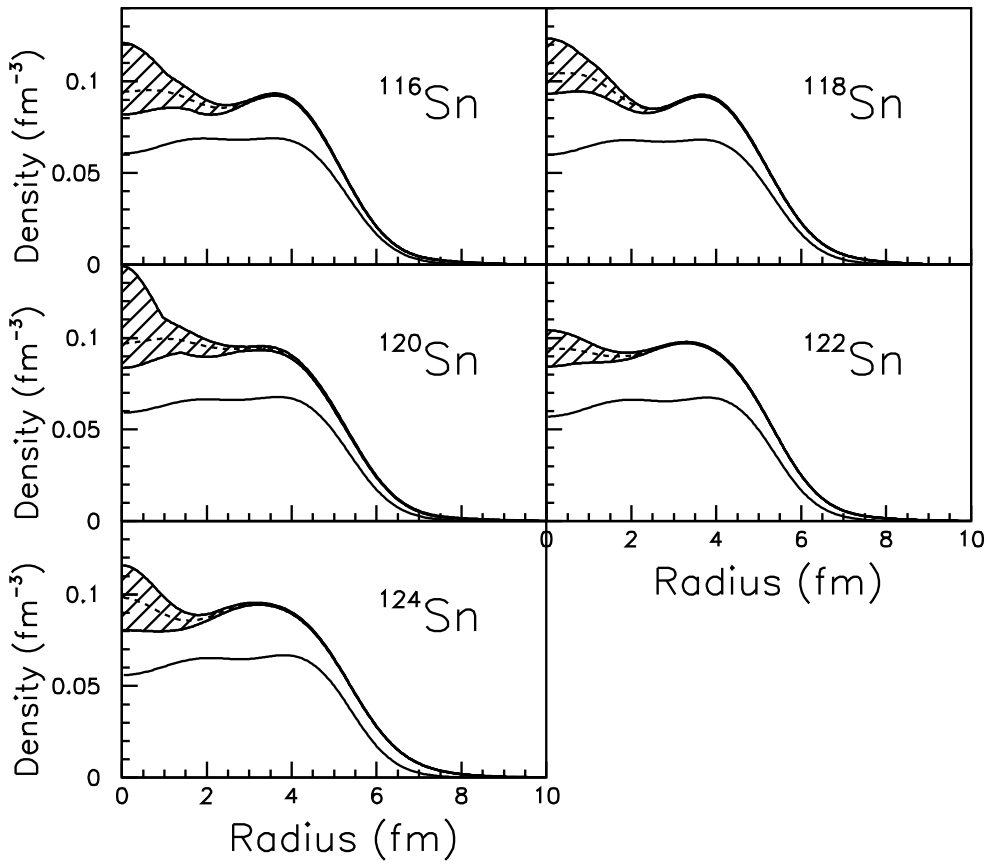

Figure 4.28: Point nucleon density distributions for tin isotopes. Solid lines show point proton density distributions. Dashed lines show best-fit neutron density distributions. Hatched areas represent the error envelopes encompassing all the trial SOG neutron density distributions deduced by the modified effective interaction. Not only statistical and experimental errors but also systematic errors from the model dependence contribute to these regions.

Chapter 5

Results and discussion

5.1 Deduced nucleon density distributions and RMS radii of tin isotopes

Figure 4.28 shows results of the deduced point proton and neutron density distributions of tin isotopes. Solid and dashed lines show point proton and best-fit neutron density distributions, respectively. These densities reproduce charge distributions of Eq. (4.22). Hatched areas are uncertainties of tin isotopes in this analysis, whose area satisfies Eq. (4.38). These uncertainties are calculated by fixing the point proton densities. Each shape of neutron density distribution between tin isotopes is similar. The χ^2/ν for only ^{120}Sn is worse than other isotopes. Thus the uncertainty is larger than other isotopes.

Figure 5.1 shows the typical uncertainty of neutron density distribution for ^{116}Sn. This figure is the same as in the upper-left panel of Fig. 4.28. The uncertainties in the middle panel of Fig. 5.1 are 0.5% at from 3 fm to 6 fm corresponding to shoulder region where number of nucleus per unit radius is maximum, 20% at 0 fm corresponding to nuclear center, and 5% at 8 fm corresponding to tail region of 1-2% of saturation density of neutron, respectively. The results indicate that the nuclear surface is the region most accurately probed by analysis of proton-nucleus elastic scattering at the energy, and this region corresponds to the mean free path in a nucleus of intermediate-energy proton. The lower panel of Fig. 5.1 shows the radial dependence of number of neutron per unit radius $4\pi r^2\rho(r)$ and its uncertainly. This uncertainty of $4\pi r^2\rho(r)$ is very small, which corresponds to 0.2 neutrons per fm. The result shows that the sensitivity for the probability of nucleons covers with the whole region of nuclear density.

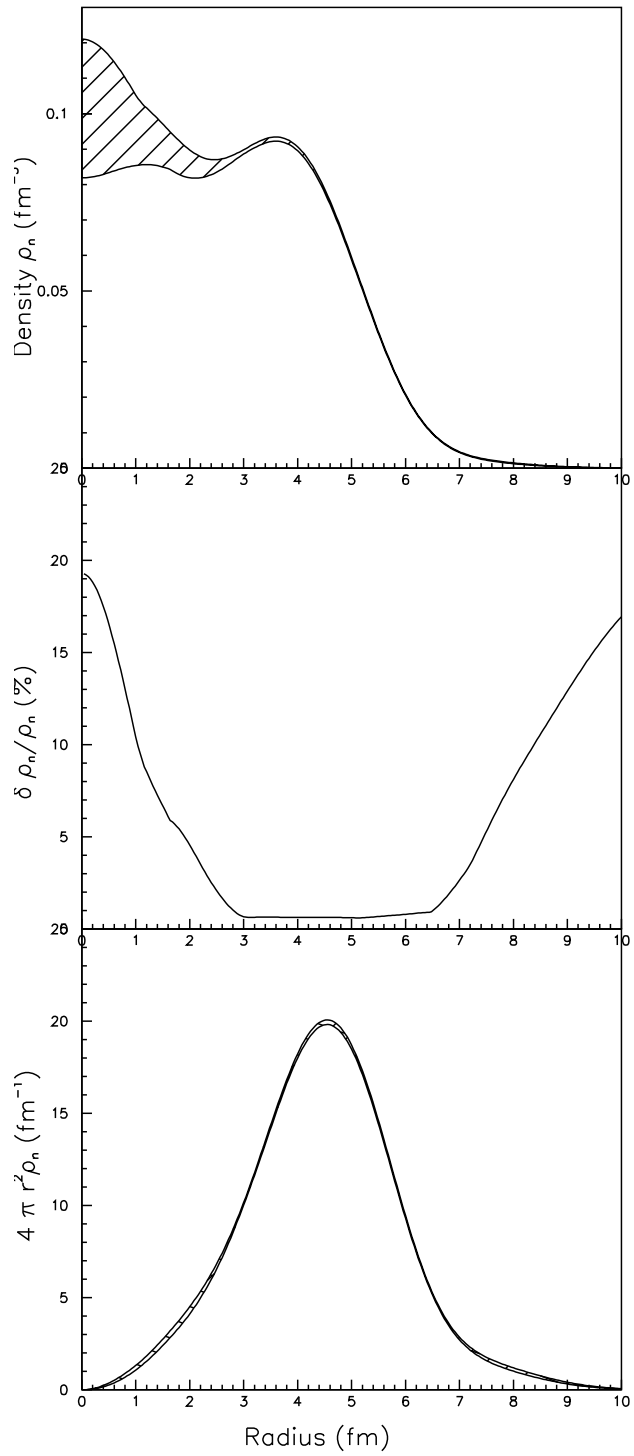

Figure 5.1: The uncertainty in the deduced neutron density distribution for ^{116}Sn as a function of radial position. Upper figure is the same as in Fig. 4.28. Lower figure shows the ratio of uncertainties to absolute value of neutron densities

Figure 5.2 shows our results for point proton and neutron RMS radii and theoretical calculations. Solid lines show RMF calculations with NL3 parameterization. Dashed and dotted lines show SHF calculations with the well-used SIII and SkM* parameterizations. All three calculations include the BCS paring forces. Though the differences from the deduced shapes of neutron density distributions between tin isotopes are not clear due to uncertainties in this analysis as shown in Fig. 4.28, the deduced RMS radii of point proton and neutron density distributions clearly increase with a mass number as shown in Fig. 5.2. This dependence is also shown by several typical theoretical calculations, and these slopes are consistent with present experimental results. Among the calculations, the SHF calculation with SkM* parameterization is in good agreement with the both RMS radii of point proton and neutron density distributions.

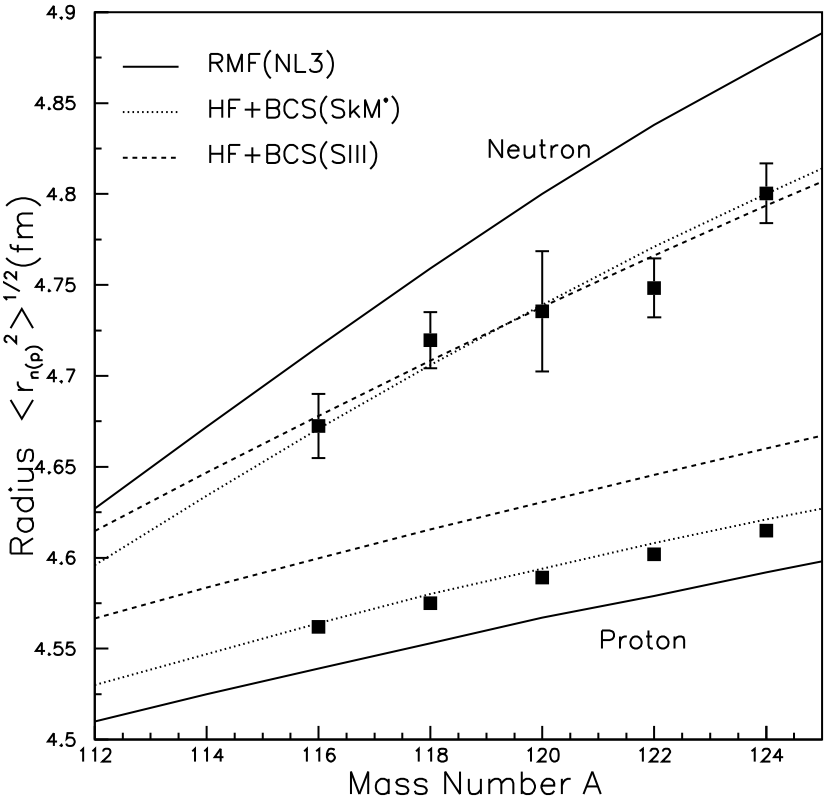

Figure 5.2: Point proton and neutron root mean squared radius of tin isotopes. The solid, dotted, and dashed Line are theoretical calculations with typical mean field model: RMF with NL3 parameterization [79], Skyrme Hartree Fock(SHF) with SkM* parameterization [77, 71] and SHF with SIII parameterization [76], respectively. All calculation are included the BCS pairing effects.

Table 5.1: Reduced RMS radii and thicknesses of tin isotopes.

Target	$\left\langle r_p^2 \right\rangle^{1/2}$ (fm)	$\langle r_n^2 \rangle^{1/2}$ (fm)	Δr_{np} (fm)
^{116}Sn	4.562 ± 0.003	4.672 ± 0.018	0.110 ± 0.018
^{118}Sn	4.575 ± 0.003	4.720 ± 0.016	0.145 ± 0.016
^{120}Sn	4.589 ± 0.003	4.736 ± 0.033	0.147 ± 0.033
^{122}Sn	4.602 ± 0.003	4.748 ± 0.016	0.146 ± 0.016
^{124}Sn	4.615 ± 0.003	4.800 ± 0.017	0.185 ± 0.017

5.2 Neutron skin thicknesses of tin isotopes

Neutron skin thicknesses of tin isotopes Δr_{np} have been measured in several experiments. Two types of experiments have been performed for the Δr_{np} of tin isotopes. One is a nucleon-sensitive probe; proton elastic scattering [31] and antiprotonic X-ray measurements [18]. Another one is an isospin sensitive probe; giant dipole [87] or spin dipole resonances measurements [88]. Figure 5.3 shows a summary of existing experimental results Δr_{np} including our data and theoretical calculations based on the RMF and the SHF. Our results are also summarized in Table 5.1. Proton scattering is a straightforward way to determine the neutron skin thickness Δr_{np} by subtracting the well-known point proton RMS radius from the neutron one. Both of the Δr_{np} for ^{116,124}Sn using 800 MeV proton elastic scattering are slightly larger than our results. However the point proton RMS used in radii of their analysis are smaller than our analysis which is tuned with the electron scattering experiment. Because the charge distribution data used in this work [62] had published latter after Ref. [31]. We think that the proton elastic scattering is mainly sensitive to the matter density not the neutron. The matter RMS radii $\langle r_m^2 \rangle^{1/2}$ of tin isotopes are compared in Table 5.2. The $\langle r_m^2 \rangle^{1/2}$ is calculated using the values in Table 5.1 and Ref. [31] by the following equation as;

$$\sqrt{\langle r_m^2 \rangle} \equiv \sqrt{\frac{Z}{A}\left\langle r_p^2 \right\rangle + \frac{N}{A}\langle r_n^2 \rangle}, \tag{5.1}$$

where, Z, N, and A show a number of proton, neutron, and nucleon, respectively. The experimental data of the 800 MeV by Ray [31] and our 300 MeV results of $\langle r_m^2 \rangle^{1/2}$ for ^{116,124}Sn are consistent regardless of their different analysis as shown in Fig. 5.2. The antiprotonic X-ray measurement provides information on the peripheral shape of nucleon density. In this method, a functional shape of density was assumed like 2pF, due to a few observed values related nuclear structure, and the uncertainty of antiproton-nucleus potential remains. In the other ways to derive Δr_{np}, some isovector dipole resonance measurements are suggested and applied, like Giant- (IVGDR) [87], Spin-(IVSDR) [88], and Pygmy-(IVPDR) [89]. However these methods are model-dependent. And it is not easy to estimate the uncertainty of the model-dependence. Therefore the systematic errors of Δr_{np} of tin isotopes can be larger.

Table 5.2: Reduced matter RMS radius of tin isotope.

Target	This work*1 (fm)	Ray [31]*2 (fm)
^{116}Sn	4.625 ±0.010	4.630±0.029
^{118}Sn	4.659 ±0.009	—
^{120}Sn	4.675 ±0.020	—
^{122}Sn	4.689 ±0.010	—
^{124}Sn	4.725 ±0.010	4.751±0.030

*1 295 MeV (p,p) with RIA.
*2 800 MeV (p,p) with 2nd-order KMT.
Here, the uncertainties of proton RMS radii are assumed to 0.005 fm.

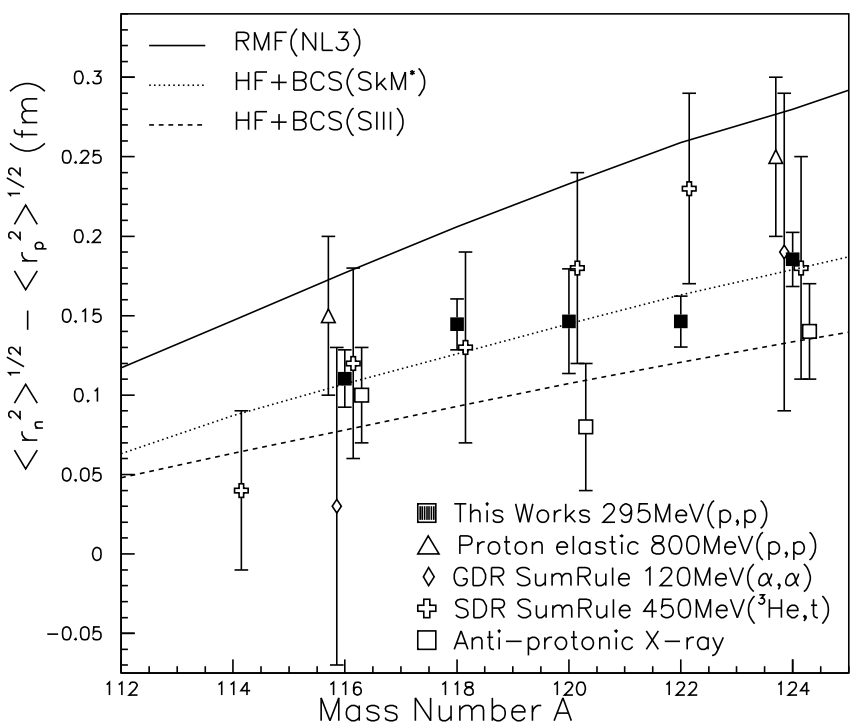

Figure 5.3: Neutron skin thicknesses of tin isotopes obtained in various method. Our results are indicated by solid squares. Results from proton elastic scattering at 800MeV [31], giant dipole resonances [87], spin dipole resonances [88] and antiprotonic X-ray data [18] are open triangles, open diamonds, open crosses, open squares, respectively. The lines as describe in Fig. 5.2.

In Fig. 5.3, our results which indicated by solid squares are more precise than other results, and are consistent with them within the errors. We notice the gradual increase of the Δr_{np} with mass number. But the values of our result are not so large as the predicted ones by the RMF model. It is because the RMF model predicts the smaller proton RMS radii and the larger neutron RMS radii as shown in Fig 5.2. On the contrary, our experimental values are slightly larger than the dashed lines of the SHF calculations using SIII parameterization. They are in agreement with dotted lines of SkM* as shown in Fig 5.2.

The neutron skin thickness Δr_{np} is theoretically related to one of the EOS properties; the symmetry energy $a_{\rm sym}$ at the saturation density ρ_0 [42, 43, 44, 41]. The EOS properties of typical mean field calculations used in this work are summarized in Appendix C. If a linear relation which they suggested between the Δr_{np} of tin isotopes and the $a_{\rm sym}$ is assumed in the stable region, the value of $a_{\rm sym}$ can be deduced. Chen *et al.* also showed the correlation between the Δr_{np} of various nuclei and the density dependence of the symmetry energy L, whose correlation is stronger than the one between the Δr_{np} and the $a_{\rm sym}$ [41] as shown in Fig. 5.4. They calculated neutron skin thicknesses S of ^{208}Pb, ^{132,124}Sn, and ^{48}Ca using twenty-one sets of SHF parameters. They showed the existence of the strong correlation between the S and the L and of the weaker but significant correlation between the S and the $E_{\rm sym}$ which is written as $a_{\rm sym}$ in this thesis for heavier nuclei ^{208}Pb, ^{132,124}Sn. The three parameterizations (SIII, SkM*, and NL3) are used as theoretical calculations, which guide the Δr_{np} to the $a_{\rm sym}$ and the L. By the theoretical calculations, we have extracted the $a_{\rm sym}$ and the L for each tin isotope by assuming the linear relation.

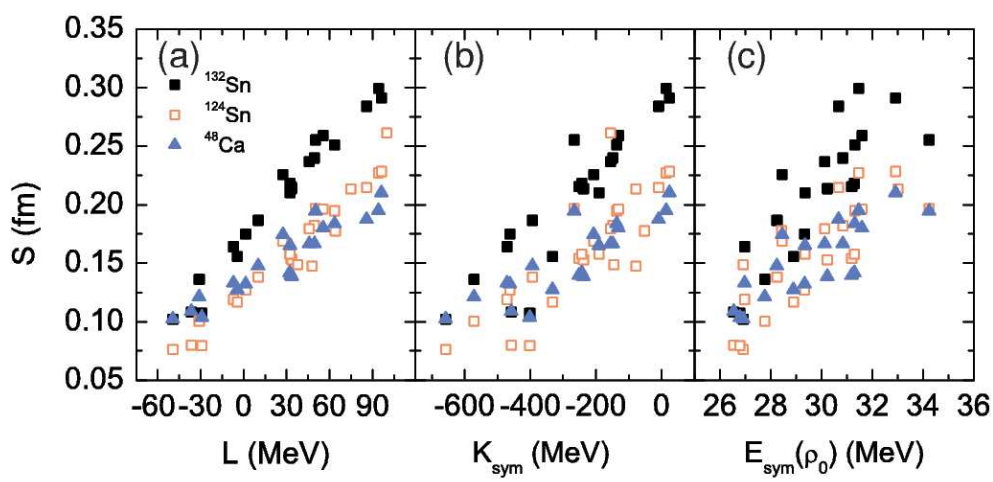

Figure 5.4: Neutron skin thickness S of ^{48}Ca, ^{124,132}Sn as a function of symmetry energy coefficient $E_{\rm sym}(a_{\rm sym})$ at the saturation density (c) and its first- and second-derivative density dependence L (a) and $K_{\rm sym}$ (b), respectively [41].

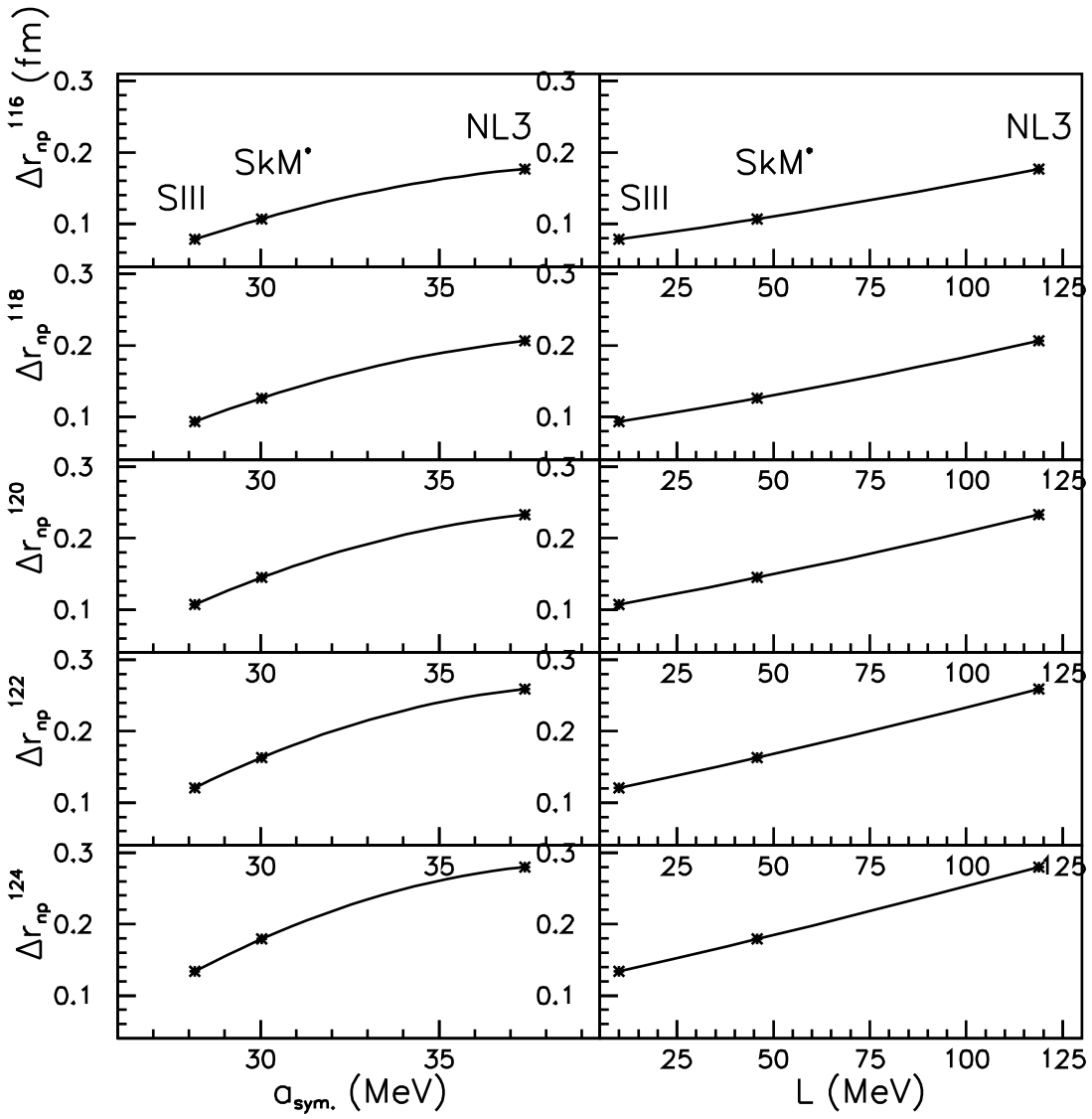

Figure 5.5: Symmetry energy coefficient $a_{\rm sym}$ at the saturation density and its density dependence L near the ρ_0 as function as the skin thickness of ^{116,118,120,122,124}Sn. Left and right panels show the correlation between the $a_{\rm sym}$ and the L and the Δr_{np} of tin isotopes, respectively. All lines represent a quadratic fit.

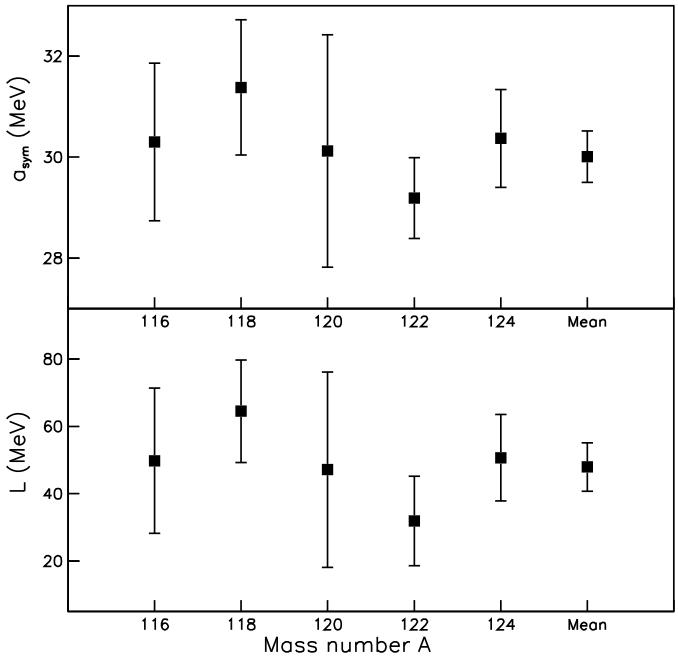

Figure 5.6: The results of the symmetry energy coefficient $a_{\rm sym}$ and its density dependence L for tin isotopes.

Figure 5.5 shows the $a_{\rm sym}$ and the L as function as the neutron skin thickness for ^{116,118,120,122,124}Sn in the left and the right panels of this figure, respectively. All panels in Fig. 5.5 represent that the $a_{\rm sym}$ and the L are strong correlations with the thickness of neutron skin. In order to deduce the $a_{\rm sym}$ and the L from Fig. 5.5, we have fitted by a quadratic function using the three theoretical calculations. Figure 5.6 shows results of the $a_{\rm sym}$ and the L for ^{116,118,120,122,124}Sn whose values are interpolated using the quadratic function. The mean values of the $a_{\rm sym}$ and the L are deduced using the relation in Fig. 5.5 as follows;

$$\begin{aligned} a_{\rm sym} &= 30.0\ ^{+0.5}_{-0.4}\ \pm\ 2.0_{\rm sys.}\ ({\rm MeV}) \\ L &= 47.9\ ^{+7.2}_{-7.9}\ \pm\ 15.0_{\rm sys.}\ ({\rm MeV}), \end{aligned}$$

where, the last values are systematic errors of this procedure. Yoshida *et al.* [42] and Chen *et al.* [41] claimed a fluctuation about 2 MeV against to the linear relations between the $a_{\rm sym}$ and the Δr_{np}. The fluctuation is also shown in the case of the L, and its value is estimated from result of fitting for ^{124}Sn by Chen *et al.* [41]. The value is about 15 MeV. Thus the systematic error of determination using this procedure for the $a_{\rm sym}$ and the L are estimated about $\pm$ 2 MeV and $\pm$ 15 MeV, respectively.

5.3 Nuclear surface diffuseness of tin isotopes

An increase of neutron skin thickness with mass number is observed in tin isotopes. Next the surface diffuseness is also investigated about a dependence with mass number in this section. The determination of nuclear surface diffuseness is generally difficult, because there is a small oscillating behavior from specific shell structures, although a nucleon density at an inner medium has almost a uniform density. We now define the nuclear surface diffuseness from a nuclear surface shape of densities by differentiating the density distribution. A way of deducing the diffuseness is described in detail in Appendix D. The errors of the obtained values of neutron densities are estimated only from the error envelop of density distribution in Fig. 4.28. But the errors of the proton and the charge diffuseness are not estimated due to a lack of the error band information, however these errors from the surface structures might be small.

Figure 5.7 shows the surface diffuseness of tin isotopes. The filled triangles, inverted triangles, and circles show the deduced surface diffuseness of charge, proton, and neutron, respectively. Open squares and triangles shows values of diffuseness using existing 3pG and SOG charge distributions [7] to discuss a systematic behavior of the isotopes. The diffuseness of point proton distribution is shown in the case of 3pG and SOG charge distribution. The diffuseness of neutron is also shown as a function of mass number in Fig. 5.7. In tin isotopes, the slope of neutron is larger than that of proton. The diffuseness of charge and proton slightly decrease, but the diffuseness of neutron distinctly increase. These difference between proton and neutron distribution might be qualitatively reflected from a sign of dependence of one nucleon separation energy with mass number.

On the other hand, theoretical calculations of the SHF with SkM* parameterizations are also shown in Fig 5.7. Solid and dashed lines show the surface diffuseness of proton and neutron. These values are almost constant for both proton and neutron. The results imply that the nuclear diffuseness is not described from only the separation energy of nucleon, and the reason remains an open question. The calculations using other parameterizations (SIII and L-HS) also show a similar behavior, but the values are smaller than the case of SkM*. Thus the point proton and neutron density distributions using SIII or L-HS parameterizations have stiff surfaces than experimental results.

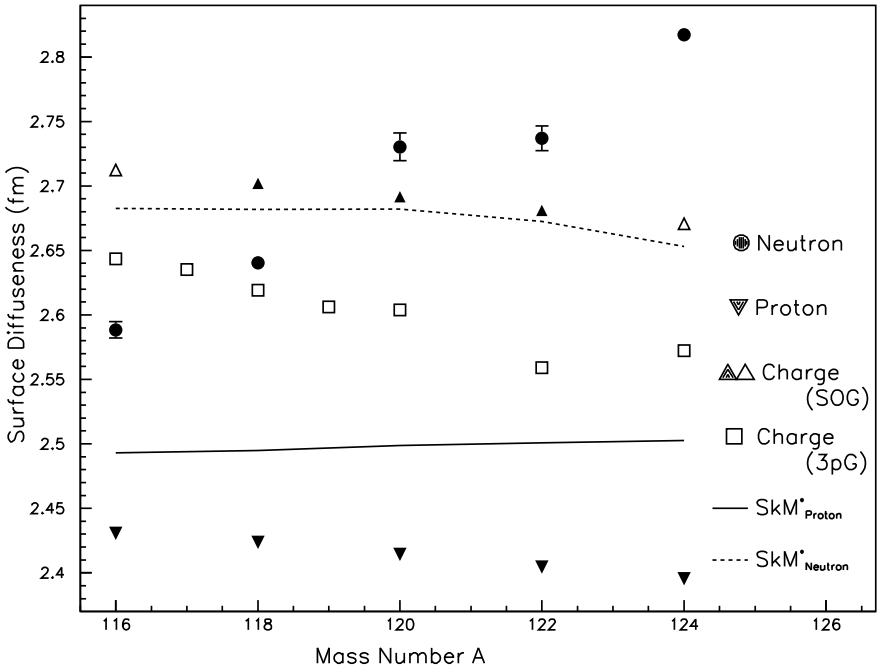

Figure 5.7: The surface diffuseness of tin isotopes. Filled circles and triangle are surface diffuseness of proton and neutron density. Squared, and triangles are surface diffuseness of 3pG, SOG charge distributions, respectively. Here, open symbols show values using existing charge distribution data [7], and filled symbols show deduced values in this work. Solid and dashed lines show the theoretical calculations for the diffuseness for proton and neutron, respectively.

Chapter 6

Conclusion

Differential cross sections and analyzing powers of the proton elastic scattering at 295 MeV were measured for the ^{116,118,120,122,124}Sn targets up to 3.5 fm^{-1} momentum transfer at WS beam course of the RCNP ring cyclotron. The experimental data were analyzed in the framework of the RIA using the newly tuned RLF interaction obtained for ^{58}Ni.

With the tuned interaction in the nuclear medium, the neutron density distributions of the tin isotopes are deduced so as to reproduce the proton elastic scattering data of the tin isotopes. The point proton distribution were unfolded using charge distribution and nucleon electric form factors which reproduce the existing experimental data in the large momentum transfer region. The uncertainties of neutron density distributions are estimated in consideration with not only experimental but also model uncertainty which were not explicitly included previously. It is found that the dominant component of uncertainties for the neutron density distributions is the applied effective interaction, not the ambiguity of scalar density nor the multistep process.

The RMS radii of point proton and neutron density distributions are deduced from the point proton unfolded from the charge distribution and neutron density distributions obtained in this analysis, and compared with several theoretical mean field calculations. The clear increase of RMS radii for point proton and neutron density distributions with mass number is observed. The neutron skin thicknesses and the surface diffuseness of the tin isotopes are deduced, and are compared with several theoretical calculations. The increase of the deduced skin thicknesses with mass number is also observed. The SHF calculation using SkM* parameterization is in good agreement with our results, the RMS radius of proton and neutron and the neutron skin thickness. The symmetry energy of the EOS, $a_{\rm sym}$, is deduced from the value of the Δr_{np} using theoretical calculations used typical parameter sets (SIII, SkM*, and NL3). The obtained value of $a_{\rm sym}$ is $30.0\ ^{+0.5}_{-0.4}\ \pm\ 2.0_{\rm sys}$ MeV, and the density dependence of the $a_{\rm sym}$ is also discussed. The obtained value of L is about $47.9\ ^{+7.2}_{-7.9}\ \pm\ 15.0_{\rm sys.}$ MeV.

Acknowledgments

First of all, I would like to express my sincere gratitude to Prof. Harutaka Sakaguchi, who is my supervisor. He has guided me through long periods since the beginning of my research career and given me good opportunities to study elastic scattering but also many experimental nuclear physics. I have learned from him not only the knowledge of nuclear physics but also attitudes to solve scientific problems. And his careful proofreading of the present thesis was gratefully helpful.

I have spent my graduate school days as a member of the "Experimental Nuclear and Hadronic Physics (NH)" group in Kyoto University. I would like to thank acknowledge Prof. Ken'ichi Imai for his guidance and encouragement. He is one of who guide me to the physics world. I would like to thank acknowledge Prof. Masaru Yosoi. He has advised me about the experiments and analysis. I have learned from him skillful experiment and analysis technique. I would like to thank acknowledge Prof. Tetsuya Murakami for his advise of work and physics. I have learned from his rich knowledge. I wish to acknowledge the help and encouragement by Prof. Masanobu Nakamura, Prof. Naohito Saito, Prof. Haruhiko Funahashi for their guidance. I would like to appreciate helpful discussions with Mr. Juzo Zenihiro. His analysis and discussion affect me very much give some hint for physics. I would like to thank members of NH group in the same grade, Dr. Yoshinori Fukao, Mr. Terunao Nakura, Dr. Hiromi Okada, Dr. Shinsuke Ota, Dr. Koji Miwa, Dr. Manabu Togawa for friendships and encouragements. Talk and discussion with them make my graduate school days fruitful and enjoyable

I express my special thanks to all the collaborators of the RCNP-E147 experiment Prof. H. Sakaguchi, Prof. T. Murakami, Prof. M. Yosoi, Dr. H. Takeda, Dr. M. Itoh, Dr. T. Kawabata, Dr. T. Ishikawa, Dr. M. Uchida, Dr. Y. Yasuda, Prof. T. Noro, Dr. H. P. Yoshida, Dr. S. Ishida, Mr. S. Asaji, and Mr. Yonemura. I wish to thank again Hidetomo P. Yoshida. He is the specialist of the Grand Raiden trigger system, worked for circuit arrangement of our target system.

I spent many times during graduate student at RCNP. I wish to thank Prof. H. Akimune, Dr. K. Nakanishi, Dr. K. Kawase. They work together in some experiments at RCNP. We would like to thank Prof. Hatanaka, Dr. Minomiya, and operating crew of RCNP for their support, for providing clear, stable, and high intensity beam during the experiment and also for beam time managements. This analysis are mainly performed RCNP main server.

I have spent invaluable years in RIKEN Nishina Center. I would like to thank acknowledge Prof. H. Sakurai, who is my adviser for researches at RIKEN. He has encouraged me to complete the doctoral work. I would like to thank acknowledge Prof. T. Motobayashi, Prof. T. Suda They have given many supports. I also wish to thanks to all the member of the Radio-Isotope Physics Laboratory, and the Heavy-Ion Physics Laboratory at RIKEN Nishina Center. Some among them now collaborates with me for the coming experiment at RIBF.

I would like to express my appreciation to my family at my home town, my sister, brother, grandmother and my parents; Kiyoshi and Emiko. They have supported and encouraged me. Finally, I would like to express my special thanks to my wife Sayaka for her cheering and respect on my work on physics and life.

Appendix A

Digital data

The experimental results of differential cross sections and analyzing powers up to high momentum transfer region 3.5^{-1} in the 295 MeV proton elastic scattering of ^{116,118,120,122,124}Sn are summarized in some tabular form.

Table A.1: Cross sections and analyzing powers of ^{116}Sn

θ_{cm} (degree)	$d\sigma/d\Omega$ (mb/sr)	Ay
7.08	$(2.661 \pm 0.084)\times 10^{3}$	0.379 ± 0.033
8.09	$(9.259 \pm 0.028)\times 10^{3}$	0.470 ± 0.033
9.10	$(2.083 \pm 0.064)\times 10^{2}$	0.533 ± 0.034
10.11	$(4.576 \pm 0.150)\times 10^{1}$	0.774 ± 0.038
11.63	$(1.558 \pm 0.049)\times 10^{2}$	0.831 ± 0.039
13.14	$(1.904 \pm 0.058)\times 10^{2}$	0.842 ± 0.039
14.66	$(1.103 \pm 0.034)\times 10^{2}$	0.838 ± 0.039
16.18	$(3.470 \pm 0.115)\times 10^{1}$	0.656 ± 0.036
17.69	$(6.265 \pm 0.237)\times 10^{0}$	-0.400 ± 0.034
19.21	$(7.546 \pm 0.267)\times 10^{0}$	0.562 ± 0.035
20.72	$(1.209 \pm 0.040)\times 10^{1}$	0.962 ± 0.042
22.24	$(1.018 \pm 0.034)\times 10^{1}$	0.887 ± 0.040
23.75	$(5.149 \pm 0.018)\times 10^{0}$	0.542 ± 0.035
25.27	$(1.640 \pm 0.063)\times 10^{0}$	-0.245 ± 0.033
26.79	$(6.970 \pm 0.256)\times 10^{0}$	-0.412 ± 0.034
28.30	$(1.008 \pm 0.034)\times 10^{0}$	0.726 ± 0.037
29.82	$(1.137 \pm 0.037)\times 10^{0}$	0.851 ± 0.040
31.33	$(7.729 \pm 0.258)\times 10^{-1}$	0.638 ± 0.036
32.84	$(3.328 \pm 0.110)\times 10^{-1}$	0.160 ± 0.031
34.35	$(9.371 \pm 0.334)\times 10^{-2}$	-0.673 ± 0.037
35.87	$(7.167 \pm 0.267)\times 10^{-2}$	0.122 ± 0.032
37.38	$(1.082 \pm 0.042)\times 10^{-1}$	0.761 ± 0.039
38.89	$(1.014 \pm 0.034)\times 10^{-1}$	0.736 ± 0.038
40.41	$(5.619 \pm 0.200)\times 10^{-2}$	0.567 ± 0.036
41.92	$(1.754 \pm 0.061)\times 10^{-2}$	0.102 ± 0.032
43.43	$(4.080 \pm 0.175)\times 10^{-3}$	-0.610 ± 0.038
44.94	$(6.405 \pm 0.317)\times 10^{-3}$	0.677 ± 0.041
46.45	$(8.947 \pm 0.393)\times 10^{-3}$	0.825 ± 0.041
47.96	$(6.711 \pm 0.266)\times 10^{-3}$	0.783 ± 0.040
49.48	$(3.088 \pm 0.167)\times 10^{-3}$	0.625 ± 0.042
50.99	$(6.348 \pm 0.383)\times 10^{-4}$	0.115 ± 0.041

Table A.2: Cross sections and analyzing powers of ^{118}Sn

θ_{cm} (degree)	$d\sigma/d\Omega$ (mb/sr)	Ay
7.08	$(2.544 \pm 0.080)\times 10^{3}$	0.417 ± 0.033
8.09	$(1.030 \pm 0.031)\times 10^{3}$	0.494 ± 0.034
9.10	$(1.999 \pm 0.062)\times 10^{2}$	0.556 ± 0.034
10.11	$(4.601 \pm 0.155)\times 10^{1}$	0.818 ± 0.039
11.63	$(1.517 \pm 0.049)\times 10^{2}$	0.754 ± 0.038
13.14	$(1.909 \pm 0.058)\times 10^{2}$	0.846 ± 0.039
14.66	$(1.093 \pm 0.034)\times 10^{2}$	0.810 ± 0.038
16.18	$(3.321 \pm 0.108)\times 10^{1}$	0.617 ± 0.035
17.69	$(5.614 \pm 0.222)\times 10^{0}$	-0.492 ± 0.035
19.21	$(8.074 \pm 0.281)\times 10^{0}$	0.655 ± 0.037
20.72	$(1.249 \pm 0.041)\times 10^{1}$	0.971 ± 0.042
22.24	$(9.868 \pm 0.326)\times 10^{0}$	0.874 ± 0.040
23.75	$(4.745 \pm 0.168)\times 10^{0}$	0.519 ± 0.034
25.27	$(1.454 \pm 0.056)\times 10^{0}$	-0.400 ± 0.034
26.79	$(7.193 \pm 0.263)\times 10^{-1}$	-0.244 ± 0.032
28.30	$(1.078 \pm 0.034)\times 10^{0}$	0.725 ± 0.037
29.82	$(1.190 \pm 0.038)\times 10^{0}$	0.826 ± 0.039
31.33	$(7.910 \pm 0.254)\times 10^{-1}$	0.573 ± 0.035
32.84	$(2.944 \pm 0.097)\times 10^{-1}$	0.061 ± 0.031
34.36	$(8.319 \pm 0.306)\times 10^{-2}$	-0.777 ± 0.039
35.87	$(8.002 \pm 0.284)\times 10^{-2}$	0.308 ± 0.033
37.38	$(1.163 \pm 0.042)\times 10^{-1}$	0.770 ± 0.039
38.90	$(9.976 \pm 0.345)\times 10^{-2}$	0.705 ± 0.038
40.41	$(5.012 \pm 0.183)\times 10^{-2}$	0.498 ± 0.035
41.92	$(1.392 \pm 0.051)\times 10^{-2}$	-0.039 ± 0.032
43.44	$(4.083 \pm 0.183)\times 10^{-3}$	-0.427 ± 0.037
44.95	$(7.400 \pm 0.432)\times 10^{-3}$	0.702 ± 0.043
46.46	$(9.543 \pm 0.429)\times 10^{-3}$	0.862 ± 0.042
47.97	$(6.349 \pm 0.265)\times 10^{-3}$	0.772 ± 0.040
49.48	$(2.430 \pm 0.147)\times 10^{-3}$	0.553 ± 0.043
50.99	$(4.337 \pm 0.313)\times 10^{-4}$	-0.097 ± 0.047

Table A.3: Cross sections and analyzing powers of ^{120}Sn

θ_{cm} (degree)	$d\sigma/d\Omega$ (mb/sr)	Ay
10.11	$(4.336 \pm 0.190)\times 10^{1}$	0.858 ± 0.042
11.63	$(1.474 \pm 0.060)\times 10^{2}$	0.786 ± 0.040
13.14	$(1.585 \pm 0.055)\times 10^{2}$	0.868 ± 0.040
14.66	$(8.291 \pm 0.263)\times 10^{1}$	0.825 ± 0.039
16.17	$(2.224 \pm 0.079)\times 10^{1}$	0.555 ± 0.035
17.69	$(4.308 \pm 0.210)\times 10^{0}$	-0.494 ± 0.038
19.20	$(7.718 \pm 0.323)\times 10^{0}$	0.742 ± 0.039
20.72	$(1.074 \pm 0.041)\times 10^{1}$	0.990 ± 0.043
22.24	$(8.237 \pm 0.329)\times 10^{0}$	0.834 ± 0.041
23.75	$(3.969 \pm 0.167)\times 10^{0}$	0.400 ± 0.035
25.27	$(1.214 \pm 0.075)\times 10^{0}$	-0.531 ± 0.043
26.78	$(7.631 \pm 0.252)\times 10^{-1}$	0.040 ± 0.031
28.30	$(1.158 \pm 0.045)\times 10^{0}$	0.823 ± 0.040
29.81	$(1.065 \pm 0.039)\times 10^{0}$	0.822 ± 0.040
31.32	$(6.186 \pm 0.251)\times 10^{-1}$	0.488 ± 0.036
32.84	$(2.087 \pm 0.090)\times 10^{-1}$	-0.186 ± 0.034
34.35	$(7.199 \pm 0.329)\times 10^{-2}$	-0.618 ± 0.039
35.87	$(9.703 \pm 0.401)\times 10^{-2}$	0.599 ± 0.037
37.38	$(1.185 \pm 0.050)\times 10^{-1}$	0.740 ± 0.039
38.89	$(8.402 \pm 0.374)\times 10^{-2}$	0.678 ± 0.039
40.41	$(3.418 \pm 0.156)\times 10^{-2}$	0.333 ± 0.036
41.92	$(8.632 \pm 0.519)\times 10^{-3}$	-0.406 ± 0.042
43.43	$(4.877 \pm 0.287)\times 10^{-3}$	0.204 ± 0.041
44.94	$(9.283 \pm 0.501)\times 10^{-3}$	0.829 ± 0.044
46.45	$(9.537 \pm 0.497)\times 10^{-3}$	0.822 ± 0.043
47.96	$(5.487 \pm 0.278)\times 10^{-3}$	0.706 ± 0.041
49.48	$(1.780 \pm 0.116)\times 10^{-3}$	0.376 ± 0.043

Table A.4: Cross sections and analyzing powers of ^{122}Sn

θ_{cm} (degree)	$d\sigma/d\Omega$ (mb/sr)	Ay
11.62	$(1.882 \pm 0.061)\times 10^{2}$	0.749 ± 0.038
13.14	$(1.937 \pm 0.061)\times 10^{2}$	0.783 ± 0.038
14.65	$(9.531 \pm 0.292)\times 10^{1}$	0.792 ± 0.038
16.17	$(2.408 \pm 0.078)\times 10^{1}$	0.517 ± 0.034
17.69	$(4.796 \pm 0.188)\times 10^{0}$	-0.480 ± 0.035
19.20	$(9.685 \pm 0.334)\times 10^{0}$	0.811 ± 0.039
20.72	$(1.337 \pm 0.044)\times 10^{1}$	1.007 ± 0.043
22.23	$(1.022 \pm 0.035)\times 10^{1}$	0.783 ± 0.039
23.75	$(4.661 \pm 0.166)\times 10^{0}$	0.361 ± 0.033
25.26	$(1.258 \pm 0.066)\times 10^{0}$	-0.636 ± 0.041
26.78	$(9.276 \pm 0.358)\times 10^{-1}$	0.175 ± 0.033
28.29	$(1.367 \pm 0.048)\times 10^{0}$	0.821 ± 0.039
29.80	$(1.236 \pm 0.041)\times 10^{0}$	0.756 ± 0.038
31.32	$(6.601 \pm 0.233)\times 10^{-1}$	0.432 ± 0.034
32.83	$(2.156 \pm 0.081)\times 10^{-1}$	-0.294 ± 0.033
34.35	$(8.261 \pm 0.338)\times 10^{-2}$	-0.496 ± 0.036
35.86	$(1.201 \pm 0.042)\times 10^{-1}$	0.652 ± 0.037
37.37	$(1.358 \pm 0.054)\times 10^{-1}$	0.778 ± 0.040
38.88	$(9.228 \pm 0.345)\times 10^{-2}$	0.640 ± 0.037
40.40	$(3.536 \pm 0.135)\times 10^{-2}$	0.245 ± 0.033
41.91	$(8.290 \pm 0.391)\times 10^{-3}$	-0.563 ± 0.039
43.42	$(7.053 \pm 0.297)\times 10^{-3}$	0.350 ± 0.035
44.93	$(1.176 \pm 0.048)\times 10^{-2}$	0.804 ± 0.040
46.45	$(1.119 \pm 0.045)\times 10^{-2}$	0.785 ± 0.040
47.96	$(6.046 \pm 0.242)\times 10^{-3}$	0.662 ± 0.038
49.47	$(1.640 \pm 0.083)\times 10^{-3}$	0.200 ± 0.037

Table A.5: Cross sections and analyzing powers of ^{124}Sn

θ_{cm} (degree)	$d\sigma/d\Omega$ (mb/sr)	Ay
10.11	$(5.062 \pm 0.175)\times 10^{1}$	0.808 ± 0.041
11.62	$(1.593 \pm 0.044)\times 10^{2}$	0.773 ± 0.039
13.14	$(1.562 \pm 0.042)\times 10^{2}$	0.829 ± 0.040
14.65	$(7.456 \pm 0.176)\times 10^{1}$	0.836 ± 0.039
16.17	$(1.835 \pm 0.052)\times 10^{1}$	0.482 ± 0.035
17.68	$(4.413 \pm 0.178)\times 10^{0}$	-0.347 ± 0.037
19.20	$(8.625 \pm 0.281)\times 10^{0}$	0.853 ± 0.041
20.71	$(1.120 \pm 0.033)\times 10^{1}$	0.986 ± 0.043
22.23	$(7.886 \pm 0.258)\times 10^{0}$	0.814 ± 0.040
23.74	$(3.579 \pm 0.127)\times 10^{0}$	0.322 ± 0.035
25.26	$(1.035 \pm 0.038)\times 10^{0}$	-0.693 ± 0.038
26.77	$(9.141 \pm 0.348)\times 10^{-1}$	0.312 ± 0.034
28.29	$(1.326 \pm 0.043)\times 10^{0}$	0.856 ± 0.040
29.80	$(1.114 \pm 0.028)\times 10^{0}$	0.755 ± 0.038
31.31	$(5.710 \pm 0.153)\times 10^{-1}$	0.378 ± 0.033
32.83	$(1.785 \pm 0.057)\times 10^{-1}$	-0.408 ± 0.035
34.34	$(8.373 \pm 0.297)\times 10^{-2}$	-0.283 ± 0.035
35.85	$(1.241 \pm 0.034)\times 10^{-1}$	0.692 ± 0.037
37.37	$(1.324 \pm 0.041)\times 10^{-1}$	0.747 ± 0.039
38.88	$(8.313 \pm 0.253)\times 10^{-2}$	0.573 ± 0.036
40.39	$(2.830 \pm 0.096)\times 10^{-2}$	0.118 ± 0.034
41.90	$(6.959 \pm 0.304)\times 10^{-3}$	-0.681 ± 0.041
43.41	$(8.072 \pm 0.278)\times 10^{-3}$	0.486 ± 0.036
44.93	$(1.244 \pm 0.042)\times 10^{-2}$	0.782 ± 0.040
46.44	$(1.076 \pm 0.038)\times 10^{-2}$	0.770 ± 0.040
47.95	$(5.148 \pm 0.184)\times 10^{-3}$	0.583 ± 0.038
49.46	$(1.227 \pm 0.063)\times 10^{-3}$	0.061 ± 0.044

Appendix B

Schrodinger Equivalent Form

In this appendix, the Schrodinger equivalent potential for the Dirac equation which contains Lorentz potentials is shown. The Dirac equation for the projectile is written as;

$$(-\boldsymbol{\alpha}\cdot\boldsymbol{\nabla}+U^V(r,E)+\beta[M+U^S(r,E)])\psi(r)=E\psi(r), \tag{B.1}$$

where ψ is the incident projectile wave function, E is the total energy in center of mass coordinate system, and M is the mass of the proton $\boldsymbol{\alpha}$, β is Dirac matrix. This equation contains local, spin-orbit, and non-local potentials, but the non-locality can be removed by rewriting the upper wave function as;

$$A^{1/2}(r,E)u(x), \qquad A(r,E)\equiv 1+\frac{U^S(r,E)-U(r,E)}{E+M} \tag{B.2}$$

After same algebra, the equation for the new two-component function *u(x)* becomes

$$(-\nabla^2+V_C+V_{SO}\,\boldsymbol{\sigma}\cdot\boldsymbol{L}+V_D)u(x)=(E^2-M^2)u(x), \tag{B.3}$$

where, the energy-dependent optical potentials are written as;

$$V_C(r,E) \equiv 2MU^S+2EU^V+(U^S)^2+(U^V)^2, \tag{B.4}$$

$$V_{SO}(r,E) \equiv -\frac{1}{r}+(U^S)^2\frac{B'}{B}, \tag{B.5}$$

$$V_D(r,E) \equiv \frac{3}{4}(\frac{B'}{B})^2-\frac{1}{r}\frac{B'}{B}-\frac{1}{2}\frac{B''}{B}, \tag{B.6}$$

$$\tag{B.7}$$

where, $B(r,E)\equiv(E+M)A(r,E)$. The prime ' denotes a radial derivative, and the small tensor and Coulomb potentials which are ignored. These potentials are similar to Schrodinger potentials, and are called a Schrodinger equivalent potential. These potentials using the relativistic approach can be compared with with the non-relativistic potentials.

Appendix C

The SHF and RMF parameterization and the EOS property

In this thesis, we discuss some effective interactions and asymmetry energies. The Skyrme force is a effective zero-range force with density-dependent and momentum-dependent terms. Hamiltonian density for Skyrme Hartree-Fock calculation is shown as;

$$\begin{aligned} H(\rho_n,\rho_p) &= \frac{h^2}{2m}(\tau_n+\tau_p)+\frac{1}{4}t_0(1-x_0)(\rho_n^2+\rho_p^2)+t_0(1+\frac{1}{2}x_0)\rho_n\rho_p+\frac{1}{12}t_3(1+\frac{1}{2}x3_)\rho^{\alpha+2} \\ &-\frac{1}{12}t_3(\frac{1}{2}+x_3)]\rho^{\alpha}(\rho_n^2+\rho_p^2)+\frac{1}{8}(t_1)(1-x_1)+3t_2(1+x_2))(\rho_n\tau_n+\rho_p\tau_p) \\ &+\frac{1}{4}(t_1(1+\frac{1}{2})+t_2(1+\frac{1}{2}))(\rho_n\tau_p+\rho_p\tau_n)-\frac{3}{32}(t_1(1-x_1) \\ &-t_2(1+x_2))(\rho_n\nabla^2\rho_n+\rho_p\nabla^2\rho_p)-\frac{1}{16}(3t_1(1+\frac{1}{2}) \\ &-t_2(1+\frac{1}{2}x_2))(\rho_n\nabla^2\rho_p+\rho_p\nabla^2\rho_n)-\frac{1}{2}W(\rho\boldsymbol{\nabla})(\rho\boldsymbol{\nabla}\cdot\boldsymbol{J}+\rho_n\boldsymbol{\nabla}\cdot\boldsymbol{J_n} \\ &+\rho_p\boldsymbol{\nabla}\cdot\boldsymbol{J_p})q+H_{Coul}-\frac{1}{16}(t_1x_1+t_2x_2)\boldsymbol{J}^2+\frac{1}{16}(t_1-t_2)(\boldsymbol{J}_n^2+\boldsymbol{J}_p^2), \end{aligned} \tag{C.1}$$

where ρ_n (ρ_p) is the density of neutron (proton) and $\rho=\rho_n+\rho_p$, while τ_n (τ_p), and $\boldsymbol{J}_n$ ($\boldsymbol{J}_p$) are the kinetic energy and the spin-orbit densities of neutron (proton), respectively.

On the other hand, the RMF model with nonlinear meson couplings is consist of nucleons, scalar σ, vector ω, charged ρ mesons, and photons. The relativistic Lagrangian is expressed as;

$$\begin{aligned} L &= \bar{\psi}(i\gamma^\mu\partial_\mu-M-g_\sigma\sigma-g_\omega\gamma^\mu\omega_\mu-g_\rho\gamma^\mu\boldsymbol{\tau}\boldsymbol{b}_\mu-e\gamma^\mu\frac{1-\tau_3}{2}A_\mu)\psi \\ &+\frac{1}{2}(\partial_\mu\partial^\mu\sigma-m_\sigma^2\sigma^2)-\frac{1}{3}g_1\sigma^3-\frac{1}{4}g_2\sigma^4+\frac{1}{2}m_\omega^2\omega_\mu\omega^\mu \\ &-\frac{1}{4}F_{\mu\nu}F^{\mu\nu}+\frac{1}{2}m_\sigma^2\boldsymbol{b}_\mu\boldsymbol{b}^\mu-\frac{1}{4}\boldsymbol{G}_{\mu\nu}\boldsymbol{G}^{\mu\nu}-\frac{1}{4}H_{\mu\nu}H^{\mu\nu}, \end{aligned} \tag{C.2}$$

where, $F_{\mu\nu}=\partial_\mu\omega_\nu-\partial_\nu\omega_\mu$, $\boldsymbol{G}_{\mu\nu}=\partial_\mu b_\nu-\partial_\nu b_\mu$, $H_{\mu\nu}=\partial_\mu A_\nu-\partial_\nu A_\mu$, and the σ, ω_μ, $\boldsymbol{b}_\mu$ and A_μ

are the σ, ω, ρ mesons and the electromagnetic field, respectively. At the case of the RMF model, M and m_i ($i = \sigma, \omega, \rho$) are real nucleon and meson masses, and are not free parameters. Thus, the number of free parameters in the RMF models is generally small than the SHF models. These values of meson masses are slightly different from the recommended values of Particle Data Group [34], however the differences do not affect processes to determined from other parameters. The variable coupling constants g_j are treated as free parameters for the fit. Table C.1 shows parameterizations for each typical interactions, and the properties of the nuclear EOS. The symmetry energy term $a_{\rm sym}(\rho)$ is defined as the second derivative of the Hamiltonian density H as;

$$a_{\rm sym}(\rho) = \frac{1}{2}\lim\frac{\partial^2}{\partial I^2}(\frac{H}{\rho}) \tag{C.3}$$

with respect to the asymmetry parameter *I=(N-Z)/A*. In this case, the symmetry energy coefficient $a_{\rm sym}$ and its density dependent L are expressed as;

$$\begin{aligned} a_{\rm sym} &= a_{\rm sym}(\rho_\infty) && \text{(C.4)} \\ L &= 3\rho\frac{\partial}{\partial\rho}a_{\rm sym}(\rho). && \text{(C.5)} \end{aligned}$$

Thus in the SHF models, the $a_{\rm sym}$ is given by;

$$\begin{aligned} a_{\rm sym} &= \frac{\hbar}{6m}(\frac{3\pi^2}{2})^{2/3}\rho^{2/3} - \frac{1}{8}t_0(1+2x_0)\rho - \frac{1}{48}t_3(1+2x_3)\rho^{\alpha+1} \\ &\quad -\frac{1}{24}(\frac{3\pi^2}{2})^{2/3}\{3t_1x_1 - t_2(4+5x_2)\}\rho^{5/3}, \end{aligned} \tag{C.6}$$

while, in the RMF models it becomes;

$$\begin{aligned} a_{\rm sym} &= \frac{3\pi^2 A}{16 g_\sigma k_F^3}[3(m_\sigma^2\phi + g_1\phi^2 + g_2\phi^3) - \frac{M^*}{g_\sigma}(m_\sigma^2 + 2g_1\phi + 3g_2\phi^2)] \\ &\quad + \frac{g_\rho^2 k_F^3}{3\pi^2 m_\rho^2} + \frac{1}{24}[-\frac{k_F^4}{B^3} + \frac{5k_F^2}{B} + \frac{9M^*A}{B}], \end{aligned} \tag{C.7}$$

where A and B are given by;

$$\begin{aligned} A &\equiv -\frac{2k_F^5 M^*}{9B^3}\{\frac{2g_\sigma k_F}{\pi^2}(B - \frac{M^{*2}}{B}) \\ &\quad + \frac{3}{M^*}(m_\sigma^2\phi + g_1\phi^2 + g_2\phi^3) - \frac{1}{g_\sigma}(m_\sigma^2 + 2g_1\phi + 3g_2\phi^2)\}^{-1} && \text{(C.8)} \\ B &\equiv \sqrt{k_F^2 + M^{*2}}. && \text{(C.9)} \end{aligned}$$

And in the SHF models, the density dependent coefficient L is simply expressed as;

$$\begin{aligned} L &= \frac{\hbar}{3m}(\frac{3\pi^2}{2})^{2/3}\rho^{2/3} - \frac{3}{8}t_0(1+2x_0)\rho - \frac{1}{16}t_3(1+2x_3)(\alpha+1)\rho^{\alpha+1} \\ &\quad -\frac{5}{24}\{3t_1x_1 - t_2(4+5x_2)\}(\frac{3\pi^2}{2})^{2/3}\rho^{5/3}. \end{aligned} \tag{C.10}$$

Table C.1: Some parameter sets on non-relativistic and relativistic mean field model, and the EOS properties of their parameters sets.

Force	SIII	SkM*	L-HS	NL3	TMA	
t_0(MeVfm^3)	-1128.75	-2645.00	938.9	938	938.9	M (MeV)
t_1(MeVfm^5)	395.0	410.0	520.0	508.194	519.151	m_σ (MeV)
t_2(MeVfm^5)	-95.0	-135.0	783.0	782.501	781.950	m_ω (MeV)
t_3(MeVfm^3)	14000.	15595.	770.0	763.000	768.100	m_ρ (MeV)
x0	0.45	0.09	10.4814	10.217	10.055+3.050/A$^{0.4}$	g_σ
x1	0.00	0.00	13.8144	12.868	12.842+3.191/A$^{0.4}$	g_ω
x2	0.00	0.00	8,08488	4.474	3.800+4.644/A$^{0.4}$	g_ρ
x3	1.00	0.00	0.0	-10.431	-0.328 -27.879/A$^{0.4}$	g_2(fm^{-1})
σ	1	1/6	0.0	-28.885	38.862 -184.191/A$^{0.4}$	g_3
W_0(MeVfm^5)	120.0	130.0	0.0	0.0	151.590-378.004/A$^{0.4}$	g_4
E/A(MeV)	-15.851	-15.770	-15.73	-16.299	-16.025	–
ρ_∞(fm^{-3})	0.145	0.160	0.148	0.148	0.147	–
K_∞(MeV)	355.4	216.6	544.4	271.76	318.146	–
m^*_∞/m	0.76	0.79	0.56	0.60	0.635	–
a_s(MeV)	28.16	30.03	34.9	37.4	30.661	–
L(MeV)	9.96	45.80	—	118.83	—	–

In the case of the RMF models, the L can analytically be calculated, but the expression is not simple. Thus we do not express L in the RMF models here.

Figure C.1 displays a distribution of for 35 sets of Skyrme interaction parameters, i.e., SI-SIV, Ska, Skb, SkM$^{(*)}$, $E_{(\sigma)}$, G_σ, R_σ, $Z^{(*)}_{(\sigma)}$, MSKa, MSk7, BSk1, SkT6, SkSC4, SkP, SkX, SLy, and SkI1-5 and relativistic mean field models, NL1-3, NL-Z, NL-SH, TM1, TM2, and TMA. Hatched areas show the restricted region in this work and in Ref. [38]. The only parameterizations which are often used or are recently determined; SIII, SkM$^{(*)}$, SGII, SkP, SkX, SLy, NL3, and TMA, indicated in Fig. C.1, where K_∞ and the $a_{\rm sym}$ values of these parameter sets are taken from Ref. [90] except TMA, and these values of TMA parameter set are taken from Ref. [91]. The SkM$^{(*)}$ parameterizations are in good agreement with both the K_∞ and the $a_{\rm sym}$. The SkP and SLy are also in better agreement with the both quantities. However the SGII parameterization only reproduce the K_∞, and the SkX parameterization only reproduce the $a_{\rm sym}$. And the correlations between the $a_{\rm sym}$ and the density dependence coefficient L of the $a_{\rm sym}$ are shown in Fig. C.2. The tendency is similar behavior to the Fig. C.1, but SGII is also in good agreement with both values.

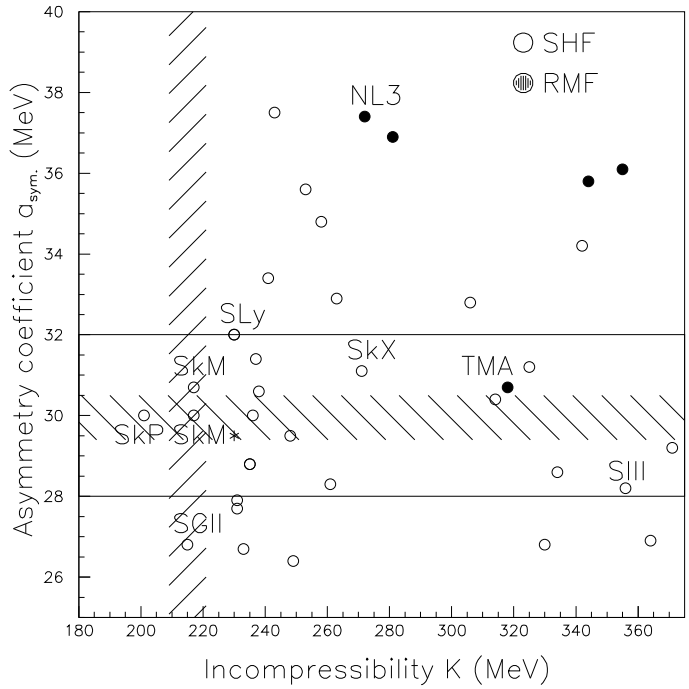

Figure C.1: The EOS property distribution using variable parameter sets. Hated areas show the restricted region in this work. Its values are 215±6 MeV of the incompressibility K_∞ [38] and 30.0±0.5 (2.0) MeV of the symmetry energy a_{sym}.

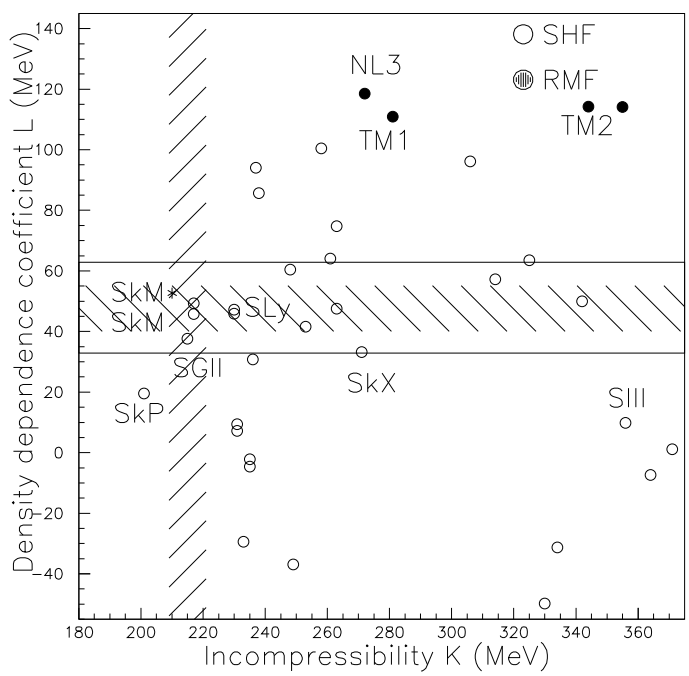

Figure C.2: The EOS property distribution using variable parameter sets. Same as Fig. C.1, but vertical axis is the density dependence coefficient L. Its value is 47.9±7.0 (15.0) MeV.

Appendix D

Definition of nuclear surface diffuseness

In general, nuclear surface diffuseness is defined as a length from 90% to 10% of a normal nuclear density ρ_0. In the case of theoretical calculations or model-independent density functions as Fourier-Bessel or sum-of-Gaussian, it is difficult to define the normal nuclear density without a constraint using a functional shape. We attempt to define the nuclear surface diffuseness by differentiating density function. If we use a Wood-Saxon functional shape (two-parameter Fermion; 2pF) of a nucleon density, a nuclear diffuseness t is unique determined as follows;

$$t = 4 \cdot \ln 3 \cdot a, \tag{D.1}$$

where,

$$\rho(r) = \frac{\rho_0}{1 + \exp((r-c)/a)},$$

where, the parameters c and t are the half-density radius and the surface diffuseness, respectively.

A differential function of density is expected to have a specific character in a surface region of density. The differential function of 2pF is shown as follows;

$$\begin{aligned} \frac{d}{dr}\rho(r) &= \frac{d}{dr}\frac{\rho_0}{1+\exp((r-c)/a)} \\ &= -\frac{\rho_0}{a}(\exp((r-c)/2a) + \exp(-(r-c)/2a))^{-2} \\ &= -\frac{\rho_0}{a}(2\cosh((r-c)/2a))^{-2}. \end{aligned} \tag{D.2}$$

Then, a full width at half maximum (FWHM) of this differential function is described as;

$$\begin{aligned} \text{FWHM} &= 2a\ (\ln(\sqrt{2}+1) - \ln(\sqrt{2}-1)) \\ &= 4a\ \ln(\sqrt{2}+1) \\ &= \ln(\sqrt{2}+1)/\ln 3 \times t \\ &\sim 0.8022\ t. \end{aligned} \tag{D.3}$$

We can see a clear relation between the width of differential function and the surface thickness t.

Figure D.1 shows a result from charge distribution of ^{124}Sn. The parameter set of 2pF is taken from Ref. [7]. The width region indicated by lower arrows almost corresponds to the surface diffuseness one indicated upper arrows. Therefore, the width is expected to indicate the t, even when any functional shape as a density is used.

The different model-dependent density called a two-parameter Gaussian (2pG) is calculated in a comparison with the 2pF function. This model-dependent density is usually not used, however it is more easy to define the normal density than 3pG which is usually used as a model-dependent density. The 2pG density is expressed as;

$$\rho(r) = \frac{\rho_0}{1 + \exp((r^2 - c^2)/a^2)}, \tag{D.4}$$

and in this case, the surface diffuseness t is described as follows;

$$\begin{aligned} t &= r(\rho(r) = 0.1\rho_0) - r(\rho(r) = 0.9\rho_0) \\ &= \sqrt{c^2 + 2a^2 \ln 3} - \sqrt{c^2 - 2a^2 \ln 3}. \end{aligned} \tag{D.5}$$

A derivative of 2pG is described as;

$$\begin{aligned} \frac{d}{dr}\rho(r) &= \frac{d}{dr}\frac{\rho_0}{1 + \exp((r^2 - c^2)/a^2)} \\ &= -\frac{2\rho_0}{a^2} r(\exp((r^2 - c^2)/2a^2) + \exp(-(r^2 - c^2)/2a^2))^{-2} \\ &= -\frac{2\rho_0}{a^2} r(2\cosh((r^2 - c^2)/2a^2))^{-2}. \end{aligned} \tag{D.6}$$

In the case of the 2pG, the width in FWHM of the differential function can not be expressed a simple form differently the 2pF case. The value of the width for the derivative of the density are numerically calculated as;

$$\text{FWHM} \sim 0.7532\ t. \tag{D.7}$$

This ratio is in disagreement with the result for 2pF about 5%. The result shows that it is more difficult to define a normal density of the 2pG than the 2pF, because a flat region of the 2pG density is very narrow compared with the 2pF case. In this work, we adopt the ratio of the 2pF case (=0.8022) as the surface thickness. Figure D.2 shows a result from charge distribution of ^{124}Sn using the 2pG form. The parameter set of the 2pG density is taken whose density has the same RMS radius and t as the 2pF case. The width region almost corresponds to the surface diffuseness one.

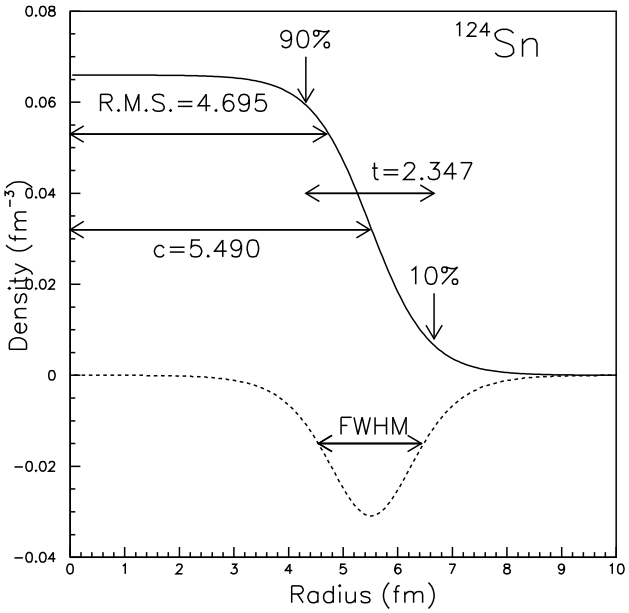

Figure D.1: A two-parameter Fermion (2pF) charge distribution of ^{124}Sn, and the differential shape of the distribution. Solid line is charge distribution by using 2pF function. Dashed line is differential function of the 2pF function

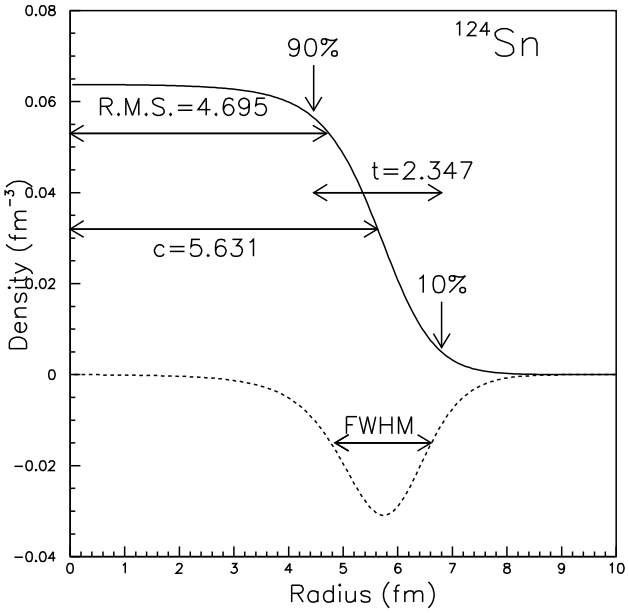

Figure D.2: A two-parameter Gaussian (2pG) charge distribution of ^{124}Sn, and the differential shape of the distribution. Two parameters of 2pG are used same RMS and the surface thickness of Fig. D.1. Solid line is charge distribution by using 2pG function. Dashed line is differential function of the 2pG function

Figure D.3 shows derivatives of the charge distributions for ^{124}Sn. The three charge distributions are used; 2pF, 3pG, and SOG which are in the same as in Fig 4.1. The surface diffuseness t of the 2pF is expected to be smaller than other two distributions from the slope of form factor distributions in Fig. 4.2, and the t of the 3pG is also expected to be slightly smaller than one of the SOG.

The results of t using three densities are deduced using the widths of the derivatives as follows;

$$\begin{aligned} t &= 2.34 \pm 0.25 \text{ (fm) [2pF]} \\ &= 2.57 \pm 0.09 \text{ (fm) [3pG]} \\ &= 2.67 \text{ (fm) [SOG]}, \end{aligned}$$

where, these values are multiplied by 0.8022^{-1}. The above three results are in good agreement with the expectations from in Fig. 4.2.

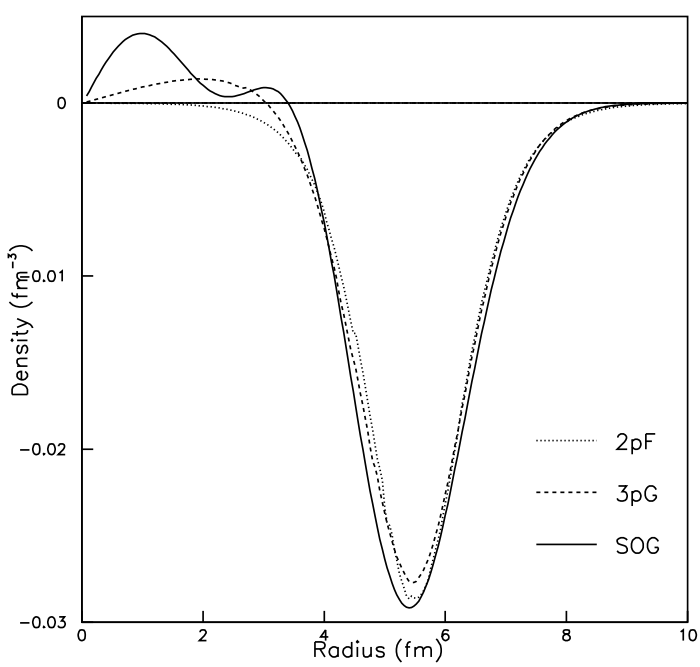

Figure D.3: The differential shapes of various charge distributions. Charge distributions for ^{124}Sn are in the same as in Fig. 4.1. The solid, dashed, and dotted lines are the derivative function of SOG, 3pG, and 2pF, respectively.

Appendix E

Analytical form factors of a nucleon and a nuclei

Here, I summarize the useful analytical expressions for the nucleon or nuclear charge form factors which are used in this work or were often used. The density $\rho(r)$ and the form factor $F(q)$ are correlated by the Fourier transform as follows;

$$\begin{aligned} F(q) &= \oint \rho(\boldsymbol{r}) e^{-i\boldsymbol{qr}} d\boldsymbol{r} \\ &= \int_0^\infty 4\pi r^2 \frac{\sin(qr)}{qr} \rho(r) dr \qquad \text{(E.1)} \\ \rho(r) &= \frac{1}{(2\pi)^3} \oint F(\boldsymbol{q}) e^{+i\boldsymbol{qr}} d\boldsymbol{q} \\ &= \frac{1}{(2\pi)^3} \int_0^\infty 4\pi q^2 \frac{\sin(qr)}{qr} F(q) dq. \qquad \text{(E.2)} \end{aligned}$$

For the nuclear charge density, a hard sphere like a realistic ball is given as follows;

$$\rho(r) = \begin{cases} \rho_0 & \text{for } r < R \\ 0 & \text{otherwise,} \end{cases} \qquad \text{(E.3)}$$

the form factor is expressed as;

$$F(q) = \frac{4\pi\rho_0}{q^3}[\sin(qR) - qR\cos(qR)]. \qquad \text{(E.4)}$$

The symmetrized Fermi distribution;

$$\rho(r) = \rho_0 \frac{\cosh(R/a)}{\cosh(R/a) + \cosh(r/a)}, \qquad \text{(E.5)}$$

leads to the following form factor;

$$F(q) = -\frac{4\pi\rho_0 a}{q} \frac{\cosh(R/a)}{\sinh(R/a)} [\frac{R\cos(qR)}{\sinh(\pi qa)} - \frac{\pi d \sin(qR)\cosh(\pi qa)}{\sinh^2(\pi qa)}]. \qquad \text{(E.6)}$$

The Fermi distribution;

$$\rho(r) = \rho_0/[1+e^{(r-R)/a}], \tag{E.7}$$

with the central density ρ_0, the diffraction radius R, and the surface diffusenesses a gives a good description of the densities for medium-heavy nuclei. This form factor can be calculated approximately as;

$$F(q) = \frac{4\pi\rho_0}{q^3}\frac{\pi qa}{\sinh(\pi qa)}(\pi qa\cdot\coth(\pi qa)\sin(qR) - qR\cdot\cos(\pi qa)). \tag{E.8}$$

The form factor is a approximated equation not an analytic one, however the agreement of this equation is very good.

For light nuclei, it is more appropriate to use the Gaussian density shown as;

$$\rho(r) = \frac{1}{\pi^{3/2}a_p^3}e^{-(r/a_p)^2}, \tag{E.9}$$

the form factor is;

$$F(q) = e^{-(a_p q/2)^2}. \tag{E.10}$$

Above all, model-independent densities, so-called a sum-of-Gaussian and Fourier-Bessel are expressed as follows;

$$\begin{aligned}\rho(r) &= \frac{1}{2\pi^{3/2}\gamma^3}\sum\frac{Q_i}{1+2R_i^2/\gamma^2} \\ &\quad\times(e^{-(r-R_i)^2/\gamma^2}+e^{-(r+R_i)^2/\gamma^2}), \end{aligned}\tag{E.11}$$

$$\begin{aligned}F(q) &= \sum\frac{Q_i}{1+2R_i^2/\gamma^2} \\ &\quad\times(\cos(qR_i)+2R_i/q\gamma^2\sin(qR_i))e^{-(\gamma q/2)^2}, \end{aligned}\tag{E.12}$$

and

$$\rho(r) = \sum a_v\frac{\sin(v\pi r/R)}{v\pi r/R} \tag{E.13}$$

$$F(q) = \sum\frac{2R^2a_v}{qv}(\frac{\sin(v\pi-qR)}{v\pi-qR}-\frac{\sin(v\pi+qR)}{v\pi+qR}). \tag{E.14}$$

The nucleon electric and magnetic form factor except the neutron electric form factor is well expressed using the famous form; so-called a dipole form factor, which corresponds to two poles with opposite sign close to each other in the time-like region. The dipole form factor is expressed as;

$$F(q) = \frac{1}{(1+q^2/a^2)^2}. \tag{E.15}$$

The density so-called a Yukawa distribution corresponds to the dipole form factor as follows;

$$\rho(r) = \frac{a^3}{8\pi} e^{-ar}, \tag{E.16}$$

Then, to examine the higher momentum transfer region, the form factors a sum-of-monopole form factor is introduced. This equation is described as;

$$F(q) = \sum \frac{Q_i}{1 + q^2/m_i^2}, \tag{E.17}$$

a corresponding density is simply described as;

$$\rho(r) = \frac{1}{4\pi r} \sum m_i^2 Q_i e^{-m_i r}. \tag{E.18}$$

On the other hand, the electric form factor of neutron is usually used so-called the Galster parameterization as follows;

$$F(q) = \frac{q^2/a^2}{1 + q^2/b^2} \frac{1}{(1 + q^2/c^2)^2}, \tag{E.19}$$

the density can be analytically transformed as;

$$\begin{aligned} \rho(r) &= \frac{b^2}{8\pi(1 - b^2/c^2)^2 a^2 r} \\ &\quad \times (cr(c^2 - b^2)e^{-cr} + 2b^2(e^{-cr} - e^{-br})). \end{aligned} \tag{E.20}$$

Appendix F

Uncertainties of the ^{58}Ni neutron density distribution

In this work, the neutron density distribution of ^{58}Ni is assumed as Eq. (4.29) by neglecting a microscopic structure of ^{58}Ni. According to the systematics obtained by solving the Schroedinger equation for one-particle motion in a spherical potential [92], the last two neutron of ^{58}Ni might occupy $2p_{3/2}$ state as shown in Fig. F.1. Some theoretical calculations, for example SHF(SkM*), RMF(L-HS), and the experimental results [93] support this picture.

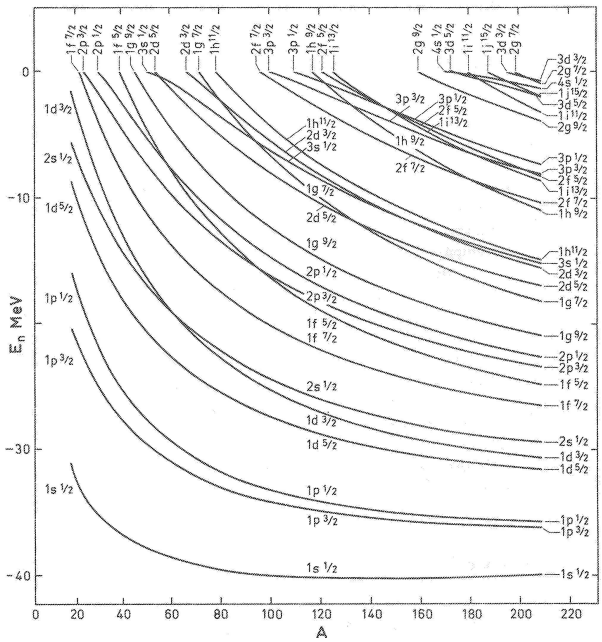

Figure F.1: Energies of neutron orbits in a spherical potential [92].

A different neutron density distribution can be calculated to compare the neutron density from Eq. (4.29). The neutron density are described as;

$$\rho_n(r) = \rho_p(r) + (\rho_n^{SHF}(r) - \rho_p^{SHF}(r)), \tag{F.1}$$

where $\rho_n(p)$ is point neutron (proton) density distribution. The SHF calculation with BCS force using the SkM* parametrization is used, because its neutron skin thickness Δr_{np} is very small as shown in Table 4.2, and it gives the almost same neutron RMS radius.

Figure F.3 shows the fitting result for ^{58}Ni and a comparison with results using different neutron density distributions. The solid and dashed lines show the fitting results using Eq. (F.1) and Eq. (4.21), respectively. Dashed lines are in the same as in Fig. 4.20. And the correlation between same parameter sets as Fig 4.21 is shown in Fig. F.2. The open symbol and errors show in the same one in Fig. 4.21. The best values from in Fig. F.2 are smaller than the values from in Fig. 4.21, however the trend of this correlation is very similar as shown in Fig 4.21. The modification ratios of coupling constants at normal density are also almost same as ones of masses using Eq. (F.1). However the best reduced chi-square χ_{min} using neutron densities of Eq. (F.1) is worse than the case of Eq. (4.29) about 10%. Therefore finally in this work, the neutron density distribution of Eq. (4.29) not Eq. (F.1) is adopted.

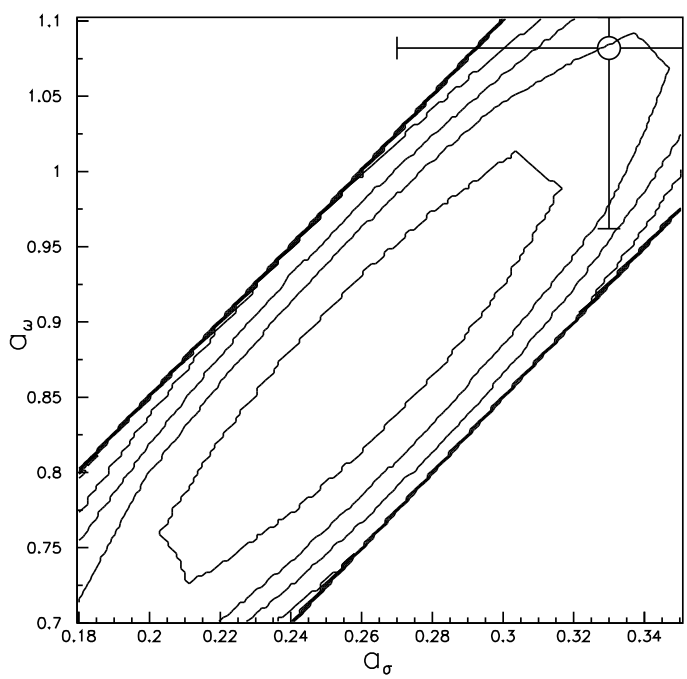

Figure F.2: Correlation between a_σ and a_ω using the neutron densities described in Eq. (F.1).

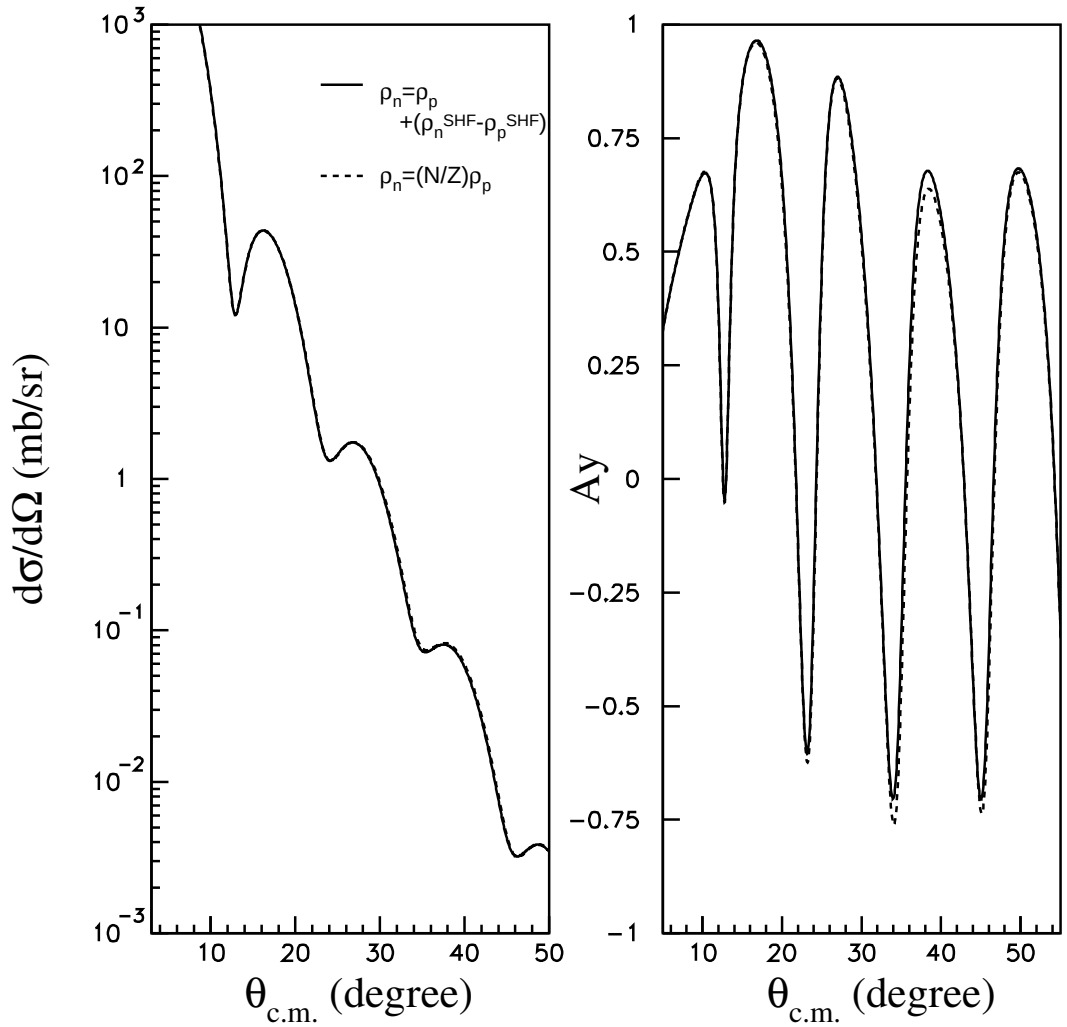

Figure F.3: Fitting results with two different densities. Solid, and dashed lines show the calculation using Eq. (F.1), and Eq. (4.29), respectively.

Appendix G

Nucleon swelling and neutron skin thickness

In our analysis, we assume that the properties of proton in the nuclei do not change, which corresponds to satisfy Eq. (4.21). Some time ago the European Muon Collaboration (EMC) collaboration discovered that the structure function for iron F_2^{Fe} differs substantially from the corresponding deuteron structure function F_2^d [94], far beyond trivial Fermi motion corrections. Since then many experiments dedicated to a study of nuclear effects in deep inelastic scattering have been carried out at CERN, SLAC, and FNAL. Figure G.2 presents a compilation of data for the structure function ratio F_2^A/F_2^d over range $0 < x < 1$ in the Bjorken scaling variable x. Here F_2^A is the structure function per nucleon of a nucleus with mass number A, and F_2^d refers the deuteron. Neglecting small nuclear effects in the deuteron, F_2^d can approximately stand for the isospin averaged nucleon structure function F_2^N. However, the more detailed analysis must include two-nucleon effects in the deuteron. Then the ratio F_2^A/F_2^d would have become one. Several distinct regions with characteristic nuclear effects can be identified: at $x < 0.1$ one observes a systematic reduction of the ratio, the so-called nuclear shadowing [95]. For $x > 0.8$ the observed enhancement of the nuclear structure function is associated with nuclear Fermi motion. Unlike the two regions, $0.1 < x < 0.8$ region is often refereed to as the traditional "EMC effect", which are still not fully understood. One of models which explains the ratio in the region is modifications of bound nucleon structure functions. The intrinsic properties of nucleons bound in nuclei can be modified as compared to free nucleons [95]. The modification is related to possible "swelling" of nucleon inside nuclei.

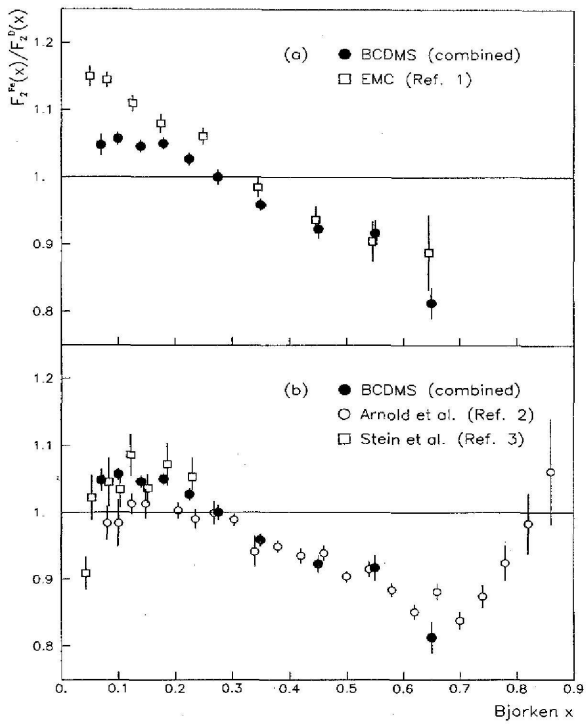

Figure G.1: The ratio of nuclear and nucleon structure function, F_2^A/F_2^d for ^{40}Ca, ^{56}Fe [95]. The data are taken from EMC, SLAC.

The experimentally observed y-scaling also indicates a rather small increase of the charge radius for bound nucleons. For example, the study of Sick [96, 97] comes to the conclusion that any increase of the nucleon radius in nuclei should be less than 6% of its free radius in ^{3}He. Barone *et al.* presented the nucleon swelling ratios in wide mass region from A=4 (^{4}He) to A=208 (^{208}Pb), which varies 3.8% (^{4}He), and 9.9% (^{208}Pb) [98]. However only the "swelling" effect can not explain the ratio in the "EMC effect" region. Other explanations have considered the existence of multi-quark clusters [99], or an excess of pions [100], or of dynamical rescaling [101]. Therefore, we have estimated how the nucleon "swelling" phenomenon affect to the neutron skin thickness. We have taken 6 $\pm$ 1 % in A$\sim$120 as the swelling ratio of proton tin isotopes whose number corresponds to tin isotopes.

Recently Sick suggested the larger RMS radius (0.895(18) fm) for the proton charge than the present obtained value (0.863(4) fm) [102]. He introduced a new type parameterization Continued Fraction expansions, and fitted using low-q data up to 1.2 fm^{-1} only to avoid the effect of the higher moments.

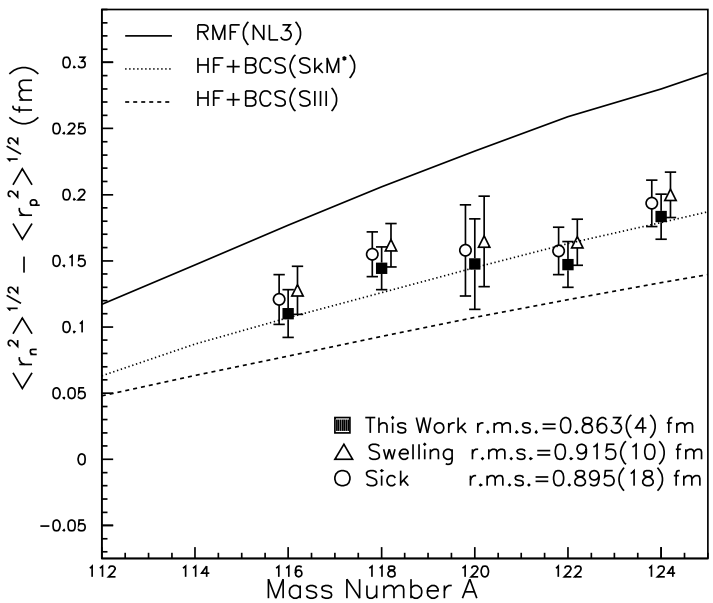

Figure G.2: Comparison with neutron skin thickness using different proton RMS radius.

We can not deduce the point proton density distributions using these proton charge RMS radii, because both cases do not provide for the proton electric form factor G^p_{ch}. Thus we have simply calculated the neutron skin thickness Δr_{np}. The Δr_{np} are calculated substituting of Eq. (4.28) into Eq. (5.1) as;

$$\Delta r_{np} = \sqrt{\frac{A}{N}\langle r_m\rangle^2 - \frac{Z}{N}(\langle r_p\rangle^2 - \langle r^p_{ch}\rangle^2) + \langle r^{n\,2}_{ch}\rangle} \; - \; \sqrt{\langle r_{ch}\rangle^2 - \langle r^p_{ch}\rangle^2 - \frac{N}{Z}(\langle r^{n\,2}_{ch}\rangle} \qquad \text{(G.1)}$$

where, we have used the matter RMS radii $\sqrt{\langle r^2_m\rangle}$ of Table 5.2 as experimental results in this work, because the proton elastic scattering is most sensitive to the matter distribution. The systematic error of matter distribution might be relatively small. Figure G.2 shows the comparison of neutron skin thicknesses using different proton RMS radii. The results of Δr_{np} using the larger proton RMS radius are slightly larger than the values in this analysis. The order of these differences are about 0.015 fm, the difference is almost in the same order as the error of the Δr_{np}.

Bibliography

[1] Beat Hahn, D. G. Ravenball, and Robert Hofstadter Phys. Rev. **101**, 1131(1956), and references therein.

[2] G. A. Jones, Rep. Prog. Phys. **33**, 645 (1970).

[3] C. W. de Jager, H. de Vries, and C. de Vries, Atomic Data and Nuclear Data Tables **14**, 479 (1974).

[4] B. Dreher, J. Friedrich, K. Merle, H. Rothhaas, and G. Luhrs, Nucl. Phys. A**235**, 219 (1974).

[5] I. Sick, Nucl. Phys. A**218**, 509 (1974).

[6] C. J. Batty E. Friedman, H. J. Gils, and H. Rebel, in Advances in Nuclear Physics, edited by J. W. Negele and E. Vogt (Plenum, New York, 1989), Vol. 19, p. 1. and references therein.

[7] H. de Vries, C. W. de Jager, and C. de Vries, Atomic Data and Nuclear Data Tables **36**, 495 (1987).

[8] M. N. Rosenbluth, Phys. Rev. **79**, 615(1950).

[9] E. B. Hughes, T. A. Griffy, M. R. Yearian, and R. Hofstadter, Phys. Rev. **139**, B458(1965).

[10] B. Milbrath *et al.*, Phys. Rev. Lett. **80**, 452(1998).

[11] M. K. Jones *et al.*, Phys. Rev. Lett. **84**, 1398(2000).

[12] O. Gayou *et al.*, Phys. Rev. Lett. **88**, 092301(2002).

[13] S. Galster, H. Klein, J. Moritz, K. H. Schmidt, and D. Wegener, Nucl. Phys. B**32**, 221(1971).

[14] S. Kopecky, J. A. Harvey, N. W. Hill, M. Krenn, M. Pernicka, P. Riehs, and S. Steiner, Phys. Rev. C **56**, 2229 (1997).

[15] J. Golak, G. Ziemer, H. Kamada, H. Witala, and W. Glockle, Phys. Rev. C **63**, 034006 (2001).

[16] L. E. Price, *et al.*, Phys. Rev. D **4**, 45 (1971); G. G. Simon, Ch. Schmitt, F. Borkowski, and V. H. Walther, Nucl. Phys. A**333**, 381 (1980); L. Andivahis *et al.*, Phys. Rev. D **50**, 49 (1994).

[17] Charles Earl Hyde-Wright, and Kees de Jager, Annu. Rev. Nucl. Part. Sci. **54**, 217 (2004), and references therein.

[18] A. Trzcinska, J. Jastrzebski, P. Lubinski, H. J. Harfmann, R. Schmidt, T. von Egidy, and B. Klos, Phys. Rev. Lett. **87**, 082501 (2001).

[19] C. J. Batty, E. Friedman, and A. Gal, Nucl. Phys. A**592**, 487 (1995).

[20] R. R. Johnson *et al.*, Phys. Rev. Lett. **43**, 844 (1979).

[21] B. M. Barnett *et al.*, Phys. Lett. B**156**, 172 (1984).

[22] H. J. Gils, H. Rebel, and E. Friedman, Phys. Rev. C**29**, 1295 (1984).

[23] T. Takahashi, H. Sakaguchi, K. Aoki, T. Hasegawa, O. Hashimoto, T. Nagae, M. Sekimoto, A. Ohkusu, H. Bhang, H. Yu, and Y. Gavrilov, Phys. Rev. C**51**, 2542 (1995).

[24] K. Aoki, H. Sakaguchi, N. Nose-Togawa, T. Takahashi, T. Hasegawa, O. Hashimoto, T. Nagae, M. Sekimoto, A. Ohkusu, H. Bhang, H. Yu, and Y. Gavrilov, Phys. Rev. C**76**, 024610 (2007).

[25] J. D. Lumpe and L. Ray, Phys. Rev. C**33**, 665 (1986).

[26] E. T. Boschitz, W. K. Roberts, J. S. Vincent, K. Gotow, P. C. Gugelot, C. F. Perdrist, and L. W. Swenson, Phys. Rev. Lett. **20**, 1116 (1968).

[27] G. D. Alkhazov *et al.*, Phys. Lett. B**67**, 402 (1977).

[28] A. Chaumeaux, V. Layly, and R. Schaeffer, Phys. Lett. B**72**, 33 (1977).

[29] I. Brissaud, M. K. Barussel, Phys. Rev. C **15**, 452 (1977).

[30] A. K. Kerman, H. McManus, and R. M. Thaler, Ann. Phys. (N.Y.) **8**, 551 (1959).

[31] L. Ray, W. R. Coker, and G. W. Hoffmann, Phys. Rev. C **18**, 2641 (1978).

[32] L. Ray, Phys. Rev. C **19**, 1855 (1979).

[33] V. E. Starodubsky and N. M. Hintz, Phys. Rev. C **49**, 2118 (1994).

[34] W. M. Yao *et al.*(Particle Data Group), J. Phys. G **33**, 1 (2006).

[35] C. J. Horowitz, Phys. Rev. C **31**, 1340 (1985); D. P. Murdock and C. J. Horowitz, Phys. Rev. C **35**, 1442 (1987); C. J. Horowitz, D. P. Murdock, and Brian D. Serot *Computational Nuclear Physics 1* (Springer-Verlag, Berlin, 1991), Chap. 7.

[36] H. Sakaguchi *et al.*, Phys. Rev. C **57**, 1749 (1998).

[37] H. Takeda, Doctor Thesis (2002), Kyoto University.

[38] M. Uchida *et al.*, Phys. Lett. B**557**, 12 (2003); M. Uchida, Doctor Thesis (2003), Kyoto University.

[39] B. Alex Brown, Phys. Rev. Lett. **85**, 5296(2000).

[40] P. Danielewicz, Nucl. Phys. A**727**, 233 (2003).

[41] Lie-Wen Chen, Che Ming Ko, and Bao-An Li, Phys. Rev. C **72**, 064309 (2005).

[42] S. Yoshida and H. Sagawa, Phys. Rev. C **69**, 024318(2004).

[43] R. J. Furnstahl, Nucl. Phys.. A**706**, 85 (2002).

[44] P. G. Reinhard, T. Brvenich, T. Cornelius, P. Fleischer, P. Klupfel, and J. A. Maruhn, Nucl. Phys. A**746**, 76(2004).

[45] K. Hatanaka, K. Calais, H. Tamura, M. Sato, and I. Miura, Nucl. Instr. and Methods A**384**, 575 (1997).

[46] T. Ichihara, H. Sakaguchi, K. Hatanaka, M. Fujiwara and K. Hosono, RCNP Annual Report 1981, p. 194.

[47] M. Fujiwara *et al.*, Nucl. Instr. and Methods A**422**, 484 (1999).

[48] T. Kawabata, H. Sakaguchi, A. Tamii, H. Takeda, T. Taki, and H. Yoshida, RCNP Annual Report 1996, p. 161.

[49] HBOOK, CERN Program Library entry Y250.

[50] PAW, CERN Program Library entry Q121.

[51] W. R. Leo, *Techniques for Nuclear amd Particle Physics Experiments* (Springer-Verlag, Berlin, 1987).

[52] R. B. Firestone and V. S. Shirley, *Table of Isotope*, 8th ed. (John Wiley & Sons, New York, 1996).

[53] S. Hama, B. C. Clark, E. D. Cooper, H. S. Sherif, and R. L. Merceri, Phys. Rev. C **41**, 2737 (1990).

[54] E. D. Cooper, S. Hama, B. C. Clark, and R. L. Mercer, Phys. Rev. C **47**, 297 (1993).

[55] J. A. McNeil, J. R. Shepard, and S. J. Wallace, Phys. Rev. Lett. **50**, 1439 (1983).

[56] C. J. Horowitz and B. D. Serot, Nucl. Phys. A**368**, 503 (1981).

[57] G. E. Brown and Mannque Rho, Phys. Rev. Lett. **66**, 2720 (1991).

[58] Tetsuo Hatsuta and Su Houng Lee, Phys. Rev. C. **46**, 34 (1991).

[59] A. Kato, S. Kimpara, and T. Kohmura, Prog. Theor. Phys. **94**, 657 (1995); T. Nagata, A. Kato, and T. Kohmura, Nucl. Phys. A**601**, 333 (1996).

[60] S. Shim, B. C. Clark, S. Hama, E. D. Cooper, R. L. Mercer, L. Ray, and G. W. Hoffmann, Phys. Rev. C **38**, 1968 (1988).

[61] J. R. Ficenec, L. A. Fajardo, W. P. Trower, and I. Sick, Phys. Lett. B**42**, 213 (1972).

[62] J. Cavedon, J. B. Bellicard, B. Frois, D. Goutte, M. Huet, P. Leconte, X.-H. Phan, and S. K. Platchkov, Phys. Lett. B**118**, 311 (1982).

[63] C. Piller *et al.*, Phys. Rev. C **42**, 182 (1990).

[64] I. Angeli, Atomic Data and Nuclear Data Tables **87**, 185 (2004).

[65] R. G. Sachs, Phys. Rev. **126**, 2256(1962).

[66] Ingo Sick, Prog. Part. Nucl. Phys. **11**, 411(1984).

[67] J. J. Kelly, Phys. Rev. C **70**, 068202 (2004).

[68] S. Bourzeix, B. de Beauvoir, F. Nez, M. D. Plimmer, F. de Tomasu, L. Julien, and F. Biraben, Phys. Rev. Lett. **76**, 384 (1996).

[69] C. B. Crawford, *et al.*, Phys. Rev. Lett. **98**, 052301 (2007).

[70] MINUIT, CERN Program Library entry D506.

[71] J. Bartel, P. Quentin, M. Brack, C. Guet, and H. B. Hakansson, Nucl. Phys. A**386**, 79 (1982).

[72] M. Beiner, H. Flocard, Nguyen Van Giai, and P. Quentin, Nucl. Phys. A**238**, 29 (1975).

[73] Y. Sugahara and H. Toki, Nucl. Phys. A**579**, 557 (1994).

[74] K. Kaki, H. Toki, and I. Tanihata, Nucl. Phys. A**724**, 99 (2003).

[75] J. Decharge and D. Gogny Phys. Rev. C **21**, 1568 (1980).

[76] Naoki Tajima, Satoshi Takahashi, and Naoki Onishi, Nucl. Phys. A**603**, 23 (1996).

[77] J. Friedrich and P.-G. Reinhard, Phys. Rev. C **33**, 335 (1986); P.-G. Reinhard, *Computational Nuclear Physics 1* (Springer-Verlag, Berlin, 1991), Chap. 2.

[78] A. N. Antonov *et al.*, Phys. Rev. C **72**, 044307 (2005).

[79] G. A. Lalazissis, S. Raman, and P. Ring, Atomic Data and Nuclear Data Tables **71**, 1 (1999).

[80] R. M. Lombard, G. D. Alkhazov, and O. A. Domchenkov, Nucl. Phys. A**360**, 233 (1981).

[81] J. Dobaczewsi, W. Nazarewicz, and T. R. Werner, Z. Phys. A **354**, 27 (1996).

[82] F. Hofmann, C. M. Keil, and H. Lenske, Phys. Rev. C **64**, 034314 (2001).

[83] J. M. Cavedon Ph.D. thesis, University of Paris-Sud, Centre d'Orsay, 1980 (unpublished).

[84] R. P. Bevington and D. K. Robinson, *Data Reduction and Error Analysis for the Physical Sciences*, 3rd ed. (McGraw-Hill, New York, 2003).

[85] J. Raynal, computer cide, ECIS95, NEA0850-14.

[86] S. Raman, C. W. Nestor, and P. Tikkanen, Atomic Data and Nuclear Data Tables **78**, 1 (2001).

[87] A. Krasznahorkay *et al.*, Nucl. Phys. A**567**, 521 (1994).

[88] A. Krasznahorkay *et al.*, Phys. Rev. Lett. **82**, 3216 (1999).

[89] A. Klimkiewica *et al.*, Phys. Rev. C **76**, 051603 (2007).

[90] Kazuhiro Oyamatsu and Kei Iida, Prog. Theor. Phys. **109**, 631 (2003).

[91] L. Geng, Doctor Thesis (2005), Osaka University.

[92] A. Bohr and B.R. Mottelson, *NUCLEAR STRUCTURE vol 1,2*, (World Scientific, 1998).

[93] R. Sherr, B. F. Bayman, E. Rost, M. E. Rickey, and C. G. Hoor, Phys. Rev. **129**, B1272 (1965).

[94] J. J. Aubert *et al.*, Phys. Lett. B**123** 275 (1987).

[95] G. Piller, W. Weise, Phys. Rep. **330** 1 (2000).

[96] I. Sick, Phys. Lett. B**157** 13 (1985).

[97] I. Sick, Nucl. Phys. A**434** 677 (1985).

[98] V. Varone, M. Genovese, N. N. Nikolaev, E. Predazzi, and B. G. Zakharov. Z. Phys. C **58** 541 (1993).

[99] R. L. Jaffe, F. E. Close, R. G. Roberts, and G. G. Ross, Phys. Lett. B**134** 449 (1983).

[100] M. Ericson and A. Thomas, Phys. Lett. B**128** 112 (1983).

[101] F. E. Close, R. G. Boberts, and G. G. Ross, Phys. Lett. B**129** 346 (1983).

[102] I. Sick, Nucl. Phys. **A434** 677 (1985).

List of Tables

List of Figures